Sulfur and oxygen isotope insight into microbial sulfur metabolism

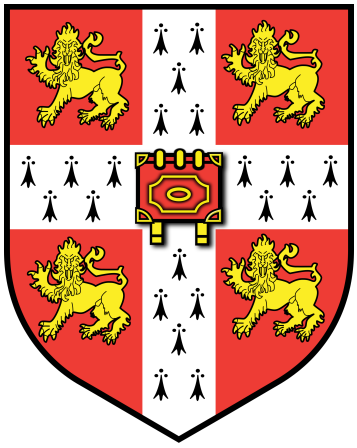

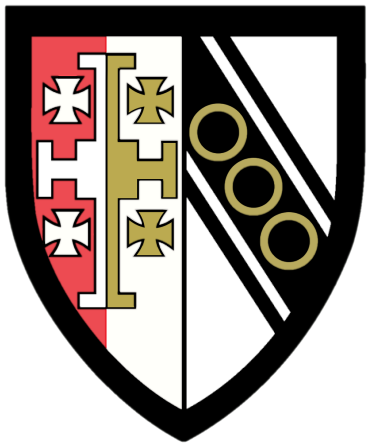

Gilad Antler

Selwyn College

This dissertation is submitted for the degree of Doctor of Philosophy

Department of Earth Sciences, University of Cambridge

July 2015

Declaration

This dissertation is the result of my own work and nothing which is the outcome of work done in collaboration except where specifically indicated in the text. It does not exceed the page limit and is not substantially the same as any work that has been or is being submitted to any university for any degree, diploma or other qualification

Gilad Antler

"The real voyage of discovery consists not in seeking new landscapes, but in having new eyes."

(Marcel Proust)

For the jalan atthirari anni/ for the moon of my life

Abstract

Dissimilatory microbial sulfate reduction (MSR) is a process where microbes utilize sulfate as an electron acceptor to oxidize organic matter in anoxic environments. In modern marine sediments, MSR is responsible for over half of the anoxic oxidation of organic matter. In addition, the anaerobic oxidation of methane (AOM) is coupled largely to MSR in marine sediments, in a process called sulfate-driven AOM, preventing the Earth's oceans from becoming a major source of this potent greenhouse gas to the surface.

The aim of this thesis was to elucidate the pathways of MSR coupled to organic matter oxidation and AOM by using a largely geochemical approach; specifically the chemical and isotope (C, S, O) variation in pure-culture sulfate reducing bacteria and sedimentary pore fluid profiles. I use this data to better understand how sulfate is involved in different diagenetic processes. The most powerful tool that used was the combined measurement and modeling of sulfur and oxygen isotopes in sulfate ($\delta^{18}O_{SO4}$ and $\delta^{34}S_{SO4}$, respectively), which enabled me to model how sulfate is recycled within pure cultures as well as the natural environment.

First I explore the combined multiple sulfur ($^{33}S/^{32}S$, $^{34}S/^{32}S$) and oxygen ($^{18}O/^{16}O$) isotope fractionation in pure cultures of a marine *Desulfovibrio* sp. DMSS-1 grown on different organic substrates. The use of multiple isotopes allows me to conclude that reversibility of each step during MSR in my experiment is correlates with the cell-specific rate sulfate reduction rate. I suggest that in environmental settings where the availability of the electron donor can change dramatically there may be more changes in the microbial mechanism of MSR that can be more pronounced.

In the second half of this thesis I explore MSR in marine and marginal marine environments and the consumption of sulfate through sulfate-driven AOM and organoclastic MSR. I find that in environments where methane is in excess there is a lower limit of the slope between $\delta^{18}O_{SO4}$ and $\delta^{34}S_{SO4}$ that results in what I call a distinct isotopic signature. This isotope signature differs to that when sulfate is reduced by either organic matter oxidation or by the slower, diffusive flux of methane within marine sediments. I suggest that this signature likely results from negligible reoxidation of sulfur species when the electron donor is abundant.

Acknowledgments

A PhD is a journey, a journey on a unique path for every man who chooses to walk it. Every day you see an undiscovered landscape, sometimes using someone else's flashlight when it's dark and sometimes, taking a ride on giants' shoulders to see far. Every person I've met along this journey has shaped the way I see things and the person that I am today, and for this I am grateful. And overall you have to remember that it is the journey that matters, the distance travelled.

First and foremost, I would like to thank my supervisor, Dr. Alexandra V. Turchyn. More than anything I want to thank Sasha for having trust in me and supporting me during every step and turn I took on this journey. I came to Cambridge without a friend and knowing only little English. Sasha gave me the trust I needed by putting my disadvantages aside and setting up the foundation to help me fulfil my full potential as a scientist. Thank you for trusting me by giving me free reign to work on other projects as well as my PhD and more then all, for being patient, forgiving me for my mistakes and challenging me intellectually. Thank you for all the time and the endless discussions we've had in the office, lab, field, conferences, group meetings (and the fun group meetings), breakfasts, coffees, lunches and dinners; every single meeting with you was fun and I have learned so much from you on a scientific level, as well as on a personal level. I will forever be grateful for it!

Thanks for Dr. Orit Sivan, from Ben Guriun University of the Negev (Israel), who has always supported me and pushes me forward and escorts me in so many accessions. Thank you for welcoming me into your lab on my every visit to Israel. To Prof. Barak Herut, the head of the Israel Oceanographic and Limnological Research, who always helped me in the field, Tanja Bosak and Shuhei Ono from Massachusetts Institute of Technology, who have had me over for 6 months overall for my pure culture project. Thank you all for being a bottomless pit of knowledge and experience. I would like also to thank to my collage tutor Dr. Nicholas J. Butterfield for help me to get alone in college and in the department and to my 'academic friends' Prof. David Hodell and Dr. Jerome Neufeld for endless discussions.

Thanks for Dr. Vicky F.C. Rennie for setting up the Elemental Analyser and guiding me on how to use it; it was indeed a goldmine. This thesis also could not have been done without the technical support of Efrat Eliani-Russak from Ben Gurion University of the Negev, James Rolfe from the Godwin Laboratory at the University of Cambridge and Bill Olszewski from Massachusetts Institute of Technology Stable Isotope Geobiology Laboratory. Thanks for Dr. David Pargament and Philip Rubinzaft from the Yarkon River Authority as well as to the captain and crew of the R/V Shikmona and Yaron Gertner's research assistant from the Israel Oceanographic and Limnological Research Institute, and the on-board technical and scientific personnel, the captain and crew of E/V Nautilus for their assistance during field sampling.

A special mention to Nadia Mokdad, one of my first friends in the UK, who has always been there for me to listen to my problems and to help me in times of needs. In addition, I want to thank all my lab friends and colleagues: Harold Bradbury, Alicia Davies, Dr. Xiaole Sun, Jennifer Mills, Dr. Andrea Erhardt, Chin Yik Lin, Dr. Vicky Rennie and Dr. Sambuddha Misra from Cambridge University, Itay Bar-Or, Michal Adler, Dr. Naama Avrahamov, Dr. Amos Russak, Elan Levy, Dr. Eyal Wurgaft, Hanni Leibowitz and Efrat Eliani-Russak from BGU and Irit and Yuval Tal, David Wang, Dr. Harry Oduro and Sharon Newman from MIT. Thanks to my parents, my brother and my sister for basically everything.

Finally, I want to thank the moon of my life, Serena Povia for the moral, emotional and even technical support, and for her affection. Without her I probably would have not been able to reach this point and to write these words.

Almost every PhD candidate in this day and age will acknowledge how hard and stressful it can be to complete your PhD. This becomes orders of magnitudes harder when one comes to a new place with an unfamiliar culture and language, leavening family and friends behind. My way of dealing with this was hours and hours of playing the guitar. With time, this had grown to be my first ever-recorded album. As art is a big part of my life, I believe that this fruit of my labor is an integral part of my thesis, which I hereby submit.

My first album is entitled "*Manuscript*" and each track is named after a section in a scientific paper. I welcome the readers of this thesis to take some time to enjoy my music while, before and after reading my thesis.

Table of Contents:

Available on: https://soundcloud.com/gilad-antler/sets/manuscript-gilad-antler

Table of Contents

List of Figures

List of Tables

Table 1: List of abbreviation

AE	Apparent equilibrium
AMP	Adenosine Mono-phosphate
ANME	anaerobic methanotrophic
AOM	Anaerobic Oxidation of Methane
APS	Adenosine phosphosulfate
CDT	Canyon Diablo Troilite
csSRR	Cell Specific Sulfate Reduction Rate
DIC	Dissolved Inorganic Carbon
MSR	Microbial Sulfate Reduction
nSRR	Net Sulfate Reduction Rate
PDB	Pee Dee Belemnite
SALP	Slop of the Apparent Linear Phase
SMOW	Standard Mean Ocean water

Chapter 1

Introduction

The carbon budget at Earth's surface determines Earth's climate; this is because the partitioning of carbon among various surface reservoirs determines how much is in the atmosphere, where it acts as the dominant greenhouse gas (e.g. Sleep and Zahnle, 2001; Walker et al., 1983; Berner et al., 1983; Berner, 2003; Raymo et al., 1988). The burial of organic carbon in shallow marine sediments represents a major removal pathway for carbon from Earth's surface environment. However, organic carbon in marine sediments may not simply be buried; organic carbon can undergo oxidation back to dissolved inorganic carbon or fermentation into methane; either oxidation of organic carbon, or turning it into methane (a gas) will prevent its ultimate burial (Aller, 2004; Froelich, et al., 1979). Production of methane is a particularly interesting fate for organic carbon in sediments because methane is a greenhouse gas that is ten times more powerful than carbon dioxide. The primary controls on the formation of methane from organic carbon in shallow marine ecosystems remain enigmatic. In sum, the fate of organic carbon, be it burial, oxidation, or methane production, in the subsurface plays an important role in the global carbon cycle and thus on climate.

1.1 Microbial respiration

Organic carbon oxidation in marine or marginal marine sediments is often tied to other biogeochemical cycles such as nitrogen, iron and sulfur (Froelich, et al., 1979; Cappellen and Wang, 1996). This is because during the oxidation of organic matter, bacteria can respire a variety of electron acceptors, including nitrogen, iron, manganese, and sulfur. The order in which these electron acceptors are used reflects the decrease in the free energy yield associated with their reduction (Figure 1.1) (Froelich, et al., 1979), the resulting changes in concentration of various elements in

the environment are shown in Figure 1.1. The largest energy yield is associated with aerobic respiration (oxidation of organic carbon with molecular oxygen - O_2), therefore as long as oxygen is available, aerobic respiration dominates the oxidation of organic carbon. In today's surface environment, oxic respiration dominates in the ocean water column, and the very top of marine sediments. Oxygen diffusion into sediments can persist a few tens of meters in the deep ocean, and a few millimetres in the shallowest sediments, before it is consumed. The depth of this oxygen penetration is a function of the supply of organic carbon to the sediments (which sets the rate of oxygen consumption) as well as the sedimentation rate (how quickly the organic carbon can be buried).

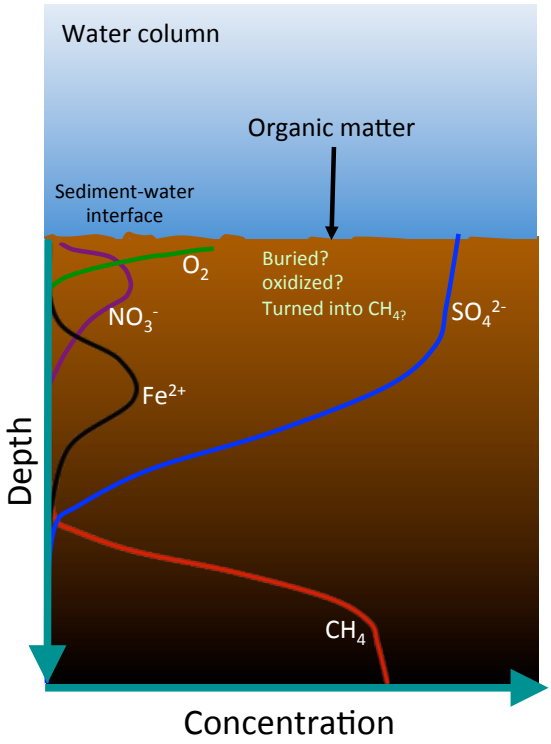

Figure 1.1: The order of the use of different electron acceptors as function of sediment depth redrawn from Froelich, et al. (1979)

Once oxygen is depleted in marine sediments there are a series of other electron acceptors that microbial populations can respire to continue to oxidize organic matter. They are used in decreasing energy yield, first denitrification (NO_3^- is the electron acceptor), then manganese and iron reduction (Mn^{4+} and Fe^{3+} are the electron

acceptors), followed by sulfate reduction (aqueous SO_4^{2-}) and finally organic matter fermentation into methane (methanogenesis) (Figure 1.1 - Froelich, et al., 1979; Berner, 1980).

Sulfate reduction, also known as dissimilatory sulfate reduction, microbial sulfate reduction and bacterial sulfate reduction in the literature, is responsible for the majority of organic matter oxidation in marine sediments due to the high concentration of sulfate in the ocean (at least two order of magnitude more abundant than oxygen at the sea surface - Kasten and Jørgensen, 2000). In addition, the methane produced during methanogenesis in marine sediments is nearly quantitatively consumed by archaea that couple this oxidation to microbial sulfate reduction (Boetius, et al., 2000; Niewöhner, et al., 1998). Of particular importance, therefore, for understanding the fate of organic carbon within sediments is to understand the microbial utilization of sulfur. Despite its important role, the dynamics of microbial sulfate reduction and the possible redox couplings of sulfate to other electron acceptors, such iron, remain enigmatic. The main goal of this thesis is to investigate the dynamics of microbial sulfate reduction and the coupling of sulfate reduction to methane production and oxidation using a geochemical approach. Specifically, I focus on the geochemical, particularly isotope, composition of pore water (defined as the water occupying the spaces between sediment particles) combined with reactive-transport and other microbial mechanistic models.

1.2 Dissimilatory microbial sulfate reduction

At a cellular level, the biochemical steps during microbial sulfate reduction have been investigated over the past 50 years (Harrison and Thode, 1958; Kaplan and Rittenberg, 1963; Rees, 1973; Farquhar et al., 2003; Brunner and Bernasconi, 2005; Wortmann, et al, 2007; Sim et al., 2011a). During microbial sulfate reduction, bacteria respire sulfate and produce sulfide as an end product simplified as:

$$SO_4^{2-} + 2CH_2O \rightarrow 2HCO^-_3 + H_2S \qquad (1.1)$$

This process consists of at least four major intracellular steps (e.g. Rees, 1973; Canfield, 2001a and Figure 1.2): during step 1, the extracellular sulfate is brought into the cell; in step 2, the sulfate is activated with adenosine triphosphate (ATP) to form Adenosine 5' Phosphosulfate (APS); in step 3, the APS is reduced to sulfite (SO_3^{2-}); in the 4 step sulfite (SO_3^{2-}) reduced to another sulfur intermediate (S_nO_n); and in step 5 this sulfur intermediate is reduced to sulfide. It is generally assumed that all four steps are reversible (e.g. Brunner and Bernasconi, 2005; Eckert et al., 2011). The reduction of sulfite to sulfide (step 4 through 5) remains the most enigmatic, and may occur in one step with the enzyme dissimilatory sulfite reductase or through the multi-step trithionite pathway producing several other intermediates (e.g. trithionate ($S_3O_6^{2-}$) and thiosulfate ($S_2O_3^{2-}$) -- Kobayashi et al. 1969; Brunner and Bernasconi, 2005; Sim et al. 2011a; Bradley et al., 2011).

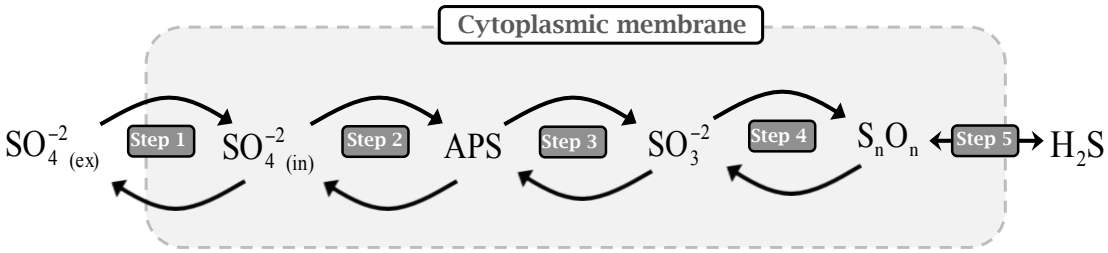

Figure 1.2: The steps of microbial sulfate reduction.

Given that each of the four steps is reversible, understanding the relative forward and backward fluxes at each step and how these fluxes relate to the overall rate of sulfate reduction, is critical for understanding the link between the rate of microbial sulfate reduction and the rate of organic matter oxidation. Changes in environmental conditions (e.g. temperature, carbon substrate, pressure) likely impact the relative forward and backward fluxes at each step within the cell as well as the overall rate of microbial sulfate reduction, but the relative role of these environmental factors in the natural environment remains elusive. Within the marine subsurface, measurements of sulfate concentrations in sedimentary pore water and subsequent diffusion-reaction modelling of the rate of sulfate depletion with depth can be used for calculating the overall rate of sulfate reduction below the ocean floor (e.g. Berner, 1980; D'Hondt et al., 2004; Wortmann, 2006; Wortmann et al., 2007; Bowles et al.,

2014). These sulfate concentration profiles alone, however, cannot provide details about how the individual biochemical steps at a cellular or community level may vary with depth or under different environmental conditions or how many times sulfate may be cycled before it is ultimately reduced.

1.3 Other sulfur redox reactions

The end product of microbial sulfate reduction is hydrogen sulfide (H_2S). Ultimately, this reduced form of sulfur has two possible fates: burial as pyrite or oxidation back to sulfate or other intermediate valence state sulfur species. In the presence of dissolved ferrous iron, sulfide will react quickly to form iron monosulfide (FeS). This amorphous mineral, in the presence of more sulfide will react to form pyrite and release hydrogen gas (Luther, 1991):

$$FeS + H_2S \rightarrow FeS_2 + H_2 \qquad (1.2)$$

Alternatively, in the presence of an oxidant (such as oxygen, ferric iron, nitrate or manganese) this sulfide can undergo chemical or microbial oxidation to produce sulfate and/or a variety of sulfur intermediates (such as thiosulfate-- $S_2O_3^{2-}$, zero-valent sulfur-- S^0, or sulfite-- SO_3^{2-}).

In marine sediments, it has been demonstrated that hydrogen sulfide (H_2S) can also reduce iron oxide minerals to form ferrous iron and elemental sulfur (e.g. Pyzik and Sommer, 1981; Yao and Millero, 1996; Canfield, 1989):

$$2FeOOH + H_2S + 4H^+ \rightarrow 2Fe^{2+} + S^0 + 5H_2O \qquad (1.3)$$

This elemental sulfur production is one example of the way that intermediate valence state sulfur species can be produced during sedimentary sulfur cycling. These intermediates of sulfide oxidation, produced by both chemical and biological processes, may undergo further oxidation, reduction and disproportionation. Microbial disproportionation of sulfur intermediates is a metabolic process in which sulfur serves as the electron donor as well as the electron acceptor in the same

reaction. Microbial disproportionation produces both hydrogen sulfide and sulfate (e.g. Bak and Cypionka, 1987; Thamdrup et al., 1993):

$$4S^0 + 4H_2O \rightarrow 3H_2S + SO_4^{2-} + 2H^+ \quad (1.4)$$

$$S_2O_3^{2-} + H_2O \rightarrow H_2S + SO_4^{2-} \quad (1.5)$$

$$4SO_3^{2-} + 2H^+ \rightarrow H_2S + 3SO_4^{2-} \quad (1.6)$$

The combination of chemical oxidation and microbial disproportionation of intermediates of sulfide oxidation may result in sulfate formation (Figure 1.3), even in the absence of electron acceptors stronger than iron.

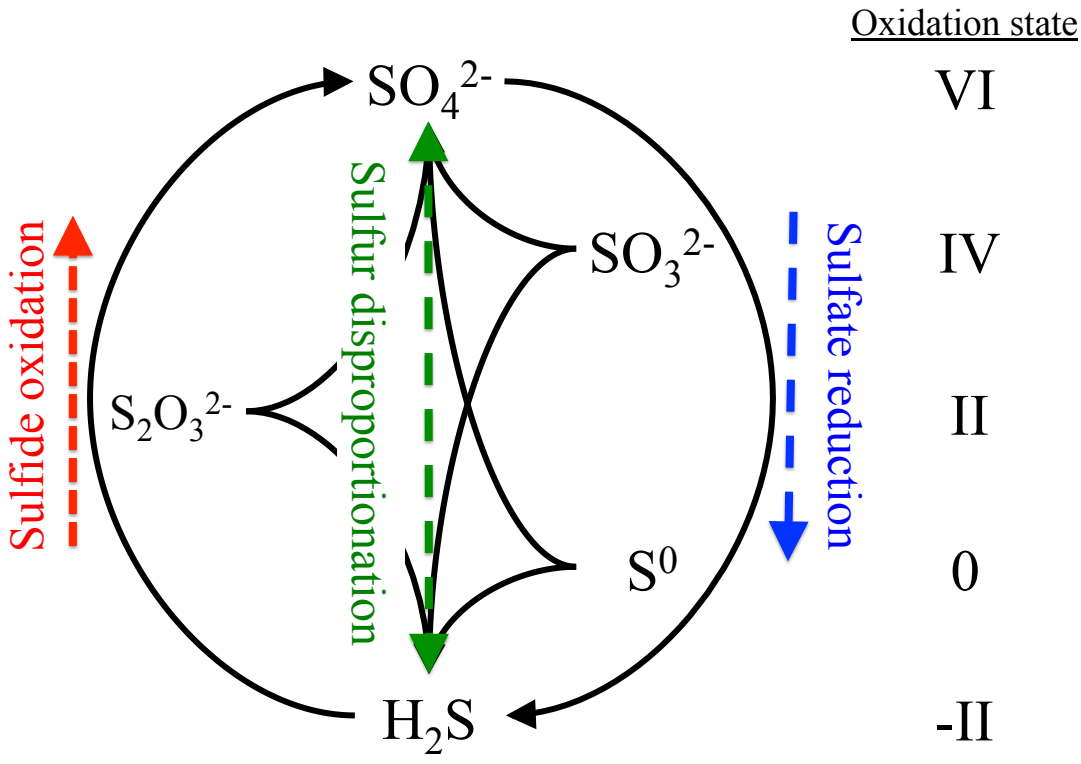

Figure 1.3: Distribution and fate of the different sulfur species intermediates in marine sediments (adapted from Zopfi et al., 2004)

1.4 Methanogenesis

Any organic matter that is not oxidized aerobically or anaerobically can undergo further reduction, leading to the formation of methane through process called methanogenesis (e.g. Whiticar et al., 1986). In freshwater sediments the dominant pathway for methanogenesis is acetate fermentation (acetoclastic methanogenesis, Eq. 1.7), whereas in marine sediments it is CO_2 reduction by hydrogen (hydrogenetic methanogenesis, Eq. 1.8) (Whiticar et al., 1986):

$$CH_3COOH \rightarrow CO_2 + CH_4 \qquad (1.7)$$

$$4H_2 + CO_2 \rightarrow 2H_2O + CH_4 \qquad (1.8)$$

One of the factors controlling the fate of organic carbon is the competition within marine sediments between methane-producing microorganisms and sulfate reducing bacteria for common substrates such as hydrogen and acetate (Ward et al., 1985). It is commonly assumed that in the presence of sulfate, sulfate reduction will out-compete methanogenesis, restricting this process to deeper depths in the sediments (e.g. Lovley and Klug, 1983). This suggests that the depth of methanogenesis depends primarily on the type of organic matter and the sulfate concentrations within the pore water of the sediments. In sediments with larger amounts of organic carbon, the zone of methanogenesis may be located a few centimeters below the sediment water interface, while in sediments with less organic carbon, the zone of methanogenesis can be located tens or hundreds of meters below sediment-water interface (Valentine, 2002; Sivan et al., 2007).

1.5 Sulfate-driven anaerobic methane oxidation

Upwardly diffusing methane can be oxidized microbially (called methanotrophy), both aerobically (via oxygen— e.g. Cicerone and Oremland, 1988) and anaerobically (anaerobic oxidation of methane – AOM—e.g. Martens and Berner,

1974; Hinrichs et al., 1999; Boetius et al., 2000; Milucka et al., 2012). In marine and marginal marine sediments, AOM has been identified as the main process consuming methane within sediments, and this methane oxidation is primarily coupled to sulfate reduction (hereafter called sulfate-driven AOM) (Eq. 1.9—e.g. Martens and Berner, 1974; Barnes and Goldberg, 1976; Reeburgh, 1976):

$$SO_4^{2-} + CH_4 \rightarrow HCO_3^- + HS^- + H_2O \qquad (1.9)$$

Sulfate-driven AOM often results in a geochemically detectable transition zone at the boundary between methane diffusing upwardly through the network of sedimentary pore water, intersecting with sulfate, diffusing downwardly from the overlying ocean (e.g. Niewöhner et al., 1998). Although marine sediments harbour the largest natural reservoir of methane on the planet, methane emissions from marine sediments are an order of magnitude smaller than those from rice paddies or terrestrial wetlands; this is because of sulfate-driven AOM, which nearly quantitatively consumes all the naturally produced methane (Wuebbles and Hayhoe, 2002). The fact that the vast majority of methane in marine sediments is oxidized through sulfate-driven AOM means that the Earth's oceans are not a major source of this potent greenhouse gas (Reeburgh, 2007).

Sulfate-driven AOM was first identified using evidence from sedimentary geochemical profiles (Martens and Berner, 1974; Barnes and Goldberg, 1976; Reeburgh, 1976). This process was initially controversial among microbiologists, because neither the responsible organism nor the mechanism was identified. About twenty years ago, field and laboratory studies demonstrated coupling between methanogens and sulfate reducers (Hoehler et al., 1994). Later, microbiologists and geochemists showed that consortia of archaea and bacteria are involved in AOM in some seep environments (Hinrichs et al., 1999; Boetius et al., 2000; Orphan et al., 2001), and that at least three groups of archaea may perform AOM (named ANME-1, ANME-2, and ANME-3) associated with sulfate reducing bacteria (Boetius et al., 2000; Orphan et al., 2002; Niemann et al., 2006). It was suggested that the archaea are responsible for the methane oxidation while the sulfate reducing bacteria separately reduce the sulfate. Recently it was shown that some ANMEs are able to oxidize

methane and reduce sulfate alone and the bacteria-archaea consortia may not be required (Milucka et al., 2012).

Some specifics of sulfate-driven AOM and its link to the subsurface sedimentary sulfur cycle, however, remain enigmatic. For instance, if we consider the proposed consortia for sulfate-driven AOM, it is still unclear what drives the coupling between sulfate reducers and methane oxidizers and how this is energetically favourable for each. If we consider, on the other hand, that a single ANME performs both sulfate reduction and methane oxidation (Milucka et al., 2012—Figure 1.4), we do not yet know how prevalent this is in the natural environment and the role of key intermediate chemical species in this pathway of sulfate-driven AOM, and how they may catalyse this microbial process. Additionally, sulfate-reducing bacteria can oxidize sedimentary organic matter, yet several studies have shown that when methane is present, all available sulfate is reduced through the less energetically favourable pathway of AOM (Kasten and Jørgensen, 2000; Niewöhner et al., 1998; Sivan et al., 2007). The lack of answers to these questions limits our understanding of the subsurface sulfur cycle and the crucial coupling to methanotrophy.

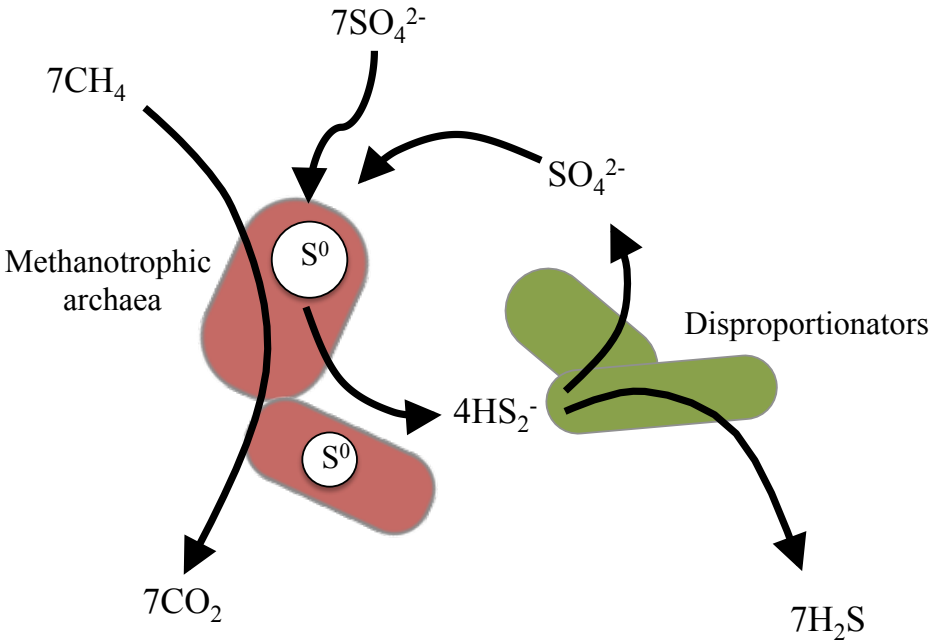

Figure 1.4: The pathway of sulfate-driven anaerobic methane oxidation. After Milucka et al., 2012

In summary, within an anoxic environment, the fate of sulfur and the intermediate-valence-state sulfur species is likely to be a key factor in dictating the fate of subsurface organic carbon. Understanding the sulfur dynamic in marine sediments is an important factor in the large-scale global carbon and the redox condition of the surface ocean. In this thesis, I will explore the dynamics of microbial sulfate reduction and its coupling to organic matter oxidation in both pure culture batch experiment and in pore water from different marine and marginal marine settings. The main geochemical tool that I will employ is the sulfur and oxygen isotopic composition of sulfate.

1.6 Pore water geochemistry profiles

Pore water is water that occupies the pore space in sediment – it is also called pore fluid and I will use these two terms interchangeably throughout the thesis. Interpreting the change in the chemical composition of pore water can reveal different chemical and biological reactions that are producing or consuming various elements, and numerical modelling allows us to explore the rates of these reactions (e.g. Berner, 1980; Berg et al., 1998). Regarding sulfate, three types of sulfate concentration profile shapes have been observed in subsurface sedimentary pore fluids; linear, concave-down and concave-up (Figure 1.5). A linear concentration profile (where the second derivative is zero) is found in diffusion-controlled systems, where sulfate diffuses from seawater concentrations at the sediment-water interface to low concentrations at depth. In this case, sulfate is being consumed in a single zone, which is often coupled to methane oxidation. When the profile is concave down, it is interpreted as continual consumption of sulfate with depth below the sea floor. In this case the second derivative of the best-fit curve through the pore fluid data yields a constant value, which is the rate of sulfate consumption per volume of sediment with depth. Concentration profiles that are concave up (red line in Figure 1.5) are less frequently found for sulfate and usually relate to sulfide oxidation or evaporate dissolution.

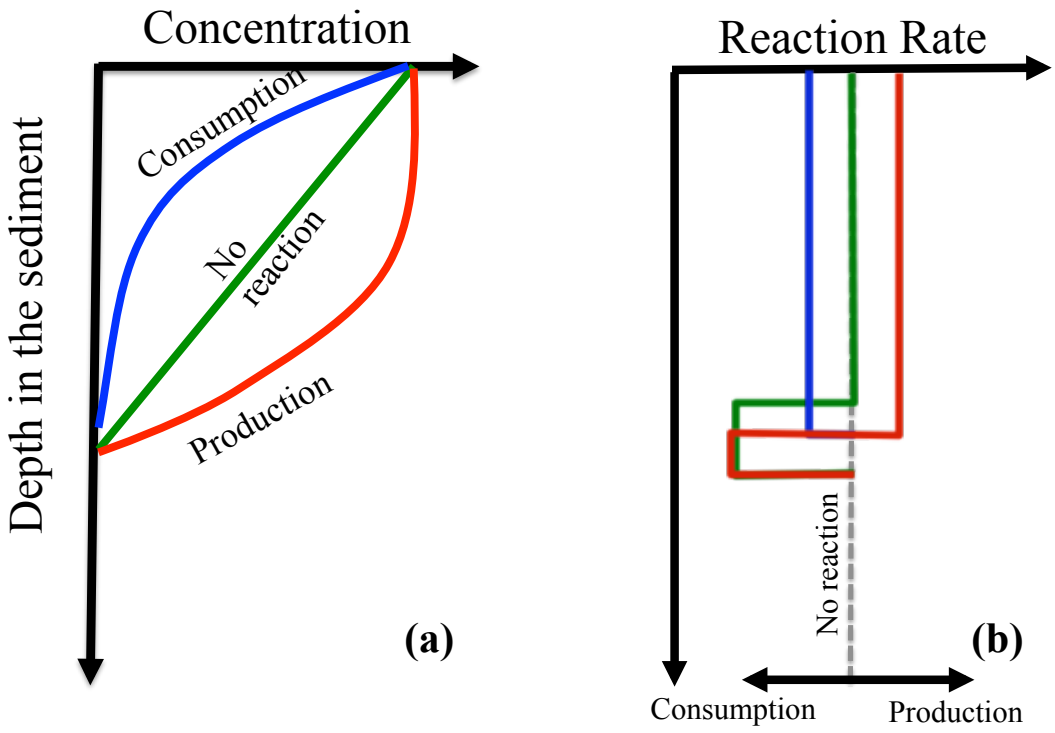

Figure 1.5: Schematic concentration profiles and the corresponding reaction rate (in this case sulfate) through sediment cores.

Since pore water cannot be considered as a closed system, the concentration of different components is not only dependent on the rate of production or consumption but also only on the rate of transport between the different layers of sediment. Therefore, a mass-conservation model that describes the pore water depth profiles needs to be employed in order to account for this rate of transport – largely through diffusion and advection. The basic conservation equation for the concentration of a chemical species 'i' in pore water (mol·L^{-3}) has a general form, as developed by Berner (1980), that includes terms for diffusion, sedimentation advection and reactions, respectively:

$$\frac{\partial \varphi C_i}{\partial t} = \varphi \cdot \frac{\partial}{\partial z} \cdot \left(D_s \frac{\partial C_i}{\partial z} \right) - \varphi \cdot (U+\omega) \frac{\partial C_i}{\partial z} - \sum R_i \quad (1.10)$$

where C_i is the concentration of solid or liquid component i in mass per unit volume of total sediment, φ is the porosity, t is time, z is the layer depth, Ds is the

diffusion coefficient in area of total sediments per unit time, U is the velocity of flow relative to the sediments-water interface, ω is the rate of burial of the layer below the sediments-water interface and R is the reactions affecting i. It is through the use of Equation 1.10 that geochemical pore fluid profiles can be modelled to understand rate of both reaction and transport of elements within the subsurface.

1.7 Process-based stable isotope geochemistry

Stable isotopes can be a useful tool for the study of a variety of microbially-mediated processes within marine sediments. Isotopes, which are 'versions' of an element with a different number of neutrons in the nucleus, do not necessarily react at the same rate in various chemical and biological reactions, therefore measuring the ratio among various isotopes and how it changes over the course of a chemical or biological reaction provides independent information about the nature of the reaction. In this work, the primary tool I use to explore the process of sulfate reduction and its coupling to methane oxidation are sulfur and oxygen isotopes in dissolved sulfate together with carbon isotopes in dissolved inorganic carbon and methane.

Stable isotopes (for an element X), are commonly reported using δ notation, give as:

$$\delta X = \left(\frac{R_{sample} - R_{std}}{R_{std}} \right) \cdot 1000 \quad (1.11)$$

Where R_{sample} and R_{std} are the ratios between the heavier and the lighter isotopes in a sample and an internationally recognized standard, respectively.

Delta notation is used for reporting isotope ratios because the variation in the ratio is largely in the 'parts per thousand' or permil, order of magnitude. Use of ratios normalized to the same standard allow laboratories around the world to compare analyses.

The fractionation factor (α), or magnitude by which isotopes are partitioned between two reservoirs (here between reservoir A and B) is defined as:

$$\alpha = \frac{1000+\delta A}{1000+\delta B} \quad (1.12)$$

and the isotope fractionation(ε), given in permil (‰), defined as:

$$\varepsilon = (\alpha - 1) \cdot 1000 \quad (1.13)$$

Isotopes of a given element can be partitioned, or fractionated, in the natural environment both through kinetic and equilibrium processes: Kinetic isotope fractionation occurs because each isotope reacts at a different rate during a chemical reaction. Typically, the lighter isotope (less neutrons, for example carbon with 6 neutrons – ^{12}C) reacts more quickly than the heavier isotope (for example carbon with 7 neutrons ^{13}C). Therefore as a reaction progresses, the product of the reaction concentrates the 'light' isotope and the reactant pool gets progressively enriched in the 'heavy' isotope. The second mechanism by which isotopes can be partitioned, or fractionated, is equilibrium isotope fractionation, which is the partial separation of isotopes between two molecules that are found in chemical, or isotopic, equilibrium. In equilibrium isotope fractionation the isotopes are distributed among various chemical species such that the energy of the system is minimized.

The total natural abundance of sulfur, oxygen isotopes are given in Table 1. The reference standard for sulfur isotopes is CDT (Canyon Diablo Troilite, a sample from a meteorite found in a crater in Arizona, US), the reference standard for oxygen isotopes is SMOW (Standard Mean Ocean Water) and the reference standard for carbon isotopes is PDB (Pee Dee Belemnite).

Table 1.1: Isotopic abundance and relative atomic mass (amu) of stable isotope of sulfur and oxygen.

Sulfur Isotopes	Abundance (%)	Mass (amu)
^{32}S	95.039	31.97207
^{33}S	0.748	32.97146
^{34}S	4.197	33.96786
^{36}S	0.014	35.96708

Oxygen Isotopes	Abundance (%)	Mass (amu)
^{16}O	99.759	15.99491
^{17}O	0.037	16.99914
^{18}O	0.204	17.99916

1.7.1 Sulfate and oxygen isotopes in dissolved sulfate

The use of isotope geochemistry, specifically the stable sulfur ($^{33}S/^{32}S$ and $^{34}S/^{32}S$) and oxygen ($^{18}O/^{16}O$) isotope ratios, has helped reveal some of the dynamics of the intracellular steps during MSR. Given that every step during MSR partitions each sulfate isotopologue (A molecular entity that differs only in isotopic composition) in a different manner, the isotope fractionations of the major or minor sulfur or oxygen isotopes in the extracellular sulfate pool should reflect the dynamics between the different steps and their relative reversibilities (Figure 1.2). Most studies using isotopes to investigate MSR exploit the ratios of ^{32}S and ^{34}S measured in sulfate, sulfide, or sulfur intermediates (e.g. Canfield et al., 2001b; 2006; 2010; Kamyshny et al., 2011; Knossow et al., 2015; Zerkle et al., 2010). Studies focusing on the fractionation of the ^{34}S isotope from the ^{32}S isotope during MSR have found that most of the enzymatic steps during MSR prefer the ^{32}S isotope, distilling ^{32}S into the produced sulfide pool, leaving ^{34}S behind in a Rayleigh-type isotope distillation. The magnitude of sulfur isotope fractionation during MSR can be as high as ~70 ‰ for $\delta^{34}S_{SO4}$ (Wortmann et al., 2007; Canfield et al., 2010; Sim et al., 2011a), as sulfide and sulfate approach isotopic equilibrium (Szabo et al., 1950; Tudge & Thode, 1950; Farquhar et al., 2003; Johnston et al., 2007; Leavitt et al., 2013; Wing and Halevy, 2014).

More recently studies have employed coupled ^{32}S, ^{33}S, and ^{34}S isotopes (e.g. Farquhar et al., 2003; 2008; Zerkle et al., 2010; Sim et al., 2011a; 2011b; Leavitt et al., 2013; 2014; Ono et al., 2006) or $^{34}S/^{32}S$ and $^{18}O/^{16}O$ isotope ratios (Brunner et al., 2005; 2012; Wortmann et al., 2007; Farquhar et al., 2008; Turchyn et al., 2006; 2010). Under strictly mass dependent fractionation, the magnitude of the $\delta^{33}S_{SO4}$ fractionation is around half (0.5147 at 25ºC-- Farquhar et al., 2003) of the fractionation of $\delta^{34}S_{SO4}$. Over the last 60 years, studies have shown that the magnitude of the sulfur isotope fractionation, for either ^{34}S or ^{33}S versus ^{32}S is a function of microbial metabolism and carbon source (e.g. Sim, et al., 2011b; Brüchert, 2004), the amount of sulfate available (e.g. Canfield, 2004; Habicht et al., 2002; Farquhar et al., 2003), the temperature (e.g. Canfield, et al., 2006) and the sulfate reduction rate (e.g. Canfield, et al., 2001a; Leavitt et al., 2013; Sim et al., 2011a;2011b).

Oxygen isotopes in dissolved sulfate ($\delta^{18}O_{SO4}$) also increase as MSR progresses, but often reach isotopic equilibrium with water and cease increasing further (Figure 1.6; Fritz et al, 1989; Böttcher et al., 1998, 1999; Turchyn et al, 2006; 2010 Wortmann, et al, 2007; Aller et al, 2010; Zeebe, 2010). Pure culture studies have shown that oxygen atoms from water are incorporated into sulfate during MSR (Fritz et al, 1989; Mizutani and Rafter 1973; Brunner et al., 2005; Mangalo et al, 2007; Mangalo et al, 2008) much more rapidly than would be expected by abiotic oxygen isotope exchange between water and sulfate under normal surface conditions (pH>1, temperature <100ºC) (Chiba and Sakai 1985; Lloyd, 1968; Rennie and Turchyn, 2014). This rapid oxygen isotope exchange during MSR is attributed to the intracellular exchange of oxygen atoms between sulfur intermediate species such as sulfite and water (Mizutani and Rafter, 1973; Fritz, et al., 1989) and occurs over time scale of minutes (Betts and Voss, 1970; Horner and Connick, 2003; Wankel et al., 2014; Müller et al., 2013). If a portion of sulfate that is brought into the cell is partially reduced and then reoxidized back to the residual sulfate pool, this exchange of oxygen isotopes between sulfate and water can be measured. The observed (and modelled) oxygen isotope enrichment over the isotopic composition of the water ($\delta^{18}O_{SO4}$- $\delta^{18}O_{H2O}$) between 22 to 30‰, reflecting this intracellular oxygen isotope exchange (e.g. Böttcher et al., 1998, 1999; Turchyn et al, 2006; 2010 Wortmann et al, 2007; Zeebe, 2010; Knöller et al., 2006).

In some experiments with natural populations and in the environment, data comparing $\delta^{18}O_{SO4}$ and $\delta^{34}S_{SO4}$ show a clear linear pattern as MSR progresses demonstrating that both oxygen and sulfur isotopes undergo kinetic isotope fractionation and the aforementioned isotope equilibrium with water is not always immediately observed (e.g. Sivan et al., 2014). The magnitude of this kinetic isotope fractionation for $\delta^{18}O_{SO4}$ has been suggested to be 25% of the magnitude of $\delta^{34}S_{SO4}$ (Rafter and Mizutani 1967; Mandernack et al., 2003). Therefore, the oxygen isotope fractionation observed during MSR is understood to be a combination of the kinetic isotope effect associated with each of steps during MSR (similar to sulfur isotopes) and the equilibration of oxygen isotopes between sulfur species in intermediate valence state and water, and the contribution of these sulfur species to the extracellular sulfate pool.

Interpreting the relative evolution of the $\delta^{18}O_{SO4}$ and the $\delta^{34}S_{SO4}$ in the extracellular sulfate pool during microbial sulfate reduction in natural environments, and what this relative evolution tells us about the enzymatic steps during sulfate reduction remains confounding. My hypothesis is that there is an incredible amount that can be learned about the mechanism of microbial sulfate reduction and its coupling to the carbon cycle by exploring how this relative evolution varies in the environment. Figure 1.6 shows schematically how pore water sulfate and sulfur and oxygen isotope profiles often look in nature, where pore water sulfate concentrations decrease below the sediment-water interface and the oxygen and sulfur isotope ratios of sulfate increase, but may evolve differently relative to one another. One question is what are the factors controlling microbial sulfate reduction in natural environments when the coupled sulfur and oxygen isotopes increase linearly (Trend A), compared to when they are decoupled and oxygen isotopes are seen to plateau (Trend B)? A second problem is that the majority of our understanding of the biochemical steps during microbial sulfate reduction comes from pure culture studies; how does this understanding translate, if at all, to the study of microbial sulfate reduction in the natural environment?

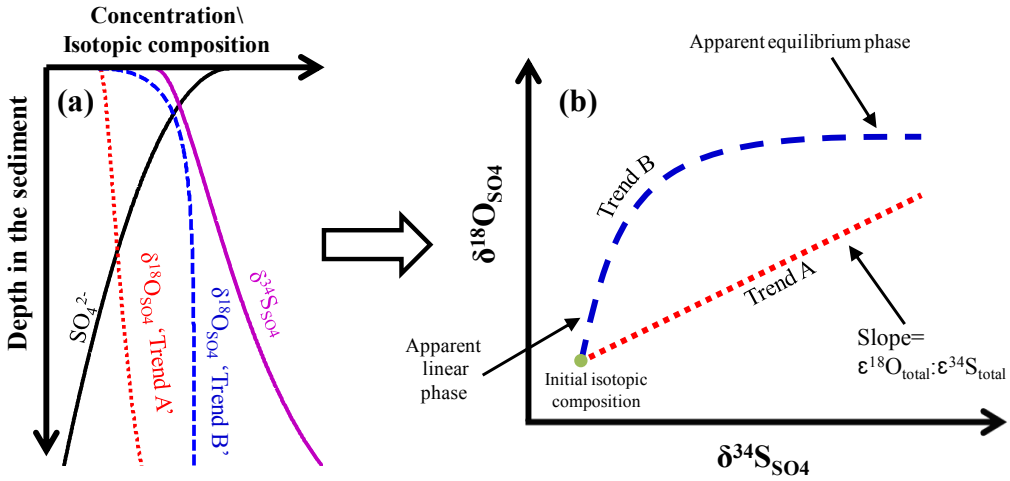

Figure 1.6: Schematic possible behaviour of sulfate during microbial sulfate reduction as SO_4^{-2}, $\delta^{18}O_{SO4}$ and $\delta^{34}S_{SO4}$ profiles (a) and $\delta^{18}O_{SO4}$ vs. $\delta^{34}S_{SO4}$ (b). 'Trend A' shows that $\delta^{18}O_{SO4}$ and $\delta^{34}S_{SO4}$ increase at a constant ratio, while sulfate reduction propagates with depth (e.g. Aharon and Fu, 2000). 'Trend B' shows an increase in $\delta^{34}S_{SO4}$ and $\delta^{18}O_{SO4}$ values at the onset of the curve, $\delta^{18}O_{SO4}$ reaches equilibrium values as sulfate reduction progresses with depth while $\delta^{34}S_{SO4}$ continue to increase. Redrawn from Antler et al., 2013.

It has been suggested that this relative evolution of the $\delta^{18}O_{SO4}$ vs. $\delta^{34}S_{SO4}$ during microbial sulfate reduction should be connected to the overall sulfate reduction rate (Böttcher et al., 1998; 1999; Aharon and Fu, 2000, Brunner et al., 2005) where the steeper the slope on a plot of $\delta^{18}O_{SO4}$ vs. $\delta^{34}S_{SO4}$ (the plot on the right in Figure 1.6) the slower the sulfate reduction rate. This suggestion was elaborated upon by Brunner et al. (2005), who formulated a model for mass flow during microbial sulfate reduction. In this work, Brunner et al. (2005) deduced that the overall sulfate reduction rate is important for the relative evolution of $\delta^{18}O_{SO4}$ and $\delta^{34}S_{SO4}$, but that the rate of oxygen isotope exchange between sulfur intermediates and water, and the relative forward and backward fluxes at each step further modifies the evolution of $\delta^{18}O_{SO4}$ vs. $\delta^{34}S_{SO4}$. In my M.Sc thesis and the major paper that came out of that work (Antler et al., 2013), I demonstrated this correlation by both measuring and then compiling sulfur and oxygen isotope data in sulfate from globally distributed marine and marginal marine pore water, where the sulfate reduction rate varies over seven

orders of magnitudes (Figure 1.7—after Antler et al., 2013). In my PhD I am exploring this relationship further with pure culture sulfate reducers and specifically during sulfate-driven anaerobic methane oxidation.

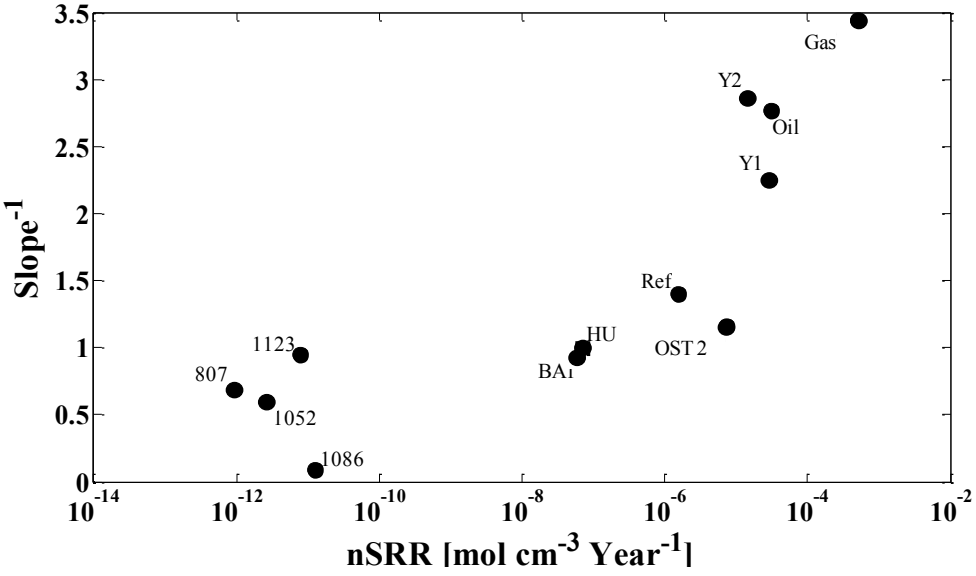

Figure 1.7: The inverse of the slope of between $\delta^{18}O_{SO4}$ vs. $\delta^{34}S_{SO4}$ plotted vresus the average net sulfate reduction rate (nSRR), as deduced from our data and worldwide pore water profiles. The labels of each point indicate the site's name (After Antler et al., 2013).

1.7.2 Carbon isotopes

Carbon isotopes are another geochemical tool that yield information on the subsurface processing of organic carbon. Specifically, carbon isotopes provide a good constraint on the depth distribution and location of methane production and methane consumption because of the large carbon isotope fractionation associated with both these processes (e.g. Whiticar, 1999; Borowski et al., 2000). During methanogenesis, ^{12}C is strongly partitioned into methane; the $\delta^{13}C$ of the methane produced can be between -50‰ to -100‰. In contrast, the residual dissolved inorganic carbon (DIC) pool becomes highly enriched in ^{13}C, occasionally by as much as 50‰ to 70‰. Oxidizing this methane during AOM on the other hand, results in

^{13}C-depleted dissolved inorganic carbon and slightly heavier δ^{13}C values of the residual methane, due to both a fractionation of 0‰ to 10‰ during methane oxidation and to the initial δ^{13}C value of the methane itself (Alperin et al., 1988; Martens et al., 1999). Therefore, in sedimentary environments where methane is being produced and consumed, the δ^{13}C of dissolved inorganic carbon in the pore water typically follows a depth profile where it decreases from the surface to the zone of AOM and then increases below in the zone where methane is being produced (e.g. Blair and Aller, 1995; Sivan et al., 2007; Malinverno and Pohlman, 2011—Figure 1.8).

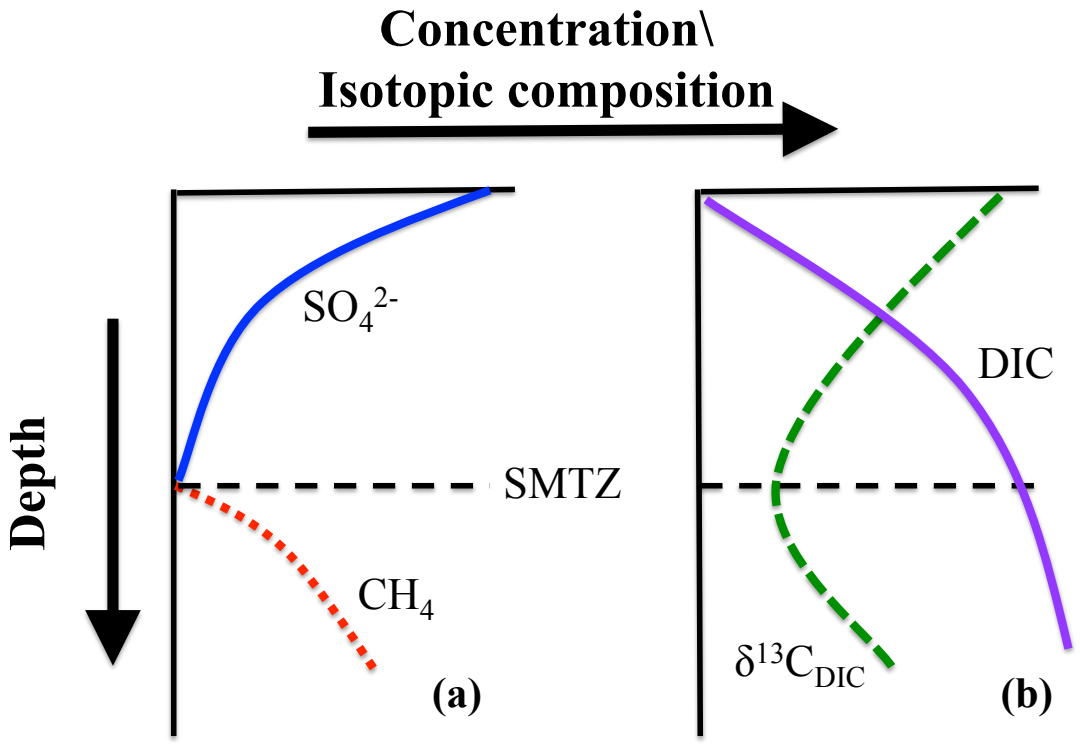

Figure 1.8: Schematic sulfate and methane concentrations profile (a) and DIC concentration and $\delta^{13}C_{DIC}$ profile (b).

1.8 Thesis objectives

Given the wide importance of the redox sulfur cycle in the oxidation of organic carbon, my thesis was built around using a geochemical approach to explore the coupling of microbial sulfate reduction to the methane cycle. The main goal of this thesis was to study the mechanism of microbial sulfate reduction and sulfate-driven AOM using $\delta^{18}O_{SO4}$ and $\delta^{34}S_{SO4}$.

The specific objectives of my PhD thesis are:

- To generate a combined model for $\delta^{18}O_{SO4}$ and $\delta^{34}S_{SO4}$ during microbial sulfate reduction.
- To test how the relationship between $\delta^{18}O_{SO4}$ and $\delta^{34}S_{SO4}$ differ during microbial sulfate reduction coupled to organic carbon oxidation and sulfate-driven AOM.
- To study the coupling between sulfate and methane in the sediment transition zone and understand how it is linked to methane fluxes.

Thesis roadmap

The remaining four chapters of my thesis comprise the modelling, laboratory and field studies undertaken as part of my PhD. I will start in chapter two with a numerical mass-balance model for sulfur and oxygen isotopes during microbial sulfate reduction and sulfate-driven AOM; this model is applied to the natural environment and to pure culture studies through the rest of the thesis. In Chapter 3, I will explore, through pure culture experiments, the dynamics of microbial sulfate reduction. Chapter 4 then explores the differences between microbial sulfate reduction and sulfate-driven anaerobic methane oxidation in estuarine sediments. I will take this forward in Chapter 5 to discuss and examine how the sulfate-driven AOM is different between sites with different methane fluxes. Finally I will summarize these results with a theory for what determines the slope between sulfur and oxygen isotopes in sulfate in different natural environments and how it is possibly traceable in the geological record.

Chapter 2

Models and methods

A Geochemical approach has been employed for decades to understand the physiology of microbes during MSR (Harrison and Thode, 1958, Kaplan and Rittenberg, 1964, Rees, 1973, Farquhar et al., 2003, Brunner and Bernasconi, 2005, Wortmann et al., 2007, Eckert et al., 2011 and Holler et al., 2011). The measurement and the subsequent modelling of the concentration of the reactant (sulfate) or the product (sulfide) can be use to calculate the net rate of the reaction, in this case microbial sulfate reduction. However, these measurements cannot provide information on reactions with higher complexity; such as the reversibility of individual steps in a catabolism pathway (a complex sequence of many enzymatic reactions and intermediates). In addition, in the natural environment, sulfur is involved in more biologically or abiotically mediated reactions than just MSR (see discussion in Chapter 1). Therefore, in order to understand sulfur metabolism in more comprehensive way, a different geochemical approach is required.

In this thesis I use a geochemical approach to understand microbial sulfate reduction (MSR) in both pure culture and in the natural environment. The main tools that I will employ are sulfur and oxygen isotopes in measured dissolved sulfate accompanied by measurements of other isotopes and concentrations. Before I embark on the geochemical studies, I will first summarize models that have been used to understand how sulfur and oxygen isotopes in dissolved sulfate change during MSR, including the development of a new model that comprised my MSc thesis which has been modified for my PhD and that I employ throughout the subsequent studies. I will then examine to what extent closed system models apply to sedimentary systems, which by definition are open systems. These two numerical models of microbial metabolism and exploring closed and open system behaviour I will employ to discuss my data throughout my thesis. Finally, in this chapter I will conclude by presenting the main analytical methods that I use for the rest of this thesis.

Table 2.1: Explanation of expressions

Parameter	unit	Explanation	Chapters
α	[/]	Isotope fractionation factor	2,3
$\alpha^{3x}S_{i\_j}$	[/]	Isotope fractionation factors for sulfur for the forward (i=f) and backward (i=b) reactions j (j=1...5). x=3,4,6	2,3
$\alpha^{18}O_{i\_j}$	[/]	Isotope fractionation factors for oxygen for the forward (i=f) and backward (i=b) reactions j (j=1...5).	2,3
bk	$M\ T^{-1}$	Backward flux in k th step of MSR network	2,3
csSRR	$M\ T^{-1}\ Cell^{-1}$	Cell specific sulfate reduction rate	3
D_0	$L^2\ T$	Molecular diffusion coefficients	2,5
D_s	$L^2\ T$	Effective diffusion coefficient	2,5
ε	‰	Isotopic fractionation	2,3
ε^{18}Oex	‰	*Oxygen isotopic fractionation between water and sulfur intermediates*	2,3
$E^{33}S$	‰	The deviation between the calculated value for $a^{33}S$ and the expected mass-dependent relationship between $a^{33}S$ and $a^{34}S$	2,3
$\varepsilon^{34}S_{total}$	‰	total S isotopic fractionation	2,3
fk	$M\ T^{-1}$	Forward flux in k th step of MSR network	2,3
$\phi\kappa$	[/]	Ratio between backward and forward flux in kth step of MSR network	2,3
φ	[/]	Porosity (Volumetric)	2,5
ϑ^*	[/]	Power-law parameter connecting mass-dependent sulphur isotope fractionation for 33S and 34S	2
J_{SO4}	$M\ L^{-1}$	Sulfate flux accros the sediment water interface	5
K	Cells M^{-1}	Specific growth rates	3
υ	$L\ T^{-1}$	The velocity of flow relative to the sediments-water interface	2
Y	T^{-1}	Grow yield	3
$\Delta\ \delta^{13}C_{CH4}$	‰	Carbon isotopic shift in methane during Anerobic oxidation of methane	5
$\delta^{13}C_{CH4}$	‰	Carbon isotopic composition of methane	1,2,4,5
$\delta^{13}C_{DIC}$	‰	Carbon isotopic composition of dissolved inorganing carbon	1,2,4,5
$\delta^{18}O_{H2O}$	‰	Oxygen isotopic composition of water	2,3,4
$\delta^{18}O_{S4O}$	‰	Oxygen isotopic composition of sulfate	All
$\delta^{18}O_{SO4(A.E)}$	‰	Oxygen isotopic composition of sulfate at apparent equlibrium	2,3
$\delta 34S_{SO4}$	‰	Sulfur isotopic composition of sulfate	All
θ_O	[/]	Ratio between sulfite back reaction to the outer sulfate pool and the overall sulfate reduction rate	2,3
ω	$L\ T^{-1}$	Rate of burial of the layer below the sediments-water interface	2

2.1 The use of models of sulfur and oxygen isotope fractionation during microbial sulfate reduction

Numerical models of MSR use sulfur ($^{33}S/^{32}S$ and $^{34}S/^{32}S$) and oxygen ($^{18}O/^{16}O$) isotope ratios in dissolved sulfate as experimental constraints, add assumptions about cellular energetics, electron flow and maximum isotope fractionations imparted by some enzymes, and then solve for the magnitude of backward and forward fluxes associated with the modelled reactions. These models have been used to reconstruct environmental processes and physiological conditions from observed isotope fractionations (e.g. Canfield et al., 2001a; 2006; Farquhar et al., 2003; 2007; Johnston et al, 2007; Sim et al., 2011a;2011b; Leavitt et al., 2013; Wing and Halevy, 2014). The use of either multiple sulfur or sulfur and oxygen isotopes provides a set of two independent equations to solve, and therefore can resolve the relative fluxes at up to two branching points within the cell, but there are more than two reactions, or branching points, to account for (e.g. Figure 1.2 in Chapter 1, Figure 2.1 here). The problem is therefore under-constrained, as there are more variables than equations. Many studies work around this limitation by merging several steps together, most notably, considering the reduction of sulfite to sulfide as single step. However, Brunner et al. (2012) modelled the sulfur and oxygen isotope evolution during MSR, and in so determined that a single-step sulfite reduction to sulfide (step 4 and 5—Figure 2.1) is not consistent with the isotope data. In theory, combining multiple sulfur and oxygen isotopes would help constrain the problem, and provide an equivalent number of variables and equations, however, only a few studies have combined multiple sulfur and oxygen isotopes (^{32}S, ^{33}S, ^{34}S and ^{18}O and ^{16}O) (e.g. Farquhar et al., 2008). I will use this multiple isotope approach in Chapter 3 in pure culture studies. In this section, however, I will summarize past models efforts, including mine published in my MSc, for sulfur and oxygen isotopes during MSR.

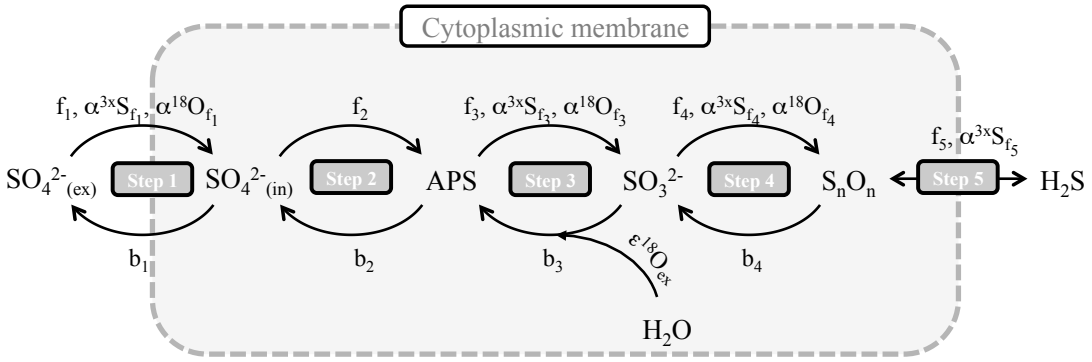

Figure 2.1: Schematic of the microbial sulfate reduction pathway. Note that this is similar to Figure 1.2 in Chapter 1 modified to assign fluxes to the various steps and isotope fractionation factors. Steps of microbial sulfate reduction and the presumed points of oxygen and sulfur isotope fractionation. i_{j_j}, $\alpha^{34}S_{i\_j}$ and $\alpha^{18}O_{i\_j}$ are the fluxes and the isotope fractionation factors for sulfur and oxygen, respectively, for the forward (i=f) and backward (i=b) reactions j (j=1...5). f_k (k=1,2 and 4) is the ratio between the backward and forward fluxes. $\varepsilon^{18}Oex$ is the oxygen isotopic fractionation between water and sulfur intermediates

The overall sulfur isotope fractionation during MSR is modelled as a superposition of the various forward and backward fluxes at each step with any isotope partitioning occurring at each step (Rees, 1973; Brunner and Bernasconi, 2005; Farquhar et al., 2003; Sim et al., 2011b) and is given mathematically by (after Brunner et al 2012):

$$\alpha^{3x}S_{total} = \frac{\begin{array}{c}\phi_1\cdot\phi_2\cdot\phi_3\cdot\phi_4\cdot\left(1-\alpha^{3x}S_{f\_5}\right)+\ldots \\ \phi_1\cdot\phi_2\cdot\phi_3\cdot\alpha^{3x}S_{f\_5}\cdot\left(1-\alpha^{3x}S_{f\_4}\right)+\ldots \\ \phi_1\cdot\phi_2\cdot\alpha^{3x}S_{f\_5}\cdot\alpha^{3x}S_{f\_4}\cdot\left(1-\alpha^{3x}S_{f\_3}\right)\end{array}}{\alpha^{3x}S_{f\_5}\cdot\alpha^{3x}S_{f\_4}\cdot\alpha^{3x}S_{f\_3}} + 1 \quad (2.1)$$

where $\alpha^{3x}S_{total}$ is the total expressed sulfur isotope fractionation factor for isotope 3x (x=3,4,6), $\alpha\ ^{3x}S_{i\_j}$ is the sulfur isotope fractionation during the forward (i=f) and backward (i=b) reaction j (where j=1…5) and ϕ_k (where k=1…4) is the ratio between the fluxes of the four intracellular steps summarized in Figure 2.1:

$$\phi_k = \frac{b_k}{f_k} \quad (2.2)$$

Thus, models of MSR (Rees, 1973; Brunner and Bernasconi, 2005; Farquhar et al., 2003; Sim et al., 2011b; Brunner et al., 2012) assign maximum values of sulfur isotope fractionation in the forward steps 1,3,4 and 5, respectively, and assume that all other steps do not fractionate sulfur isotopes – e.g., Rees, 1973).

For minor isotopes (such as ^{33}S), the relationship between the isotope fractionation for ^{33}S /^{32}S (compared with $^{34}S/^{32}S$) is commonly given as (e.g. Young et al., 2002; Farquhar et al., 2003; Johnston et al, 2005):

$$\ln(\alpha^{33}S) = \vartheta^* \cdot \ln(\alpha^{34}S) \quad (2.3)$$

where ϑ^* is the calculated temperature-dependent equilibrium isotope fractionation between sulfate and sulfide (0.5147-- Farquhar et al., 2003). The deviation between the calculated value for $\alpha^{33}S$ and the expected mass-dependent relationship between $\alpha^{33}S$ and $\alpha^{34}S$ is defined as:

$$E^{33}S = 1000 \cdot \left(\alpha^{33}S - \alpha^{34}S^{0.515}\right) \quad (2.4)$$

Whereas the isotope fractionation of ^{33}S in every step during MSR does not deviate from a mass dependent fractionation with respect to ^{34}S (Equation 2.1), the overall expressed isotope fractionation can deviate from a purely mass-dependent relationship. The magnitude of this offset is a function of the relative forward and backward fluxes of every step during MSR and stems from the fact that the mixing between two pools is linear, but the mass-dependent fractionation obeys a power law (Farquhar et al., 2003; Farquhar et al., 2007; Johnston et al, 2007). Mixing between two pools with variable branching points is common in metabolisms such as MSR, and it has been used in the past to calculate the dynamics of the forward and backward fluxes of each step during MSR as well as explore the evolution of microbial metabolism over the course of Earth history (e.g. Canfield, 2004; Farquhar

et al., 2003; 2013; Sim et al., 2011b; Johnston et al., 2005; 2006; 2011; Crowe et al., 2014; Paris et al., 2014). This is demonstrated in Figure 2.2a.

Oxygen isotopes in dissolved sulfate ($\delta^{18}O_{SO4}$) are thought to record information complementary to that revealed by sulfur isotopes. The relative change between $\delta^{18}O_{SO4}$ and $\delta^{34}S_{SO4}$ has been used as a tracer of pyrite oxidation (e.g. Balci et al., 2007; Brunner, et al., 2008; Heidel and Tichomirowa, 2011; Kohl and Bao, 2011), sulfur disproportionation (e.g. Cypionka et al., 1998; Böttcher et al, 2001; Böttcher and Thamdrup, 2001; Böttcher et al, 2005), cryptic cycling of sulfur (e.g. Aller et al, 2010; Johnston et al., 2014; Riedinger et al., 2010; Mikucki et al., 2009) and sulfate-driven anaerobic oxidation of methane (e.g. Aharon an Fu, 2000; 2003; Deusner et al., 2014; Sivan et al., 2014). Changes in the reversibility of all steps during MSR (Figure 2.1) leads to differing changes in the oxygen - and sulfur - isotope composition of sulfate as MSR progresses.

The model for oxygen isotopes in sulfate is derived from the work of Brunner et al. (2005, 2012). In order to understand the relative evolution of sulfur and oxygen isotopes in sulfate during bacterial sulfate reduction in pure culture, Brunner et al. (2005, 2012) solved a time dependent equation in which the oxygen isotope exchange between sulfur intermediates and ambient water and the cell specific sulfate reduction rates are the ultimate factors controlling the slope of $\delta^{18}O_{SO4}$ vs. $\delta^{34}S_{SO4}$ during the onset of bacterial sulfate reduction. For the purpose of this thesis (as applied to natural environments rather than pure cultures) I reconsidered this model in three ways. First, the cell specific sulfate reduction rate varies over orders of magnitudes in different natural environments, yet the relative evolution of $\delta^{18}O_{SO4}$ vs. $\delta^{34}S_{SO4}$ plot versus depth may exhibit the same pattern. Therefore, I suggest that any time dependent process related to the isotope evolution (e.g. the rate of the oxygen isotopic exchange between ambient water and sulfur intermediate such as sulfite) is faster than the other biochemical steps during bacterial sulfate reduction. Second, in the models of Brunner et al. (2005, 2012) the equilibrium value for the $\delta^{18}O_{SO4}$ depended critically on the value of $\delta^{18}O$ of the ambient water. However, the equilibrium value for $\delta^{18}O_{SO4}$ in natural environments shows a range (22-30‰) that cannot be explained only by the variation in $\delta^{18}O$ of the ambient water (which ranges from 0 to -4‰). It

has been suggested that this large range of oxygen isotope equilibrium values may reflect isotope exchange at different temperatures, although more recent studies have shown that the temperature effect is small (~2‰ between 23 to 4°C -- Brunner et al., 2006; Zeebe, 2010). Alternatively the large range of oxygen isotope equilibrium may reflect the combined effect of kinetic and equilibrium oxygen isotope fractionation (Wortmann et al., 2007; Turchyn et al., 2010). The latter has led to the observed $\delta^{18}O_{SO4}$ at equilibrium to be termed 'apparent equilibrium' ($\delta^{18}O_{SO4(A.E)}$). For my model, therefore, I attributed the change in the $\delta^{18}O_{SO4}$ to change in the mechanism of the bacterial sulfate reduction and not to changes in the $\delta^{18}O$ of the water. Third, the model of Brunner el al. (2005, 2012) ruled out a linear relationship between $\delta^{18}O_{SO4}$ and $\delta^{34}S_{SO4}$ which has not been observed in pure culture. My model had to account for a linear relationship, which has been observed in natural environments.

To address these issues, I removed the characteristic timescale used by Brunner et al. (2005, 2012) for the cell-specific sulfate reduction rate and focus instead on how the different fluxes at each step impact the evolution of $\delta^{18}O_{SO4}$ vs. $\delta^{34}S_{SO4}$. I further allowed changes in the equilibrium values of the $\delta^{18}O_{SO4}$ due to a combination of equilibrium and kinetic oxygen isotope effects rather than only through a change in the $\delta^{18}O$ of the ambient water.

The assumptions in my model include:

- The system is in steady state. This means sulfate reduction rate = $f_i - b_i$ (where i=1,2,3— Figure 2.1).
- I model oxygen isotopic exchange between ambient water and sulfite (Betts and Voss, 1970; Horner and Connick, 2003; Müller et al., 2013; Wankel et al., 2014). This oxygen isotope exchange contributes three oxygen atoms to the sulfate that will ultimately be produced during reoxidation, while the fourth oxygen atom is gained during the reoxidation of the AMP-sulfite complex to sulfate (Wortmann et al., 2007; Brunner et al., 2012).
- Oxygen isotopic exchange is considered to be much faster with respect to other biochemical steps, which means, that for any practical purpose, sulfite is constantly in oxygen isotopic equilibrium with ambient water. This results in a solution that is independent of the timescale of the problem. This is because the

timescale for this isotope exchange, given intracellular pH (6.5-7 — Booth, 1985), should shorter than minutes (Betts and Voss, 1970; Wankel et al., 2014).

• The kinetic oxygen isotopic fractionation during the reduction of APS to sulfite (f_3) is equal to 25% of the sulfur isotope fractionation ($\varepsilon^{18}O_{f\_3}$: $\varepsilon^{34}S_{f\_3}$=1:4) (Mizutani and Rafter, 1969)**.** This value for the kinetic oxygen isotope fractionation is the lowest value that was found in lab experiments, and therefore I consider it to be the closest to the real ratio between $\varepsilon^{18}O_{f\_3}$ and $\varepsilon^{34}S_{f\_3}$. This assumption has not been made by Brunner et al. (2005, 2012) and allows my model to simulate a linear relationship between $\delta^{18}O_{SO4}$ and $\delta^{34}S_{SO4}$.

• Any kinetic oxygen isotope fractionation in step 4 or step 5 (the reduction of sulfite to sulfide) is not significant for oxygen isotopes, since oxygen isotope exchange during the back reaction (step 3) resets the $\delta^{18}O$ of the sulfite.

• Step 5 was simplified by making it unidirectional. I am able to do this because recent work has suggested that even if sulfide concentrations are high (>20 mM), only ~10% of the sulfide is re-oxidized (Eckert et al., 2011) which is insignificant with respect to the overall recycling of other sulfur intermediates (Wortmann et al., 2007; Turchyn et al., 2006).

The full derivation of the model equations using these assumptions, and similar to the derivation in Brunner et al., 2012, is in Appendix A and yields the following continuous (See appendix B for function analyse) solution for $\delta^{18}O_{SO4(t)}$ as function of $\delta^{34}S_{SO4(t)}$:

$$\begin{gathered}\text{If } \phi_1\cdot\phi_2\cdot\phi_3=0 \text{ then}\\ \delta^{18}O_{SO4(t)}=\frac{\varepsilon^{18}O_{total}}{\varepsilon^{34}S_{total}}\cdot\left(\delta^{34}S_{SO4(t)}-\delta^{34}S_{SO4(0)}\right)+\delta^{18}O_{SO4(0)}\\ \text{and if } 0<\phi_1\cdot\phi_2\cdot\phi_3<1 \text{ then}\\ \delta^{18}O_{SO4(t)}=\delta^{18}O_{SO4(A.E)}-\exp\left(-\theta_O\cdot\frac{\delta^{34}S_{SO4(t)}-\delta^{34}S_{SO4(0)}}{\varepsilon^{34}S_{Stotal}}\right)\cdot\left(\delta^{18}O_{SO4(A.E)}-\delta^{18}O_{SO4(0)}\right)\end{gathered} \tag{2.5}$$

where $\varepsilon^{34}S_{total}$ and $\varepsilon^{18}O_{total}$ are the measured sulfur and oxygen isotope fractionations, respectively, and $\delta^{34}S_{SO4(t)}$, $\delta^{34}S_{SO4(0)}$, $\delta^{18}O_{SO4(t)}$ and $\delta^{18}O_{SO4(0)}$ are the isotopic

compositions of sulfur and oxygen in the residual sulfate at time t and time 0, respectively. $\delta^{18}O_{SO4(A.E)}$ is the isotopic composition of oxygen in the residual sulfate at 'apparent equilibrium', and θ_O is a parameter initially formulated by Brunner et al. (2005). This parameter define as the ratio between sulfite back reaction to the outer sulfate pool and the overall sulfate reduction rate (Brunner et al., 2012):

$$\theta_O = \frac{\phi_1 \cdot \phi_2 \cdot \phi_3}{1-\phi_1 \cdot \phi_2 \cdot \phi_3} \quad (2.6)$$

Factorization of equation (2.5) suggests that there are two distinct stages on a cross-plot of $\delta^{18}O_{SO4}$ vs. $\delta^{34}S_{SO4}$ during microbial sulfate reduction:

1. Apparent linear phase. The initial stage of the $\delta^{18}O_{SO4}$ vs. $\delta^{34}S_{SO4}$ cross-plot during MSR can be approximated by a linear line. The mathematical term for this line can be described by the first term of an Equation 8 Taylor series around $\delta^{34}S_{SO4(0)}$ and $\delta^{18}O_{SO4(0)}$ (Antler et al., 2013). The slope of this apparent linear phase (SALP) can therefore be written as:

$$SALP = \theta_O \frac{\delta^{18}O_{SO4(A.E)} - \delta^{18}O_{SO4(0)}}{\varepsilon^{34}S_{total}} \quad (2.7)$$

The value of the SALP can vary between 0.25 to over 10 and has been shown to be a function of the sulfate reduction rate (Böttcher et al., 1998; 1999; Brunner et al., 2006; Aharon and Fu, 2000; Antler et al., 2013) and the electron donor type and supply rate of this electron donor (Sim et al., 2011b)

2. Apparent equilibrium phase. This is the last stage on the $\delta^{18}O_{SO4}$ vs. $\delta^{34}S_{SO4}$ cross plot, where the $\delta^{18}O_{SO4}$ reaches a constant value while the $\delta^{34}S_{SO4}$ continues to increase. In the natural environment, the $\delta^{18}O_{SO4}$ equilibrium can vary between 22‰ and 30‰ over the $\delta^{18}O$ of the water (e.g. Wortmann et al., 2007; Turchyn et al., 2006; Knöller et al., 2006). Several sulfur intermediates have been suggested to exchange oxygen isotopes with water; most notably APS (e.g. Mizutani and Rafter, 1973; Fritz, et al., 1989), sulfite (e.g. Wankel et al., 2014; Muller et al., 2013) and AMP (e.g.

Wortmann et al., 2007; Wankel et al., 2014). Recent studies have ruled out the equilibrium between APS and water (Brunner et al., 2012; Kohl et al., 2012). Under cytoplasmic pH (6-7), sulfite reaches isotopic equilibration in matters of minutes (Betts and Voss, 1970); the rapidity of the oxygen isotope equilibrium implies that sulfite in the cell is in fully equilibration with water. The value of apparent equilibrium, including the effect of the kinetic oxygen isotope fractionation, is expressed mathematically as:

$$\delta^{18}O_{SO4(A.E)}=\delta^{18}O_{H2O}+\varepsilon^{18}O_{ex}+\frac{\varepsilon^{18}O_{f\_1}}{\phi_1\cdot\phi_3}+\frac{\varepsilon^{18}O_{f\_3}}{\phi_3} \quad (2.8)$$

Since $\delta^{18}O_{SO4}$ does not always reach apparent equilibrium within the frame of given experiment or even at times in the natural environment, the apparent equilibrium value ($\delta^{18}O_{SO4(A.E)}$) can be obtained from the fact that SALP and $\delta^{18}O_{SO4(A.E)}$ should correlate (Equation 2.7); this correlation implies that you can calculate $\delta^{18}O_{SO4(A.E)}$ from a cross plot of SALP vs. $\delta^{18}O_{H2O}$. At the intercept of a SALP vs. $\delta^{18}O_{H2O}$ line ($\delta^{18}O_{H2O}=0$), the $\delta^{18}O_{SO4(A.E)}$ is equal to:

$$\delta^{18}O_{SO4(A.E)}=SALP_{(\delta^{18}O_{H2O}=0)}\cdot\frac{\varepsilon^{34}S_{total}}{\theta_O}+\delta^{18}O_{SO4(t=0)} \quad (2.9)$$

where $SALP_{(\delta^{18}O_{H2O}=0)}$ is the slope of the apparent linear phase predicted at $\delta^{18}O_{H2O}=0$ (and the intercept on the SALP vs. $\delta^{18}O_{H2O}$ plot) and $\delta^{18}O_{SO4(t=0)}$ is the initial $\delta^{18}O_{SO4}$ value (at time zero).

Similarly, a useful way to study the mutual evolution of $\delta^{18}O_{SO4}$ and $\delta^{34}S_{SO4}$ with respect to reaction progress (e.g. the decrease in sulfate concentration with time during MSR) is to plot θ_O vs. $\varepsilon^{34}S_{total}$ (Figure 2.2b). Previous studies have used this cross-plot to investigate the mechanism of MSR (Brunner, et al., 2005; Knöller et al., 2006; Turchyn, et al., 2010; Brunner et al., 2012; Antler et al., 2013) and sulfate-driven anaerobic methane oxidation (Deusner et al., 2014). Because both $\varepsilon^{34}S_{total}$ and θ_O are functions of the forward and backward fluxes during MSR (Equations 6 and 9, respectively), this plot can be used to relate sulfur and oxygen isotope measurements

to the intracellular MSR fluxes. This is because for every set of given forward and backward fluxes there is specific θ_O and $\varepsilon^{34}S_{total}$. However, since there are more branching points in the framework of MSR than the solution for θ_O and $\varepsilon^{34}S_{total}$, the ratio of between the forward and backward fluxes of every branching point cannot be solved uniquely. Figure 2.2b also demonstrates the relationship between θ_O vs. $\varepsilon^{34}S_{total}$ and the ratio of intracellular fluxes.

Calculations of θ_O must assume a certain value of $\delta^{18}O_{SO4(A.E)}$ (e.g. Brunner et al., 2006; Knöller et al., 2006— see also equation 2.5). However, if $\delta^{18}O_{SO4}$ did not reach equilibrium there might be a big uncertainty in estimating this $\delta^{18}O_{SO4(A.E)}$. We can think about alternative ways to estimate θ_O without the needs of a measured $\delta^{18}O_{SO4(A.E)}$; here, I resolve this by noting that $\delta^{18}O_{SO4(A.E)}$ is proportional to the $\delta^{18}O_{H2O}$ (Eq. 2.8), and their differentials are equal: $d(\delta^{18}O_{SO4(A.E)})=d(\delta^{18}O_{H2O})$, therefore they are directly proportional. In addition, the slope of the apparent linear phase (SALP) is proportional to $\delta^{18}O_{SO4(A.E)}$ (Eq. 2.9). Hence, SALP is also proportional to $\delta^{18}O_{H2O}$:

$$SALP \propto \delta^{18}O_{H2O} \quad (2.10)$$

According to equation 2.7, the proportionality coefficient should be equal to $\theta_O/\varepsilon^{34}S_{total}$ and is equal to the slope of the SALP vs. $\delta^{18}O_{H2O}$. Then, $\varepsilon^{34}S_{total}$ is easily calculated from experimental measurements, and θ_O can be derived.

The θ_O vs. $\varepsilon^{34}S_{total}$ diagram (Figure 2.2b) has similarities with the $E^{33}S$ vs. $\varepsilon^{34}S_{total}$ diagram (Fig, 2.2a), but typically one of the two of them is used alone. Chapter 3 will explore whether the use of combined θ_O vs. $\varepsilon^{34}S_{total}$ and $E^{33}S$ vs. $\varepsilon^{34}S_{total}$ diagrams can enable the probing of different processes and reaction rates during MSR. In theory, this combined isotope approach explores a wider range of steps in the MSR network, not all of which can be inferred by using θ_O vs. $\varepsilon^{34}S_{total}$ or $E^{33}S$ vs. $\varepsilon^{34}S_{total}$ plots alone.

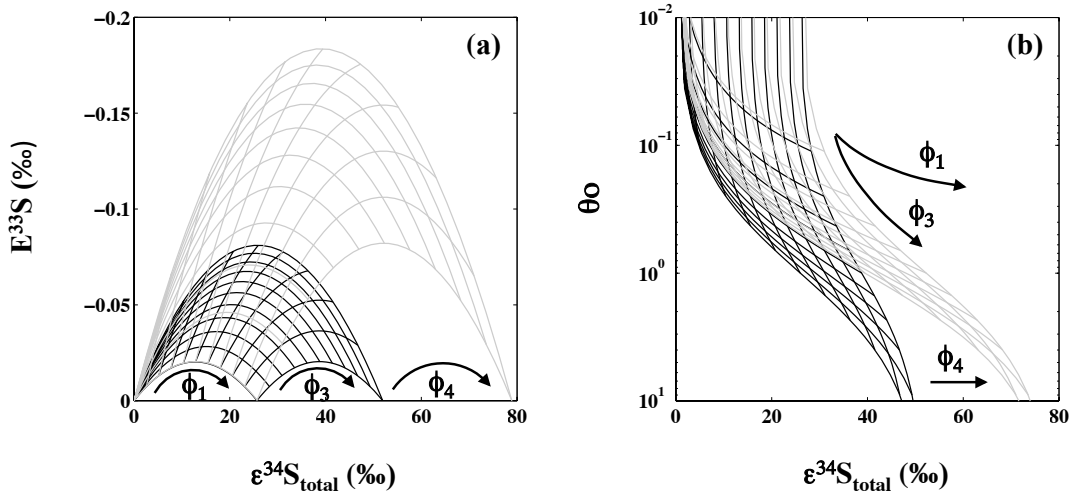

Figure 2.2: $E^{33}S$ vs. $\varepsilon^{34}S_{total}$ (a) and θ_O vs. $\varepsilon^{34}S_{total}$ (b) diagrams. The black and the gray meshes are the solutions where ϕ_4 (the fluxes ratio of step 4, the reduction of sulfite to S_nO_n—figure 1) is minimal (=0) and maximal (=1), respectively. The arrows represent the direction n by which each flux ratio (Figure 1) changes in the diagrams. In theory, an experiment where two of three of $E^{33}S$, $\varepsilon^{34}S_{total}$, and θ_O are measured will plot within the black and the grey meshes and it will allow solution for the relative fluxes at the various steps during MSR. Here, I use the isotope fractionation for steps 3,4 and 5 as $\alpha^{3x}S$= 0.975 (Brunner et al., 2012) and θ=0.5147 (Farquhar et al., 2003).*

2.2 Applying my time-dependent closed system model to pore fluid profiles

In this section I discuss the use of my model of microbial sulfate reduction metabolism (Section 2.1) to understand what controls the relative evolution of $\delta^{18}O_{SO4}$ vs. $\delta^{34}S_{SO4}$ in the natural environment. Applying what is effectively a "closed system" model to an "open system" (environmental pore fluids) requires understanding the physical parameters that control each of the sulfate species concentrations (in this case $^{34}S^{16}O_4^{2-}$, $^{32}S\ ^{18}O^{16}O_3^{2-}$ and $^{32}S^{16}O_4^{2-}$) within the fluids in

the sediment column (Jørgensen, 1979; Wortmann et al., 2007; Wortmann and Chernyavsky, 2011).

In my thesis I utilize SALP, that is the relative change of $\delta^{18}O_{SO4}$ vs. $\delta^{34}S_{SO4}$, rather than the $\delta^{18}O_{SO4}$ value at apparent equilibrium although both hold information about the mechanism of the microbial sulfate reduction (see Equation 2.7 and 2.8). Focusing on SALP enables investigating the mechanism of microbial sulfate reduction from sites that were not cored deep enough to observe apparent equilibrium. Also, it is not clear whether the $\delta^{18}O_{SO4}$ really reaches equilibrium values at some sites.

The outstanding question is how can I apply SALP as observed in the relative evolution of the $\delta^{18}O_{SO4}$ and $\delta^{34}S_{SO4}$ in the pore fluids to the model for the biochemical steps during bacterial sulfate reduction as derived for pure cultures? In order to investigate to what extent the closed system model can be apply to an open system, I generated sulfate, $\delta^{18}O_{SO4}$ and $\delta^{34}S_{SO4}$ synthetic profiles for two extreme cases, deep-sea and estuarine sediments. The profiles were generated using the general diagenetic equation (Berner, 1980):

$$\frac{\partial \varphi C_i}{\partial t} = \varphi \frac{\partial}{\partial z}\left(D_z \frac{\partial C_i}{\partial z}\right) - (U+\omega)\frac{\partial C_i}{\partial z} - \sum R_i \quad (2.11)$$

where C_i is the concentration of solid or liquid component i in mass per unit volume of total sediment, t is time, z is the layer depth, φ is the porosity Ds is the effective diffusion coefficient in area of total sediments per unit time, U is the velocity of flow relative to the sediments-water interface, ω is the rate of burial of the layer below the sediments-water interface and R is the reactions affecting i.

C_i stands for each one of the different sulfate species (in this case $^{32}S^{16}O_4^{2-}$, $^{34}S^{16}O_4^{2-}$, $S^{18}O\ ^{16}O_3^{2-}$ as all other species considered as much less abundant). For my purpose, I assume no advection and uniform porosity throughout the sediment column and with time. In addition, sulfate reduction rates were considered as constant in space and time (the reduction rate of each sulfate species was calculated using the

overall sulfate reduction rate and the expected change in $\delta^{18}O_{SO4}$ and $\delta^{34}S_{SO4}$ according to the close system model— see above). Therefore equation 2.11 can be written as:

$$\frac{\partial C_i}{\partial t} = D_s \frac{\partial^2 C_i}{\partial z^2} - \omega \frac{\partial C_i}{\partial z} - SRR_{(Ci)} \quad (2.12)$$

I solved equation 2.12 using a finite difference approach. The sulfate species concentrations began at seawater concentrations throughout the entire sediment column, except at the deepest point in each case where the concentrations were considered as zero. I let all the profiles reach to steady state (steady state defined when the maximum different between the concentrations two time intervals at given depth is smaller than 10 orders of magnitudes than the concentration at this depth). The assumption that $Ds=D_0 \cdot \varphi^2$ (Berner et al., 1980) was used for estimating the effect of tortuosity. φ is the porosity and the molecular diffusion coefficient for sulfate in seawater (D_0) was calculated based on Donahue et al. (2008):

$$D_0=(4.655+0.2125 \cdot T) \cdot 10^{-6} \quad (2.13)$$

where D_0 is the molecular diffusion coefficient of sulfate (cm^2 sec^{-1}) and T is the temperature (ºK).

Two extreme cases were considered: (a) Deep-sea temperature (2°C), low sedimentation rate (10^{-3} cm·$year^{-1}$) and slow net sulfate reduction rate (low as 10^{-12} mol·cm^{-3}·$year^{-1}$), typical of deep-sea environments versus (b) Surface temperature (25°C), high sedimentation rate (10^{-1} cm·$year^{-1}$) and high net sulfate reduction rate ($5 \cdot 10^{-4}$ mol·cm^{-3}·$year^{-1}$) conditions similar to shallow marginal-marine environments. In each case I have calculated the “closed system” solution for a given mechanism, or intracellular fluxes during microbial sulfate reduction, and then separately calculated the “open system” for the same mechanism give the natural conditions described above.

Figure 2.3 presents the calculated open system versus closed system SALP for the two extreme environments, as function of the change in ϕ_3 (where ϕ_1 and ϕ_4 are fixed and equal to 0.99 and 0, respectively). It can be seen that in applying the closed system solution to the open system can lead to underestimation of as much as 10% in the value of ϕ_3 (For changes in ϕ_1 and ϕ_4, the misestimate will be similar in magnitude). Although there are vastly different physical parameters between these two synthetic sites, the resulting calculated SALPs are not significantly different. This similarity in calculated SALP is because the main difference moving to an open system from a closed system is the change the relative diffusion flux of any of the isotopologues. I conclude that it is possible to read the SALP from $\delta^{18}O_{SO4}$ and $\delta^{34}S_{SO4}$ pore fluid profiles and apply my closed system model to understand the mechanism, with the caveat that I have error bars on my resulting interpretation.

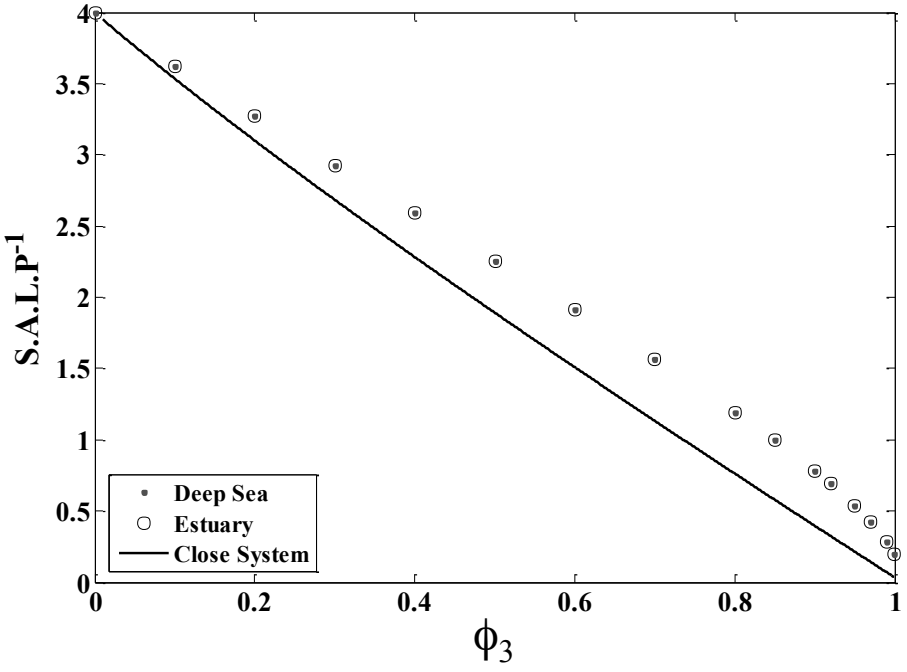

Figure 2.3: The slope of the apparent linear phase as a function of ϕ_3 (where ϕ_1 and ϕ_4 are fixed and equal to 0.99 and 0, respectively) for 3 different scenarios: Closed system (according to Equation 2.7), simulation of typical deep-sea sediment and simulation of typical estuary sediment.

2.3 Analytical methods

Table 2.1 summarizes the measurements that have been made in each of the chapters in this thesis. Cation (Na^+, K^+, Ca^{2+}, Mg^{2+}, Sr^{2+}) concentrations were analysed by Inductivity Coupled Plasma-Atomic Emission spectroscopy (ICP-AES, P-E optima 3300, at the Geological Survey of Israel) with error of 2%. Sulfate concentrations were measured by Ion Chromatography (IC, Dionex DX5000, at Ben Gurion University of the Negev) with an error of 3%. Sulfide concentrations were measured by spectrophotometer using modified methylene blue assay (Cline, 1969). DIC concentrations were measured according to the peak height and calibration curve on the Continues Flow Gas Source Isotopic Ratio Mass Spectrometer (CF-GS-IRMS Thermo, at Ben Gurion University of the Negev) with an error of 0.2 mM. For methane measurement, 1 ml headspace sample was taken from the crimped vial with a gas-tight pressure lock after the bottle was shaken vigorously. Methane was measured from the headspace on a Focus Gas Chromatograph (Thermo, at Ben Gurion University of the Negev) with ShinCarbon column with precision of 2 $\mu M\ L^{-1}$. Cell density was measured by epifluorescence microscopic counts of cells stained by SYTOX-Green nucleic acid stain.

2.3.1 Isotope measurements

Sulfur isotopes

For $\delta^{34}S_{SO4}$ analysis, sulfate was precipitated as barium sulfate (barite) using a saturated barium chloride solution. The barite was then washed with 6N HCl and distilled water. The barite was combusted at 1030°C in a Flash Element Analyzer (EA), and the resulting sulfur dioxide (SO_2) was measured by continuous flow on a GS-IRMS (Thermo Finnegan Delta V Plus Godwin Laboratory, University of Cambridge). The error for $\delta^{34}S_{SO4}$ was determined using the standard deviation of the standard NBS 127 at the beginning and the end of each run (~0.3‰ 1σ). Samples were corrected to NBS 127, IAEA-SO-5 and IAEA-SO-6 standards (20.3‰, 0.5‰

and -34.1‰, respectively). The $\delta^{34}S_{SO4}$ values are reported versus Vienna Canyon Diablo Troilite (VCDT).

For multiple sulfur isotope measurements ($\delta^{33}S$ and $\delta^{34}S$), sulfide generated during batch culture growth was extracted by acidifying the culture medium with 6 N HCl at 80°C under nitrogen gas for two hours. $H_2S(g)$ produced during this distillation was precipitated as ZnS in a Zn–acetate solution (0.18 M). After the extraction of sulfide, the samples were purged by nitrogen gas for an additional hour to ensure the complete removal of sulfide. Sulfate in the remaining medium was reduced to sulfide by reacting with 30 ml of the reducing agent (mixture of HI, H_3PO_2 and HCl, Thode et al., 1961). The samples were boiled and purged by N_2 gas. After the volatile products were passed through a condenser and a trap containing distilled water, sulfide gas generated from sulfate reduction was collected in the $AgNO_3$ trap. Ag_2S samples were then reacted with an excess of fluorine gas at 300 °C. The produced SF_6 gas was purified by gas chromatography and transferred into an isotope-ratio mass spectrometer for multiple sulfur isotope measurements in dual-inlet mode (Stable Isotope Geobiology Laboratory at Massachusetts Institute of Technology). The analytical reproducibility of measurements using the fluorination method, as determined by repeated analyses of international reference material, is ±0.1‰ and ±0.2‰ and ±0.01‰ for $\delta^{33}S$, $\delta^{34}S$ and $\delta^{33}S$-0.515•$\delta^{34}S$, respectively.

Oxygen isotopes

$\delta^{18}O_{H2O}$ was measured by a Continues Flow Gas Source Isotopic Ratio Mass Spectrometer (CF-GS-IRMS Thermo, at Ben Gurion University of the Negev) coupled to a Gas Bench II (GBII) interface. Vials containing 0.5 ml of the sample were flushed with helium and 0.4% CO2 gas-mixture and the samples were measured after equilibrating for 24 hours. Samples were corrected to three standards (-7.3, 0.2 and 11.2‰). The error of the measurement was ± 0.1‰. $\delta^{18}O_{H2O}$ reported versus Vienna Standard mean Ocean water (VSMOW).

For $\delta^{18}O_{SO4}$ analysis, barite was pyrolyzed at 1450°C in a Temperature Conversion Element Analyzer (TC/EA). The resulting carbon monoxide (CO) was

measured by continuous helium flow on a GS-IRMS (Thermo Finnegan Delta V advance, at the Godwin Laboratory, University of Cambridge). Samples for $\delta^{18}O_{SO4}$ ran in replicates (n=3-5) and the standard deviation of these replicate analyses was used as the error (~0.3‰ 1σ). Samples for both $\delta^{18}O_{SO4}$ and $\delta^{34}S_{SO4}$ were corrected to NBS 127 and IAEA-SO-6 standards (8.6‰ and -11.35‰). $\delta^{18}O_{SO4}$ reported versus Vienna Standard Mean Ocean water (VSMOW).

$\delta^{18}O$ Measurement validation

The pure culture growth experiments (Chapter 3) were done with enriched ^{18}O water (with $\delta^{18}O_{H2O}$ up to ~78‰), which introduces several analytical issues. First, it is not clear how linear the mass spectrometers are for high values of $\delta^{18}O_{H2O}$ and $\delta^{18}O_{SO4}$. A non-linear response will result in error in the analysis since our isotope measurements are often exceeding the calibration envelope. I resolved this by diluting the high samples with a standard with low oxygen isotopic composition (-7.3‰ and -11.35‰ for $\delta^{18}O_{H2O}$ and $\delta^{18}O_{SO4}$, respectively). An example is shown in Figure 2.4 Both $\delta^{18}O_{H2O}$ and $\delta^{18}O_{SO4}$, are shown with the mixing line between the high δ18O sample and the low $\delta^{18}O$ standard. This exercise demonstrates that there is no significant effect on the $\delta^{18}O_{H2O}$ and $\delta^{18}O_{SO4}$ measurements as far from the calibration envelope as my experiments were done.

The second potential problem with using high $\delta^{18}O_{H2O}$ is the incorporation of water molecules into the barite crystal lattice. In order to examine the effect of the ^{18}O-enriched water on the measurement, I compare the initial $\delta^{18}O_{SO4}$ from all our experiment versus the $\delta^{18}O_{H2O}$ of the solution (Figure. 2.5). From this I show that the highest $\delta^{18}O_{SO4}$ I measure are, ironically, in the lowest $\delta^{18}O_{H2O}$, in addition there is no significant difference between $\delta^{18}O_{SO4}$ that was measured with water that had a $\delta^{18}O_{H2O}$ of ~75‰ or ~35‰ (Figure 2.5). This suggests that, for this experimental setup, there is virtually no effect of the oxygen isotopic composition of water on the oxygen isotopic composition of the sulfate during laboratory handling. I suggest that the high $\delta^{18}O_{SO4}$ value in the experiment with low $\delta^{18}O_{H2O}$ is most likely due to different batches of Na_2SO_4 salt that were used, which is also supported by different initial $\delta^{34}S_{SO4}$ which is ~1‰ in the experiments with higher the $\delta^{18}O_{SO4}$.

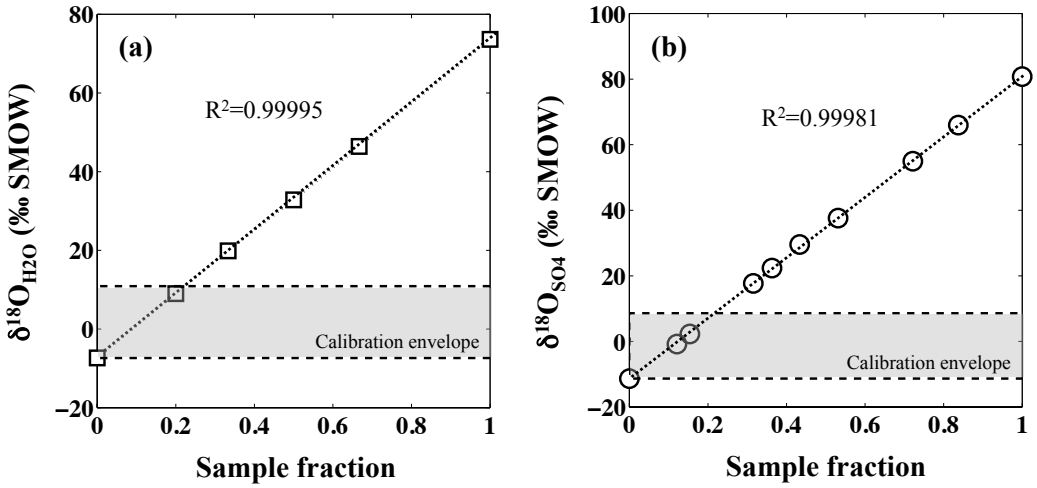

Figure 2.4: The measured $\delta^{18}O_{H2O}$ (a) and $\delta^{18}O_{SO4}$ (b) plotted versus sample dilution with a low value standard. The samples fraction is the fraction of the samples in the final mixture between the sample and the low standard.

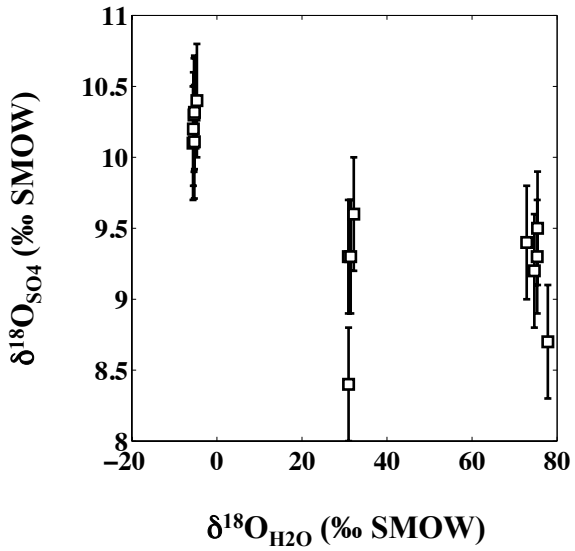

Figure 2.5: The initial $\delta^{18}O_{SO4}$ of each experiment versus the ambient $\delta^{18}O_{H2O}$.

Carbon isotopes

$\delta^{13}C_{DIC}$ and $\delta^{13}C_{CH4}$ were measured by a Continues Flow Gas Source Isotopic Ratio Mass Spectrometer (CF-GS-IRMS Thermo, at Ben Gurion University of the Negev) through a Gas Bench II (GBII) interface and the PreCon (for $\delta^{13}C_{CH4}$). The errors were 0.1‰ for $\delta^{13}C_{DIC}$ and 1‰ for $\delta^{13}C_{CH4}$ between replicates. The values are reported versus Vienna Pee Dee Belemnite (VPDB) standard.

Table 2.2: Summary of the measurements that have been done in each one of the thesis chapters

	Measurement									
	Major Cation	SO_4	H_2S	Cells count	DIC	CH_4	$\delta^{34}S$	$\delta^{33}S$	$\delta^{18}O^a$	$\delta^{13}C^b$
Chapter 3										
Chapter 4										
Chapter 5										

[a] $\delta^{18}O_{SO4}$ and $\delta^{18}O_{H2O}$

[b] $\delta^{13}C_{DIC}$ and $\delta^{13}C_{CH4}$

Chapter 3

Combined ^{33}S and ^{18}O isotope tracing of intracellular sulfur metabolism during microbial sulfate reduction

Given that each of the steps during MSR is reversible, understanding the relative forward and backward fluxes at each step within the cell and how these step-specific fluxes relate to the overall rate of sulfate reduction is critical for understanding how MSR impacts the subsurface carbon cycle. Changes in environmental conditions also should impact the fluxes at each step as well as the overall rate of MSR, but a quantitative understanding of the complete impact of these factors on the overall rate of MSR remains elusive.

Both oxygen and sulfur isotopes in the residual sulfate during sulfate reduction are affected by the changes in the intracellular fluxes of sulfur species within the bacterial cells. However, as I have outlined both in the introduction and the previous chapter, these isotopes in the residual sulfate are affected in different ways, and thus the change of one isotope versus the other helps solve for the relative change in the flux of each intracellular step as sulfate is being reduced (Farquhar et al., 2003; Rees 1973). The sulfur and oxygen isotope composition of residual sulfate has been used to explore the mechanism of traditional (organoclastic) sulfate reduction both in pure culture (e.g. Knöller et al., 2006; Mangalo et al., 2007; 2008; Brunner et al., 2005; 2012) and in the natural environment (e.g. Böttcher et al., 1998, 1999; Wortmann 2007, Turchyn 2006; Aller et al., 2010).

Pure culture experiments (i.e. experiment with single strain of an isolated microbe) are informative in studying microbial metabolism as pure cultures allow us

to study a single metabolism over a potential range of conditions. There are two main methods through which pure culture experiments are conducted; close system batch reactors experiment and open system chemostats (also known as flow-through reactors). While batch culture allow us to ascertain changes with time over the growth of the pure culture, a chemostat allows the culture to reach to steady state conditions. Both approaches have been used to explore MSR metabolism (e.g. Farquhar et al., 2003; Canfield et al., 2006; Sim et al., 2011b; Eckert et al., 2011). However, the "Achilles heel" of pure culture experiment is the lack of an environmental context; over 90% of the microbes present in marine sediments and soil samples are with an unknown metabolism. Therefore, studying only single bacteria give only partially constrains on environment and it is heavily biased toward microbes that are easier to isolate.

In this chapter I aim to: 1. Test whether the major and minor sulfur isotopes and the oxygen isotope systems record complementary or identical information about intracellular processes; and 2. explore the magnitude of the equilibrium and kinetic oxygen isotope effects. To do this, I experimentally explore the respective evolution of three isotope ratios: $^{33}S/^{32}S$, $^{34}S/^{32}S$ and $^{18}O/^{16}O$ during MSR in pure culture as a function of the csSRR and $\delta^{18}O_{H2O}$. These measurements are then used to constrain models of $\delta^{34}S_{SO4}$, $\delta^{33}S_{SO4}$ and $\delta^{18}O_{SO4}$. I will conclude this chapter by comparing my pure culture results with results from pore fluids from marine and marginal marine environments.

3.1 Methods

Pure culture marine *Desulfovibrio* sp. (Strain DMSS- 1—Sim et al. 2011) was incubated at room temperature (22ºC) in the dark to medium consisting of (per liter): $NaHCO^3$, 9 g; Na^2SO^4, 3 g; KH^2PO^4, 0.2 g; NH_4Cl, 0.3 g; NaCl, 21 g; $MgCl_2 \cdot 6H_2O$, 3 g; KCl, 0.5 g; $CaCl_2 \cdot 2H_2O$, 0.15 g; resazurin, 1 mg, as well as 1 ml of trace element solution SL-10 (Widdel et al., 1983), 10 ml of vitamin solution described as a part of DSMZ medium 141 (DSMZ, Braunschweig, Germany: Catalogue of strains 1993), and 1 ml of selenium stock solution (0.4 mg of Na_2SeO_3 per 200 ml of 0.01 N NaOH). Sodium ascorbate (1.5 g per liter) was added as a reducing agent. Lactate/

Malate/ Ethanol/ Fructose/ Glucose were used both as an electron donor and as a carbon source. The medium was titrated to pH 7.5 and prepared anaerobically under N2/CO2 (80%/20%). Each incubation experiment with different organic substrates was repeated three times using isotopically labelled water with different initial oxygen isotope compositions.

Bacteria were pre-cultured with the respective electron donor before inoculation (step a and b—Figure 3.1): about 1ml of pre culture medium was transfer to a 100ml of fresh medium after washing the plaque (step c—Figure 3.1). Then, 10ml of inoculated medium was transfer to 7 15ml vial (step e—Figure 3.1) which each provided a single-point batch experiment. Each vial was eliminated each time point, by removing 1ml of sample for cell counts and sulfide measurement and the injection of 2ml of 20% ZnAc. About 1ml were then filtered for sulfate concentration and another filtered 1ml was added to 1ml saturated BaCl solution to precipitated $BaSO_4$. The remaining solution was used to analyse multiple sulfur isotopes. The specific analytical methods were detailed in Chapter 2.

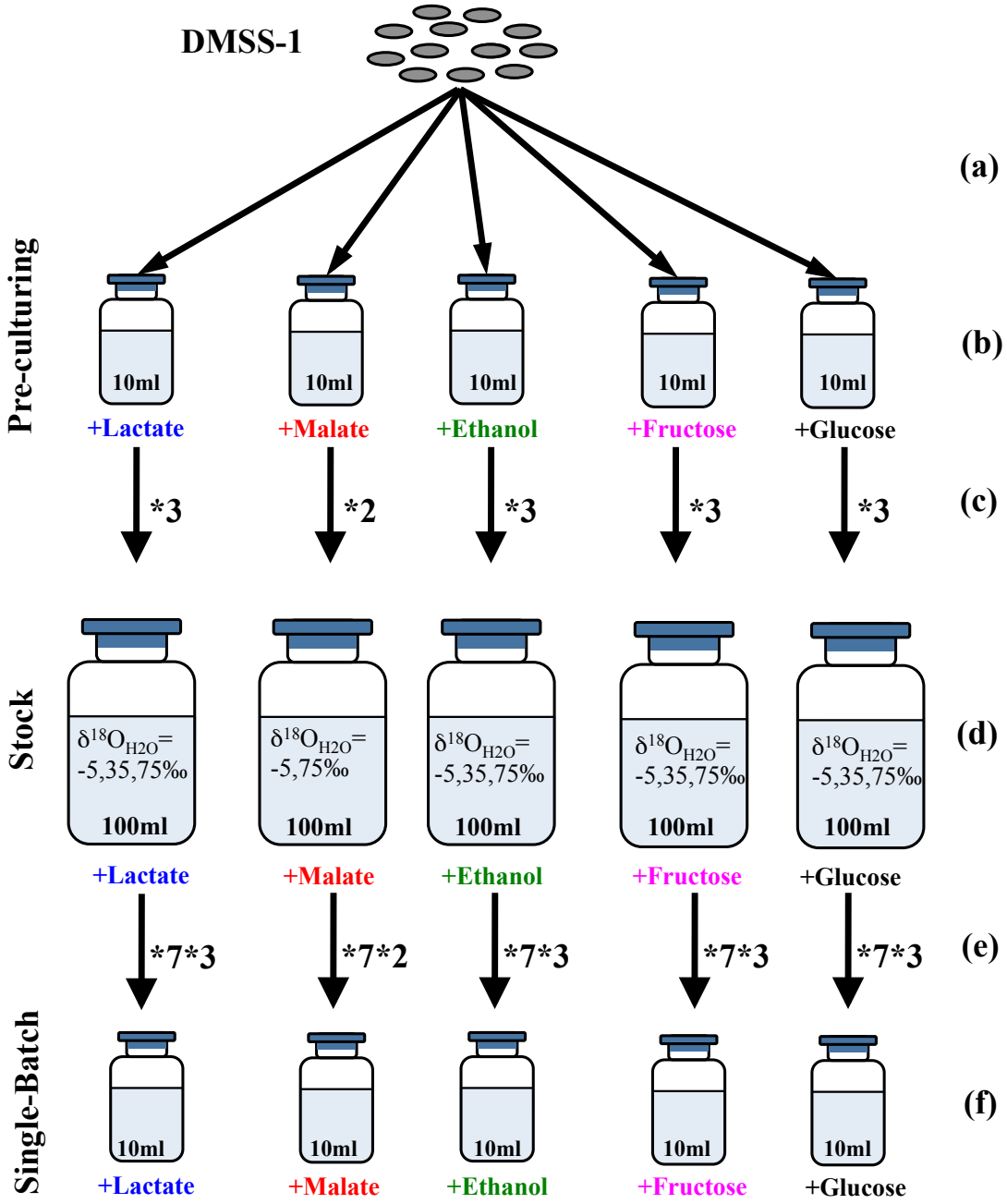

Figure 3.1: Schematic depiction of experimental preparation. Step a: inoculation of strain DMSS-1 into 5 separate mediums for pre culturing. Seop b: bacteria grow on five different electron donors (Lactate, Malate, Ethanol, Fructose and Glucose). Step c: inculcation of the bacteria into 100ml fresh medium stock after per culturing. Step e: Dividing the stock into 7 different single point batch reactors. Step f: experiment starts.

Table 3.1: Combinations of electron donors (rows) and isotopic composition of the water ($\delta^{18}O_{H2O}$ -- columns) used in experiments. '+' marks the explored combination

	-5‰	35‰	75‰
Lactate	+	+	+
Malate	+		+
Ethanol	+	+	+
Fructose	+	+	+
Glucose	+	+	+

3.1.1 Cell-specific sulfate reduction rate calculation

Many previous studies have addressed the relationship between the sulfate reduction rate (or more specifically the cell specific sulfate reduction rate) and the magnitude of the sulfur isotope fractionation. The average cell-specific sulfate reduction rate (often abbreviated as csSRR) is calculated from the ratio between the specific growth rate and the growth yield. The specific growth rates (K) of exponentially growing cells in batch culture were calculated using:

$$K=\frac{d\ln(c)}{dt} \quad (3.1)$$

Where c is the cells density (cells/ml) and t is time. The grow yield (Y) is the ratio of the change in cell density and the change in sulfate (or sulfide) concentration:

$$Y=\frac{dc}{dSO_4^{2-}} \quad (3.2)$$

csSRR is therefore equal to:

$$csSRR=\frac{K}{Y} \quad (3.3)$$

3.2 Results

All results from the pure culture growth experiments are tabulated in Appendix A.4.1. Figure 3.2 is a composite figure showing sulfate concentrations cell density and $\delta^{34}S_{SO4}$ and $\delta^{18}O_{SO4}$ measured in experiments with all different electron donors. In this figure I present only the experiments with $\delta^{18}O_{H2O}\approx75‰$, because the change in most parameters are consistent among the various experiments (independent of the $\delta^{18}O$ of the water) but the experiment with $\delta^{18}O_{H2O}\approx75‰$ was sub-sampled at the highest resolution. Sulfate concentrations decreased with time as expected during MSR, and cell densities, $\delta^{34}S_{SO4}$ and $\delta^{18}O_{SO4}$ increased with time in all experiments, showing the growth and sulfate reduction by DMSS-1 under all tested conditions. The largest and the smallest decreases in sulfate concentration were observed in the experiments with lactate and glucose, respectively, confirming that lactate stimulates faster rates of MSR than glucose. The $\delta^{34}S_{SO4}$ and $\delta^{18}O_{SO4}$ showed the opposite trend, where sulfur and oxygen isotope ratios changed more rapidly when DMSS-1 grew on glucose than when the bacterium grew on lactate.

To compare sulfur isotope fractionation among the experiments, I plot the change in $\delta^{34}S_{SO4}$ from is initial value ($\delta^{34}S_{SO4}(t)$- $\delta^{34}S_{SO4}(0)$) versus the natural logarithm of the ratio of the remaining sulfate (Figure 3.2a); The more rapid the change $\delta^{34}S_{SO4}$ versus the depletion in sulfate concentration the bigger the sulfur isotope effect. It can be seen that the highest sulfur isotope enrichment is in the glucose experiment, followed by fructose, malate, ethanol and then lactate with the smallest $\delta^{34}S_{SO4}$ change versus the depletion of sulfate. Similarly, I can use the cross-plot of $\delta^{18}O_{SO4}$ vs. $\delta^{34}S_{SO4}$ (Figure 3.3b) to demonstrate the how the relative enrichment of $\delta^{18}O_{SO4}$ and $\delta^{34}S_{SO4}$ change among the experiments. In this plot (Figure 3.3b) the higher the slope between $\delta^{18}O_{SO4}$ and $\delta^{34}S_{SO4}$ the more rapid $\delta^{18}O_{SO4}$ is changing relative to $\delta^{34}S_{SO4}$. The $\delta^{18}O_{SO4}$ enrichment versus $\delta^{34}S_{SO4}$ is the highest in the glucose experiment and the lowest in the lactate experiment.

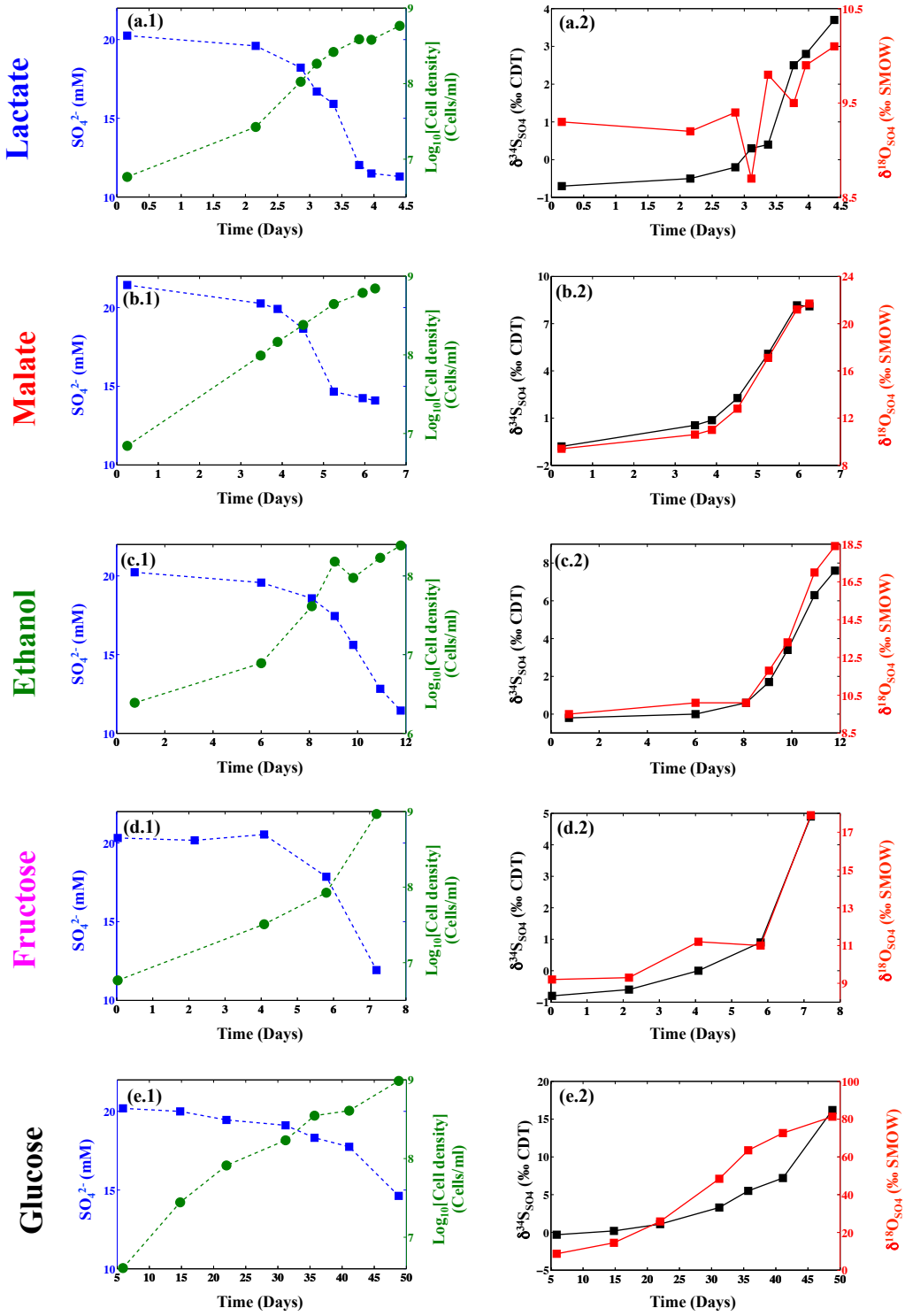

Figure 3.2: Time dependent sulfate (SO_4^{2-}) concentration and cell density (a) and $\delta^{34}S_{SO4}$ and $\delta^{18}O_{SO4}$ (b) for DMSS-1 grow on lactate (#.1), malate (#.2), ethanol (#.3) Fructose (#.4) and glucose (#.5) (where # indicates panels a and b) in the experiment with $\delta^{18}O_{H2O}$ =~75 ‰. Other results can be found in table S1 in the supplemental online material.

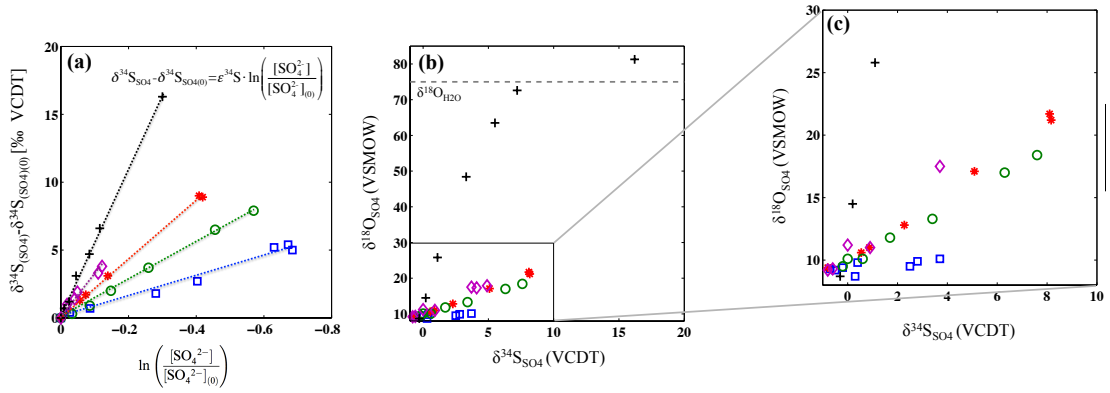

Figure 3.3: Isotope enrichment. Sulfur isotope vs. the natural logarithm of the residual sulfate fraction left in the experiment after bacterial sulfate reduction (a), $\delta^{18}O_{SO4}$ vs. $\delta^{34}S_{SO4}$ (b). The rightmost panel shows an enlargement of the middle panel (c).

3.4 Discussion

3.4.1 Placing a limit on kinetic oxygen isotope fractionation

In Chapter 2, I summarized how through the use of stable sulfur ($^{33}S/^{32}S$ and $^{34}S/^{32}S$) and oxygen ($^{18}O/^{16}O$) isotope ratios, isotope geochemistry can reveal intracellular processes during MSR. Isotopes do not necessarily react at the same rate in various chemical and biological reactions. Therefore, the ratios among various isotopes and their changes over the course of a chemical or biological reaction can provide independent information about the nature of the reaction. There are two ways through which isotopes of a given element may be partitioned, or fractionated, in the natural environment. First, kinetic isotope fractionation occurs because each isotope react at a different rate during a chemical reaction and typically, lighter isotopes reacts more quickly than the heavier isotopes. Therefore, as a reaction progresses, the product of the reaction concentrates the light isotope and the reactant pool gets progressively enriched in the 'heavy' isotope. The second mechanism by which isotopes can be partitioned is equilibrium isotope fractionation, which is the partial separation of isotopes between two molecules that are found in chemical, or isotopic,

equilibrium. In equilibrium isotope fractionation the isotopes are distributed among various chemical species such that the energy of the system is minimized.

As introduced in Chapter 1 and Chapter 2, the use of $\delta^{18}O_{SO4}$ analyzed during MSR mainly targets the reoxidation of intracellular reduced-valence sulfur, although the potential importance of kinetic oxygen isotope fractionation is becoming increasingly recognized (Brunner 2005:2012; Farquhar et al., 2008; Wortmann 2007, Turchyn 2006; Aller et al., 2010; Antler et al., 2013; Wankel 2014). Kinetic oxygen isotope fractionation during MSR further complicates interpretations of $\delta^{18}O_{SO4}$, because it can influence the apparent equilibrium value (Wortmann et al., 2007; Turchyn et al., 2010; Antler et al., 2013—see also equation 2.8 in chapter 2). Some studies have previously assumed no kinetic oxygen isotopic fractionation (Brunner et al., 2006; 2012), and some estimate an overall kinetic oxygen isotope fractionation as high as 10‰ (Wankel et al., 2014). Turchyn et al. (2010), suggested that the kinetic oxygen isotope fractionation cannot be higher than 4‰. All these assumptions lead to differing conclusions about cellular fluxes of sulfur and electrons during MSR and complicate interpretations of environmental data.

The kinetic oxygen isotope fractionation can only be studied when the effect of water-isotope equilibrium on the $\delta^{18}O_{SO4}$ is minimal; that is to say the reoxidation of intracellular intermediate valence state sulfur species is minimal. I explore this by plotting the slope of the apparent linear phase ('SALP', Chapter 2, equation 2.7) against the oxygen isotope composition of the water (Figure 3.4a). My experiments demonstrate that the oxygen isotopic composition of water affects the calculated SALP in all experiments, including conditions that previously would have been interpreted dominantly kinetically driven. Therefore, there is an equilibrium, or reoxidative, component contributing to the total sulfate-oxygen isotope fractionation under all tested conditions. However, the experiment exhibiting the smallest influence of this oxygen isotope equilibrium can place a limit on the total kinetic oxygen isotope fractionation. Thus by picking the lowest SALP among all the calculated SALPs, I can identify the upper limit for the kinetic oxygen isotope effect. Figure 3.4a shows that the kinetic isotope effect has the largest contribution to the measured $\delta^{18}O_{SO4}$ in cultures grown on lactate.

The SALP from the lactate experiment grown in water with a $\delta^{18}O_{H2O}$ of -5.3‰ is the most moderate slope calculated (Figure 3.4a). This moderate slope, 0.009 ± 0.03, indicates that the kinetic isotope effect on oxygen relative to sulfur is negligible. However, the variation in $\delta^{18}O_{SO4}$ in the lactate experiment is very small (~1‰) and the error on the analytical measurement for $\delta^{18}O_{SO4}$ is high (on the order of 0.4‰), requiring a more conservative calculation. Therefore, I consider the experiment on malate, which exhibited the second most moderate slope (Malate- Figure 3.4a). In this case, the slope was still smaller than 0.2, which suggests that the magnitude of the kinetic oxygen isotope fractionation cannot be larger than 25% of the magnitude of the kinetic isotope fractionation for sulfur isotopes. Overall, I suggest that the kinetic oxygen isotope fractionation ($\varepsilon^{18}O_{total}$) is between 0 and 5‰. This value is in agreement with Brunner et al. (2005; 2012) and the estimates derived by Turchyn et al. (2010) in pure culture studies. However, environmental studies, which find linear correlations on the $\delta^{18}O_{SO4}$ vs. $\delta^{34}S_{SO4}$ cross-plot with slopes between 0.34-0.5, require considerably higher values for kinetic oxygen isotope fractionation (Sivan et al., 2014).

The calculated $\delta^{18}O_{SO4(A.E)}$ for each of my experiments is presented in Figure 3.4b as a function of the cell specific sulfate reduction rate. It can be seen that there is an inverse correlation between the $\delta^{18}O_{SO4(A.E)}$ value and the cell specific sulfate reduction rate. As mentioned in Chapter 2, it has been suggested that the range of values often observed for the $\delta^{18}O_{SO4(A.E)}$ has been attributed to equilibration of intracellular intermediates at different temperatures (impacting the oxygen equilibrium isotope fractionation factor). However, because my experiments were conducted at the same temperature (~22ºC) and at the same time, I can rule out temperature effects on these different oxygen isotope equilibrium. Thus, other factors, related to the cell physiology and growth conditions, must modify the value of $\delta^{18}O_{SO4(A.E)}$. This correlation validates the idea that MSR can generate a range of apparent equilibrium values, rather than a fixed value, as previously suggested (Wortmann et al., 2007; Turchyn et al., 2010; Wankel et al., 2014; Antler et al., 2013). This correlation also demonstrates that in the presence of growth conditions that favour high cell-specific sulfate reduction rates, the kinetic oxygen isotope

fractionation outcompetes the equilibrium fractionation as the $\delta^{18}O_{SO4}$ equilibrium tends to infinity (as predicted by Equation 2.8 in Chapter 2).

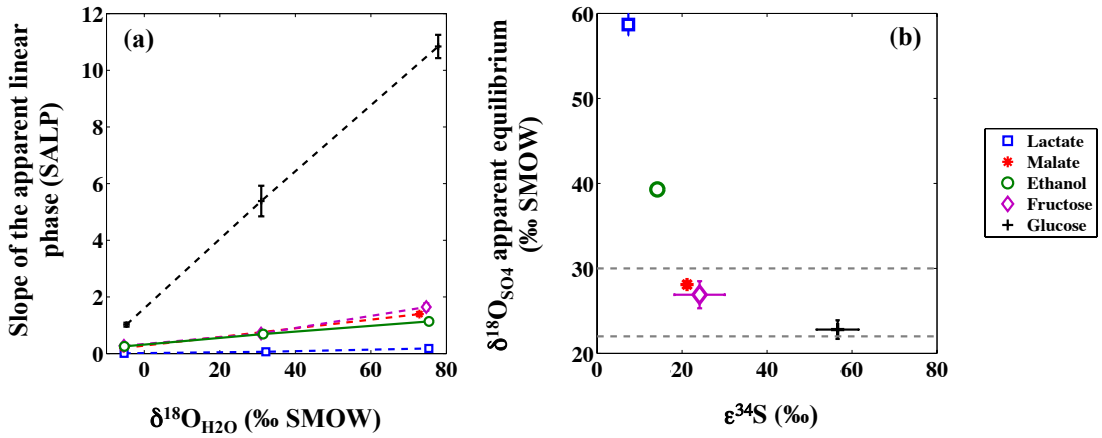

Figure 3.4: The slope of the apparent linear phase on the $\delta^{18}O_{SO4}$ vs. $\delta^{34}S_{SO4}$ cross-plot (SALP) plotted against the oxygen isotopic composition of water used in the experiments (a). The apparent equilibrium value of $\delta^{18}O_{SO4}$ ($\delta^{18}O_{SO4(A.E)}$) in each experiment plotted against the sulfur isotopic fractionation $\varepsilon^{34}S_{total}$ in each experiment (b) .

3.4.2 Tracing of intracellular sulfur metabolism during microbial sulfate reduction

Sulfur isotope fractionation in my experiments was calculated using Rayleigh-type distillation by plotting the change in the sulfur isotopic composition against the fraction of the remaining sulfate (Figure 3.3a). Similar to previous experiments with the same strain of sulfate reducing bacteria (Sim et al., 2011a,b), the sulfur isotope fractionation varied greatly, depending on the electron donor. A number of previous studies explored the relationship between the sulfate reduction rate (or cell specific sulfate reduction rate) and the magnitude of sulfur isotope fractionation in pure culture experiments (e.g. Leavitt et al., 2013; Sim et al., 2011b), in batch culture experiments with natural populations (e.g. Stam et al., 2011) or by calculating isotope fractionations from pore water fluids (e.g. Aharon and Fu, 2000; Wortmann et al., 2001). Typically, these studies report an inverse correlation between $\varepsilon^{34}S_{total}$ and the

sulfate reduction rate (e.g. Ono et al., 2014). My experiments used different organic donors to change the cell-specific sulfate reduction rate and reproduced the same inverse relationship between the cell-specific sulfate reduction rate and the magnitude of sulfur isotope fractionation (Figure 3.5a). This is consistent with previous studies of DMSS-1 in culture experiments (Sim et al., 2011a; b). This confirms that the smaller the sulfur isotope fractionation is, the lower the fluxes of intracellular sulfur intermediates that are being oxidized back to the sulfate pool. Consequently, later steps of sulfate reduction (steps 3,4 and 5 — Fig 2.1 chapter 2) have the greatest influence on the total sulfur isotope fractionation, with larger forward fluxes reducing the overall sulfur isotope fractionation (e.g. Rees 1973; Brunner and Bernasconi, 2005; Canfield 2006; Wing and Halevy, 2014).

To further explore the intracellular steps during MSR, the minor sulfur isotopes ($^{34}S/^{32}S$ versus $^{33}S/^{32}S$) provide information on the mixing among different pools within the MSR framework (see also Figure 2.2a chapter 2). As discussed in Chapter 2, plotting $E^{33}S$ (which provides information on the mixing between the different intracellular sulfur pools) versus the sulfur isotope fractionation ($\varepsilon^{34}S_{total}$) allows us to resolve some of the intracellular fluxes (up to two branch points – see Figure 2.2a for an example of this type of plot). Figure 3.5b presents the calculated $E^{33}S$ vs. $\varepsilon^{34}S_{total}$ from my experiments. It can be seen that the results from this study fall within the grey mesh of model space for $\phi_4=1$ (the flux ratio of step 4 - the reduction of sulfite to polysulfide — Figure 2.1 chapter 2). However, when I plot my data together with literature data using the same stain (DMSS-1 --Sim et al., 2011a; 2011b) it is clear that the $E^{33}S$ vs. $\varepsilon^{34}S_{total}$ data cannot be explain solely by assuming $\phi_4=1$ or $\phi_4=0$ and additional information is needed to solve the intracellular fluxes uniquely.

I can use the oxygen isotope in sulfate data to resolve this further. Figure 3.5c shows θ_O calculated from my five different electron donor experiments and plotted against $\varepsilon^{34}S_{total}$ (similar to Figure 2.2b chapter 2). The θ_O largely correlates with $\varepsilon^{34}S_{total}$, where the higher values of $\varepsilon^{34}S_{total}$ are associated with the larger values of θ_O. Notably, not all the data points fall within the envelopes for the two end member solutions ($\phi=0$ and $\phi=1$, black lines and grey lines, respectively, Figure 3.5c).

The presence of some data points outside the modelled space in $E^{33}S$ vs. $\varepsilon^{34}S$ and θ_O vs. $\varepsilon^{34}S_{total}$ plots (Figure 3.5a, b, c) is consistent with observations made by Brunner et al. (2012) and Sim et al. (2011b) using either one or the other of the plots. In practice, this indicates that previous models that account for different branching point during MSR, as constrained by stable isotopes of sulfur and csSRRs, do not adequately explain all observations that have been made in pure culture and in the natural environment. Models currently use either $E^{33}S$ vs. $\varepsilon^{34}S$ or θ_O vs. $\varepsilon^{34}S_{total}$, and simplify to two branching points (typically the reduction of APS to sulfite and the reduction of sulfite to sulfide), but should likely consider additional branching points (and enzymatic steps where sulfite is not reduced to sulfide in one step). My experiments with DMSS-1 in pure culture and different electron donors express cell-specific sulfate reduction rates that vary over two orders of magnitude. The increase in cell-specific sulfate reduction rates and the accompanying variations in the stable sulfur ($^{33}S/^{32}S$ and $^{34}S/^{32}S$) and oxygen ($^{18}O/^{16}O$) isotope ratios can be used to further explore the dynamics of MSR.

The mismatch between my data and the model space can be used to solve the rates of each of the reactions at each branching point. Because the relationships among $\varepsilon^{34}S$, $E^{33}S$, θ_O and the fluxes ratio are not linear, I solve for each individual flux ratio by minimizing the misfit. This flux ratio solution (ϕ_1, ϕ_3 and ϕ_4) is shown in Figure 3.5d as a function of the cell-specific sulfate reduction rate; all the fluxes ratios correlate with the cell-specific sulfate reduction rate. My experiments can be divided into three broad categories based on the key branching reaction: 1) Lactate experiment, with high cell-specific sulfate reduction rates and minimal reoxidation of sulfur intermediates; 2) Malate, ethanol and fructose, with moderate cell-specific sulfate reduction rates, where sulfite is likely to be the key branch point; 3) Glucose, with slow cell-specific sulfate reduction rates where the last step (the reduction to sulfide) is the key branch point.

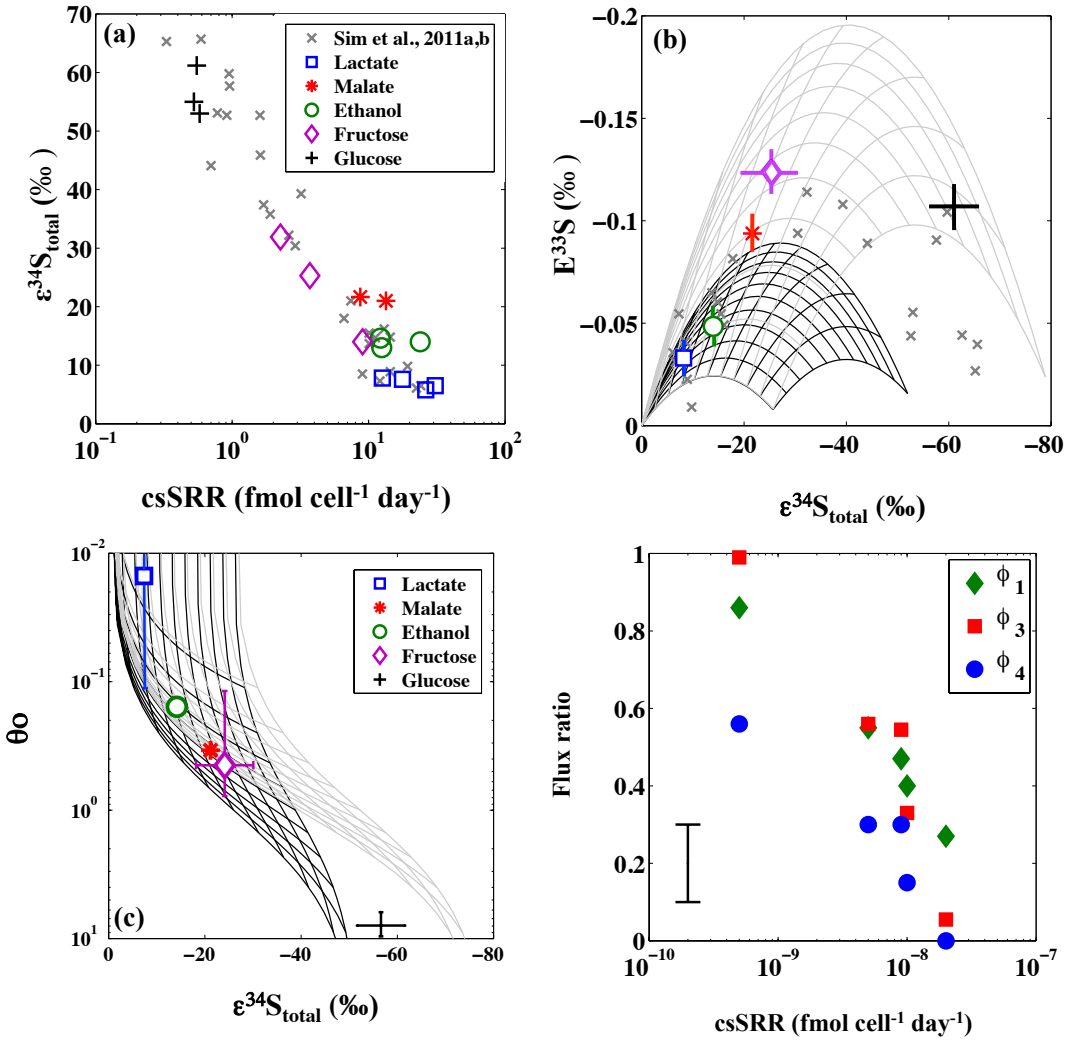

Figure 3.5: Isotopic fractionation. (a) Fractionation of $^{34}S/^{32}S$ as a function of the cell specific sulfate reduction rate (csSRR) in this study. Data from Sim et al. (2011a,b) are plotted for comparison. $E^{33}S$ vs. $\varepsilon^{34}S_{total}$ (b) and the θ_O vs. $\varepsilon^{34}S_{total}$ (c) diagram. The bottom right panel (d) is the calculated flux ratio of steps 1,3 and 4 (Figure 2.1—methods section) as a function of the cell specific sulfate reduction rate.

Oliveira et al. (2008) suggest that the DsrC protein plays a key role in the reduction of S^0 produced by DsrAB. In addition, Bradley et al. (2011) suggest that both the rate of electron supply and ratio of electrons over sulfite supplied to the Dsr subunits will impact the key sulfur intermediate, or branch point, within the reduction network. According to my flux calculation (Figure 3.5d) all steps correlate with the cell-specific sulfate reduction rate, and therefore it seems that there is no one branch

point or step that limits the process; instead, my data suggest that at each branching point the reversibility anticorrelates with the overall reduction rate. I suggest that in my experimental set up, where the electron donor was not limiting, at the onset of the reaction the reversibility of each enzyme was regulated by the cell-specific sulfate reduction rate. However, in different settings, where the electron donor or sulfate concentrations might be limited or unavailable it is possible that one of the steps will become rate-limiting.

In conclusion, I found a strong correlation between the csSRR and $\varepsilon^{34}S$, $E^{33}S$, θ_O (Figure 3.5) and $\delta^{18}O_{SO4(A.E)}$ (Figure 3.4). In addition, as was developed in chapter 2, the variation on both sulfur and oxygen isotopes is tied to the reversibility of each enzymatic step during MSR. This confirms that the reversibility of each reaction is closely related to the csSRR and likely determines it. Based on the sulfur and oxygen isotopic fractionation I also compute the reversibility of each step and find that the reversibility of all the steps (1, 3 and 4) is anti-correlates with the csSRR. Therefore, it seems like there is no one rate-limiting step, but all the reversibility of all the steps aligns with each other according to the csSRR.

3.4.3 Environmental implications

To what extent do results from pure culture experiments such as this explain the geochemical variability in the natural environment? This section addresses this question by applying my insights from pure culture experiments to $\delta^{18}O_{SO4}$ and $\delta^{34}S_{SO4}$ data from previously published pore fluids. This will lead to the next two chapters where I will apply the use of $\delta^{18}O_{SO4}$ and $\delta^{34}S_{SO4}$ data that I acquired from pore fluids I collected in various shallow marine environments. In this discussion relating pore fluid data to my pure culture experiments, the depth below the seafloor of total consumption of sulfate is used to calculate the net sulfate reduction rate: 1) sulfate is consumed over three meters below the seafloor in environments with high sulfate reduction rates (on the order of 10^{-4} to 10^{-5} mol cm^{-3} $year^{-1}$) such as estuaries and methane seeps (Aharon an Fu, 2000 & 2003). 2) Sulfate is consumed between three and ten meters in environments with moderate sulfate reduction rates (on the order of 10^{-6} mol cm^{-3} $year^{-1}$), including the continental shelf and river deltas (Aller et

al., 2010). 3) When sulfate is consumed deeper than ten meters below the seafloor, the environment is considered to have low sulfate reduction rates (lower than 10^{-7} mol cm^{-3} $year^{-1}$), exemplified by organic-poor deep-sea sediments (Turchyn et al., 2006; Wortmann et al., 2007).

Figure 3.6 plots these three categories of site (color coded) for pore fluid isotopes in a $\delta^{18}O_{SO4}$ vs. $\delta^{34}S_{SO4}$ crossplot, and overlays the curves for the relative evolution of $\delta^{18}O_{SO4}$ vs. $\delta^{34}S_{SO4}$ based on my experiments. Figure 3.6 shows a number of notable features. First, the overall variation in the data from pore fluids follows my findings, where at lower sulfate reduction rates, the $\delta^{18}O_{SO4}$ increases rapidly compared to the $\delta^{34}S_{SO4}$. Second, most of the pore fluid data fall above my laboratory-derived estimate for kinetic oxygen isotope fractionation. Lastly, data points from many field sites with moderate to low sulfate reduction rates fall above the curve of my glucose experiment, which records the highest oxygen isotope enrichment in pure culture to date.

In an open system, such as marine sediments, different transport mechanisms should modify the $\delta^{18}O_{SO4}$ and $\delta^{34}S_{SO4}$ versus those predicted from closed system batch experiments (Jørgensen, 1979; Wortmann et al., 2007). Therefore, if I want to compare my results from this study to pore fluid data, it is important to consider how the prevalence of the open system will affect the $\delta^{18}O_{SO4}$ vs. $\delta^{34}S_{SO4}$. My model in Chapter 2 suggests that using a calculation of SALP in an open system versus closed system, at the most moderate SALP the $\delta^{18}O_{SO4}$ vs. $\delta^{34}S_{SO4}$ in closed and opened system are virtually the same. When the SALP is steeper, on the other hand, closed system and open system diverge and the open system conditions moderate the calculated SALP. I suggest therefore, that the gaps between my experiments and pore fluid $\delta^{18}O_{SO4}$ vs. $\delta^{34}S_{SO4}$ data cannot be explained simply by the different transport mechanism of the open system pore fluids versus my closed system batch experiments, because the direction by which the closed system results should be modified is in the opposite directions of the mismatch between my experiments and the pore fluids.

Overall, pore fluids and pure culture experiments of microbial sulfate reducers exhibit similar trends. Some gaps between them can be explained by the much lower cell-specific sulfate reduction rates relative to batch experiments (e.g. Holmkvist et al., 2011). However, some features, such as the high oxygen isotope equilibrium values (which can be more than 5‰ higher then expected from my experiment—Figure 3.6) with high apparent SALP in pore fluids from sites with slow sulfate reduction rates may not be explained only by MSR even if I consider any potential temperature effect on the oxygen isotope equilibrium between sulfur intermediates and water. Therefore, I suggest that different processes control this relationship in those cases. For instance, in gas seeps, where sulfate-driven anaerobic oxidation of methane is present, I will demonstrate in subsequent chapters that $\delta^{18}O_{SO4}$ vs. $\delta^{34}S_{SO4}$ shows a linear correlation with moderate slopes (Aharon an Fu, 2000;2003; Rubin-Blum et al., 2014; Wehrmann et al., 2011) due to little reoxidation of reduced sulfur species (Antler et al., 2015). In contrast, in organic-poor sediments, the sulfate reduction rate is low, a extracellular complex sulfur-iron or sulfur-manganese cycling is possible, pushing the slopes on $\delta^{18}O_{SO4}$ vs. $\delta^{34}S_{SO4}$ toward much steeper slopes as $\delta^{18}O_{SO4}$ increases with minor change in $\delta^{34}S_{SO4}$ (e.g. Aller et al., 2010, Blake et al., 2006; Böttcher et al., 2006).

The next challenge will be to resolve the gap between the pure cultures experiments and *in situ* pore fluid $\delta^{34}S_{SO4}$ and $\delta^{18}O_{SO4}$. This might be enabled by the increasing availability of coupled measurements of $\delta^{34}S_{SO4}$, $\delta^{33}S_{SO4}$ and $\delta^{18}O_{SO4}$ together with csSRR. Studies of microbial cultures at even lower cell-specific sulfate reduction rates than now available may also yield even higher $\delta^{34}S_{SO4}$, $\delta^{33}S_{SO4}$ and $\delta^{18}O_{SO4}$ signals and expand the known range of oxygen and sulfur isotope fractionations accessible to MSR.

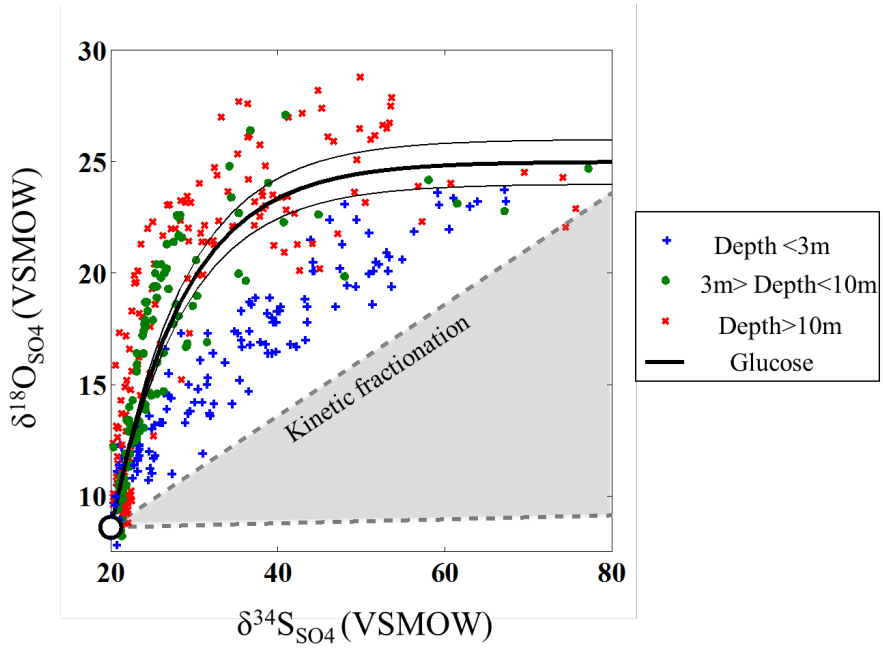

Figure 3.6: $\delta^{18}O_{SO4}$ vs. $\delta^{34}S_{SO4}$ data from pore fluids data superposed with estimation. (Data were taken from Aharon and Fu, 2000; 2003; Aller et al., 2010 Antler et al., 2013; Böttcher et al., 1998; 1999; 2006; Blake et al., 2006; Wehrmann et al., 2011; Wortmann 2006; 2007)

3.5 Conclusions

In this chapter I presented multiple sulfur and oxygen isotope data from pure culture *Desulfovibrio* sp. (Strain DMSS-1). Within these cultures on different electron donors, the cell specific sulfate reduction rates vary over two orders of magnitudes. I demonstrate how both the isotopic fractionation of sulfur and oxygen in dissolved sulfate record different processes even under controlled conditions and as a function of sulfate reduction rates. As previously shown, the $^{34}S/^{32}S$ fractionation varies between 7 and 61‰ and correlates with the cell specific sulfate reduction rates. As for the oxygen isotopes in dissolved sulfate, in this chapter, I show for the first time that oxygen isotopes can exceed the isotopic composition of the water and that the oxygen isotopes apparent equilibrium is also a function of the cell specific sulfate reduction rates. I later used these results to solve uniquely the fluxes ratios of each individual step during microbial sulfate reduction.

I also compared my pure culture sulfur and oxygen isotopes results to results from pore fluid sulfate from the literature. Although my experiments show the highest sulfur and oxygen isotopes ever recorder from pure culture, the isotopes results do not cover the entire span of the results from within the natural environment. I suggest that the gap between lab experiments and the natural environment is probably due to the fact that in the natural environment the organic matter availability is much lower then even in my slowest experiment. In addition, it is possible that other processes such as sulfur oxidation to sulfide, sulfur disproportionation and sulfate-driven anaerobic methane oxidation impact the isotopic correlation in the natural environment from the one predicted by pure culture experiments. More pure culture experiments that push down the organic matter availability even further are needed, in addition to experiments with natural population to explore the integrated of all the processes that involve sulfur on the isotopic signature of sulfur and oxygen in dissolved sulfate.

Chapter 4

Sulfur and oxygen isotope insight into sulfate-driven anaerobic methane oxidation in estuarine sediments

Estuaries sit at the transition zone between the marine and terrestrial environments and provide an ideal location to study microbial sulfate reduction and sulfate-driven anaerobic oxidation of methane (AOM). This is because estuaries often trap large amounts of organic carbon from terrestrial weathering and yet are coupled with high sulfate concentrations from the ocean. Worldwide, there are ~1200 major estuaries, covering an area of 500,000km^2 - the equivalent to almost 0.5% of the ocean floor. Because estuaries are in shallow water they can be easily sampled (unlike deeper marine sediments) and because of the high supply of organic carbon, anaerobic microbial reactions often occur higher up in the sediment column then they do in open marine sediments.

Several coastal areas in the South- and East- Mediterranean are characterized by relatively small-stream estuaries with low natural flows and a high load of organic carbon. In certain cases, as along the Mediterranean coast of Israel, the bottom bathymetry of the lower parts of the coastal streams lies below sea level, which enables the intrusion of seawater and the formation of highly salinity-stratified estuaries which can extend up to a few kilometers inland. The combination of high concentrations of sulfate (from the ocean) and fast depletion of sulfate within sediments due to high organic matter load, makes these sites ideal to investigate the sedimentary microbial sulfate reduction, sulfate-driven AOM and even deeper processes in relatively short cores.

As explored throughout this thesis, the sulfur and oxygen isotope composition of residual sulfate has been used to explore the mechanism of microbial sulfate reduction during organic matter oxidation both in pure culture (e.g. Mangalo et al., 2007; Mangalo et al., 2008; Turchyn et al., 2010; this thesis) and in the natural environment (e.g. Böttcher et al., 1998; Böttcher et al., 1999; Aharon and Fu, 2000; Aharon and Fu, 2003; Turchyn et al., 2006; Wortmann et al., 2007; Antler et al., 2013 – see introduction/Chapter 1 of this thesis). However, only recently have sulfur and oxygen isotopes in sulfate been used specifically to study sulfate-driven AOM, and to understand whether the intracellular mechanism of sulfate reduction is different when microbial sulfate redcution is coupled to AOM as opposed to generic organic matter oxidation, also known as organiclastic sulfate reduction (Deusner et al., 2014; Sivan et al., 2014). The fact that coupled sulfur and oxygen isotopes in sulfate haven't been analysed near the sulfate-methane transition zone to explore sulfate-driven AOM is partly because of the technical difficulty of measuring the isotopes of sulfate where the sulfate concentration is low.

In the last 15 years, much biological and biochemical evidence was gathered on the differences between microbial sulfate reduction coupled with organic matter oxidation versus coupled in sulfate-driven AOM, however, little is still know about how these biological and biochemical differences affect the geochemistry. In this chapter, I will investigate microbial sulfate reduction and sulfate-driven AOM at two different estuary sites, located off the Mediterranean coast of Israel (The Yarqon and the Qishon estuaries), using multi-isotope measurements to further our understanding of the dynamic of this process. I report carbon isotopes in dissolved inorganic carbon ($\delta^{13}C_{DIC}$), sulfur and oxygen isotopes in pore fluid sulfate ($\delta^{34}S_{SO4}$ and $\delta^{18}O_{SO4}$, respectively) and carbon isotopes in pore fluid methane ($\delta^{13}C_{CH4}$) as well as the concentrations of dissolved inorganic carbon (DIC), sulfate, and methane. The samples were collected off the Mediterranean coast of Israel (The Yarqon and the Qishon estuaries).

4.1 Methods

4.1.1 Study sites

The Yarqon (Site Y3-- Figure 4.1) is the largest coastal river in Israel with a length of 27.5 km and a drainage basin area of 1800 km^2. The estuary contains high organic carbon load from up-stream of 20-60 mg L^{-1} (Gafny et al., 2000) and a lower water mass close to seawater salinity. The Qishon (Site QB2-- Figure 4.1) stream drainage area occupies 1100 km^2, with intensive agricultural activity and industry taking place within the basin. The 7-km long Qishon estuary is characterized by the penetration of seawater, thereby producing a highly stratified water column. Nearby industrial plants provide high nutrients/carbon load in the Qishon estuary (Eliani-Russak et al., 2013). The salinity of the pore fluids in the two estuaries is close to the salinity of the eastern Mediterranean (Antler et al., 2013; Eliani-Russak et al., 2013) with a $\delta^{18}O_{H2O}$ of 2± 0.5%, similar to previous measurements of the $\delta^{18}O_{H2O}$ of the eastern Mediterranean (e.g. Sisma-Ventura et al., 2009). Thus the water at the boundary layer of the estuary sediments is predominantly saline Mediterranean water and the pore fluids see far less of the top layer of estuarine freshwater.

4.1.2 Sampling and samples preparation

The sediments from the Yarqon estuary (location: 32° 4.334'N, 34° 46.559'E, water depth: 2m, distance from the shore: 1km) were sampled by 50 cm long perspex tubes using a gravity corer. The sediments from the Qishon estuary (location: 32° 48.503'N, 35° 1.717'E; water depth: 4m; distance from the shore: 0.7km) were sampled by a box corer sub-sampled by 50 cm long Perspex tubes and by piston corer. The sediment was returned immediately to the lab and sliced to 1 cm slices under an argon atmosphere to avoid oxygen contamination. For methane and $\delta^{13}C_{CH4}$ measurements, a special corer with side holes (1 cm in diameter) every two centimeters has been designed for quick and more precise subsampling. Through this special corer, ~2 ml of the sediment was taken using an edge cut syringe into a flushed argon bottle containing 5 ml sodium hydroxide (1.5 N) and the bottle was

sealed with crimper.

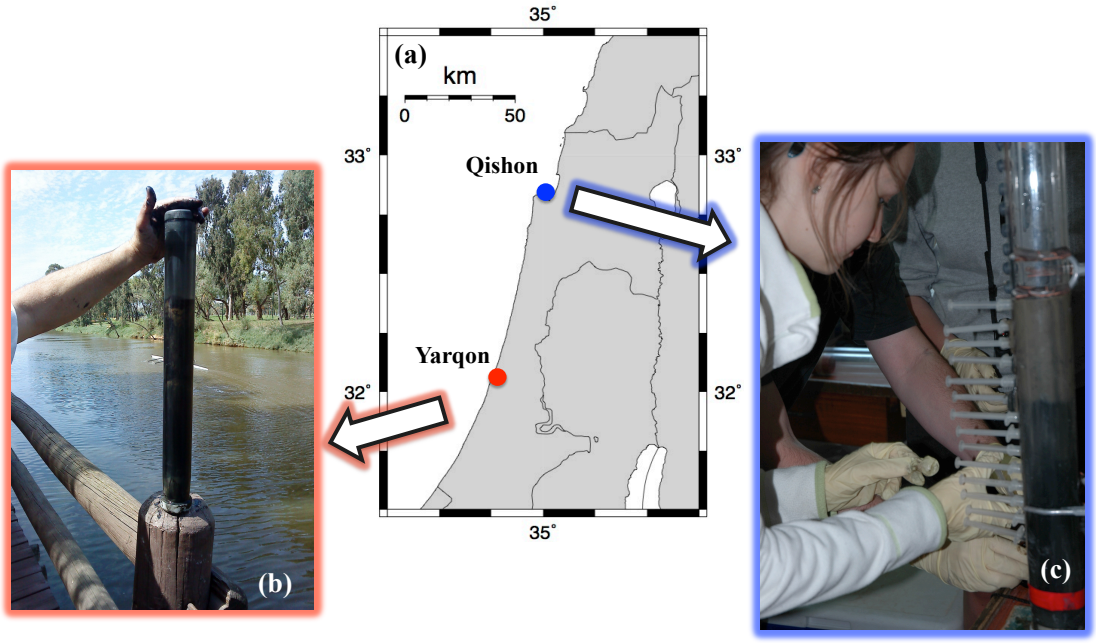

Figure 4.1: Map of the study area: Eastern Mediterranean region (a), A core from the Yarqon estuary (b), sampling at the Qishon estuary (c). The dots and the corresponding labels indicate the site locations and names, respectively.

Pore fluids were extracted using a centrifuge flushed with argon. 2 ml of filtered samples were transferred into vials for measurement of major ions and the $\delta^{18}O_{SO4}$ and $\delta^{34}S_{SO4}$. Those samples were flushed with argon for 15 minutes. Pore fluid sulfate was precipitated as barium sulfate (barite) using a saturated barium chloride solution. The barite was then washed with 6N HCl and distilled water. For the dissolved inorganic carbon and $\delta^{13}C_{DIC}$ measurements the sample was filtered (0.45 µm) and transferred into poisoned syringe containing $HgCl_2$ powder. The details of the methods are included in Chapter 2.

4.2 Results

In the Yarqon estuary (Y3—Figure 4.2) the pore-fluid sulfate concentration profile (Figure 4.2a) shows an almost linear decrease from the sediment-water interface down to complete sulfate depletion at the sulfate-methane transition zone at 15 cm. The dissolved inorganic carbon concentration profile mirrors the sulfate profile, increasing from the sediment water interface to 50 mM at 25 cm (Figure 4.2b). Methane concentrations increase from the sediment-water interface up to 0.6 mM around 11 cm depth and then level off (Figure 4.2c). The $\delta^{13}C_{DIC}$ sharply decreases from -17‰ at the sediment-water interface to -23‰ at 10 cm and remains at this value downcore. Both the $\delta^{18}O_{SO4}$ and $\delta^{34}S_{SO4}$ increase with depth, below 10 cm the increase in $\delta^{18}O_{SO4}$ moderates with depth (Figure 4.2a and 4.2d, respectively). The $\delta^{13}C_{CH4}$ values (Figure 4.2c) are scattered throughout the core and vary over a range of around 15‰.

In the Qishon estuary (QB2— Figure 4.3) sulfate is depleted by 18 cm. Similar to the profile observed in the Yarqon sediments, the dissolved inorganic carbon concentration profile mirrors the sulfate concentration profile. (Figure 4.3a and 4.3b). Methane concentrations are similar in magnitude to the Yarqon in the box corer profile, however the piston corer profile enabled us to observe an increase in methane to 2 mM at a depth of 26 cm (Figure 4.3c). In the Qishon the $\delta^{13}C_{DIC}$ decreases from -10‰ to -18‰ in the upper 10 cm, but then increases sharply to -7 ‰ by 30 cm (Figure 4.3b). As in the Yarqon, in the Qishon both the $\delta^{18}O_{SO4}$ and $\delta^{34}S_{SO4}$ increase with depth (Figure 4.2 a and d and 4.3 a and d, respectively). $\delta^{13}C_{CH4}$ data are scattered but shows 15‰ decrease below a depth of 15cm (Figure 4.3c).

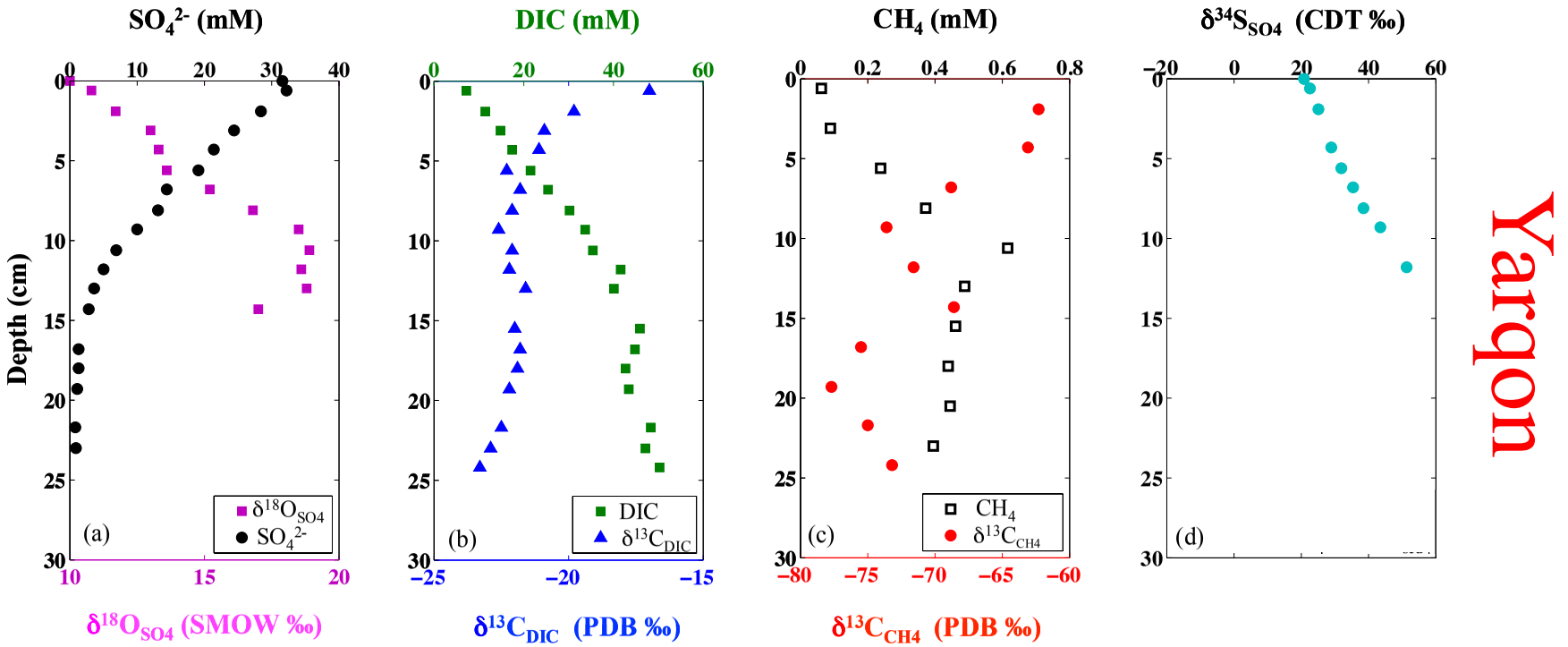

Figure 4.2: Pore fluid profiles in the Yarqon estuary at sits Y3 of sulfate concentrations and $\delta^{18}O_{SO4}$ (a), dissolved inorganic carbon (DIC) and $\delta^{13}C_{DIC}$ (b), methane and $\delta^{13}C_{CH4}$ (c) $\delta^{34}S_{SO4}$ (d).

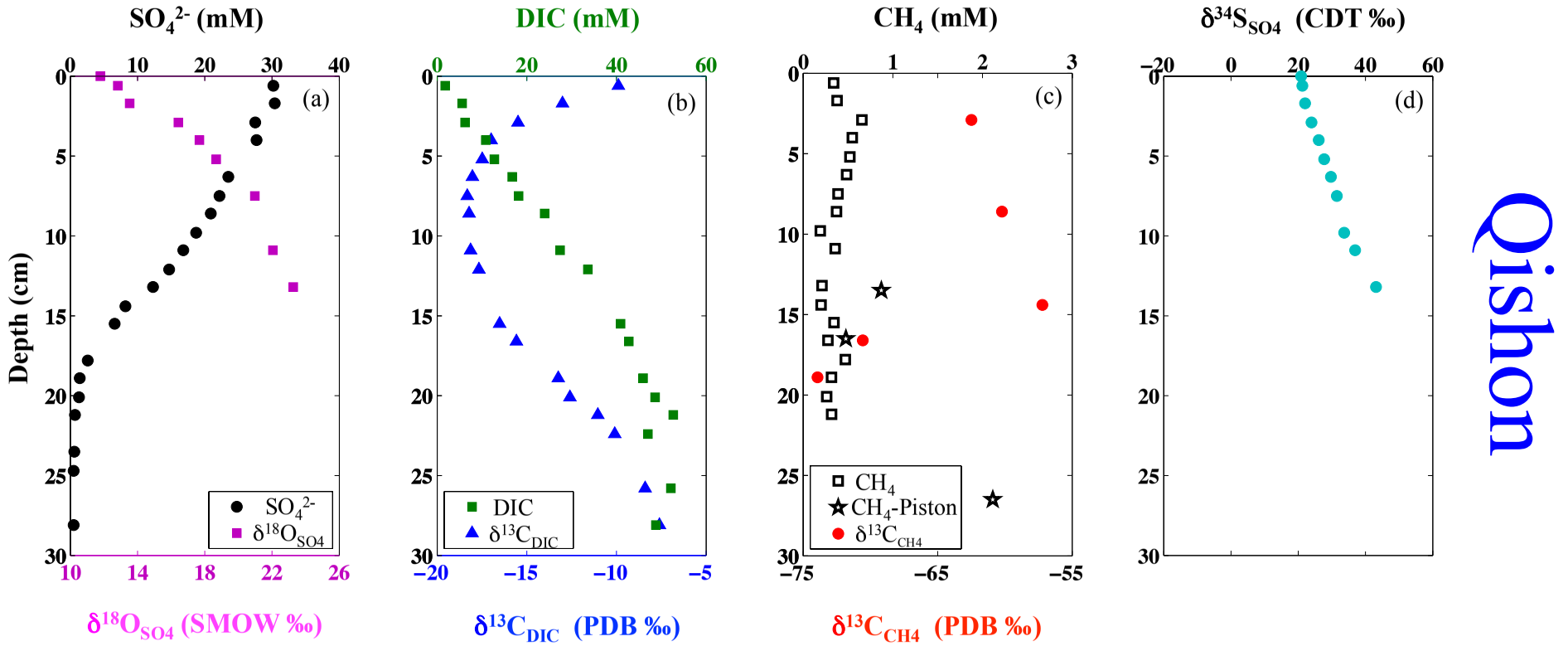

Figure 4.3: Pore fluid profiles in the Qishon estuary at sites QB2 of sulfate concentrations and $\delta^{18}O_{SO4}$ (a), dissolved inorganic carbon and $\delta^{13}C_{DIC}$ (b), methane and $\delta^{13}C_{CH4}$ (c) $\delta^{34}S_{SO4}$ (d). 'Pis' stand for samples that were taken from a piston corer.

4.3 Discussion

4.3.1 Methanogenesis and methanotrophy in the Yarqon and the Qishon sediments

At first glance, both studied sites seem to have comparable subsurface geochemistry and thus likely a similar sequence of anaerobic microbial reactions in the sediments: a decrease in sulfate concentrations and corresponding accumulation in dissolved inorganic carbon and some increase in methane concentrations (Figure 4.2 and 4.3). Both sites are good candidates for sulfate-driven AOM in a marginal marine setting. Other than the depletion of sulfate followed by the increase in methane concentration, is there other evidence for both methane production and subsurface methane consumption in these estuarine environments?

One indication for methanogenesis and methanotrophy in these estuarine sediments is the $\delta^{13}C_{CH4}$. During AOM, ^{12}C-bearing methane is preferentially oxidized leaving ^{13}C-bearing methane behind. Thus the $\delta^{13}C_{CH4}$ should become more ^{13}C depleted with depth below the depth of methanotrophy due to less methane consumption and the production of ^{13}C depleted methane below. The $\delta^{13}C_{CH4}$ profiles from the Yarqon and the Qishon cores suggest that at both sites there is subsurface methane production and consumption; $\delta^{13}C_{CH4}$ increases from around -75‰ below the sulfate minimum zone to -60‰ in the top sediments (Figure 4.2 and 4.3). This change in the $\delta^{13}C_{CH4}$ suggests there is a zone of production of methane and above it a zone of consumption of methane. However, the scattered profiles do not allow me to estimate clearly the depth distribution.

The isotopic composition of dissolved inorganic carbon ($\delta^{13}C_{DIC}$) can also provide evidence for the spatial location of methanotrophy and methanogenesis within subsurface sediments. Due to the extremely high carbon isotope fractionation during methanogenesis (up to 100 ‰—Whiticar, 1999) the resulted methane is much more ^{13}C depleted, or lighter, than the resulting or residual dissolved inorganic carbon. Methane oxidation, on the other hand, has a much smaller carbon isotope

fractionation (0-10‰— Alperin et al., 1988; Martens et al., 1999), producing dissolved inorganic carbon that has a similar carbon isotope composition to its methane precursor. The $\delta^{13}C_{DIC}$ profiles from the Yarqon and the Qishon (Figure 4.2b and 4.3b, respectively) are markedly different, although from the sediment-water interface to 7cm depth the $\delta^{13}C_{DIC}$ decreases at both of the cores, suggesting ^{12}C enriched dissolved inorganic carbon is being added to the pore fluids. However, below 7cm in the Yarqon, the $\delta^{13}C_{DIC}$ remains fairly constant (Figure 4.2b) while in the Qishon the $\delta^{13}C_{DIC}$ starts to increase again, as would be expected from the classic isotope geochemistry profiles of insitu deep methanogenesis (Figure 4.3b).

The fact that the $\delta^{13}C_{DIC}$ in the Yarqon does not increase suggests that the methane is produced much further below the studied core or that the methane is produced and consumed at the same depth (7cm in the Yarqon). If the methane is produced below the studied sediment core, then at this 'other location' a pool of isotopically heavy dissolved inorganic carbon would exist, coupled to the isotopically light pool of generated methane. That isotopically heavy dissolved inorganic carbon would need to be diffusing elsewhere, or precipitated as authigenic carbonate at the 'other location' such that I do not observe it within my studied sediment core, while the methane diffuses or advects to my studied site. The second possibility to explain the lack of change in the $\delta^{13}C_{DIC}$ below 7cm in the Yarqon is that the methane is produced at the same depth where it is consumed. This would create an isotopically closed system where the $\delta^{13}C_{DIC}$ does not change dramatically, and is not inconsistent with the measurement of isotopically light methane that I have made in the Yarqon. Since methane concentrations are two orders of magnitude less than the dissolved inorganic carbon concentration, ^{12}C-rich methane can be generated locally (in small concentration) without necessarily impacting the residual $\delta^{13}C_{DIC.}$

The difference in the $\delta^{13}C_{DIC}$ profiles between the Qishon and the Yarkon is the first suggestion that the subsurface microbial processes are different between these two sites. While the carbon isotopes suggest that the location of methanogensis and methanotrophy are different between the Yarqon and Qishon estuaries, my question is whether this impacts the link between sulfate and methane. The sulfate concentration profiles at both sites are slightly different as well. While at the Yarqon site the sulfate

concentration profile is almost linear, at the Qishon site the sulfate concentration profile is slightly concave-up. I plot the dissolved inorganic carbon vs. sulfate concentrations (Figure 4.4), which reveal that the ratio of change in sulfate versus dissolved inorganic carbon is also different between the sites. In the Yarqon sediments, the ratio of change in sulfate versus dissolved inorganic carbon is close to -1:1 (one mole of sulfate consumed to one mole of dissolved inorganic carbon generated Figure 4.4a), while in the Qishon estuary the ratio is not constant with depth and changes from almost -1:2 at the upper part of the core to -1:1 at the lower part (Figure 4.4b). This stoichiometric ratio between sulfate and dissolved inorganic carbon hints at the pathway through which sulfate is being consumed: during sulfate-driven AOM we expect a ratio of -1:1 (Similar to Burdige and Komada, 2011) between sulfate consumption and dissolved inorganic carbon production (Eq. 1.9, introduction), while in organic matter oxidation we expect a mol ratio of -1:2 for sulfate consumption to dissolved inorganic carbon production (Eq. 1.1, introduction).

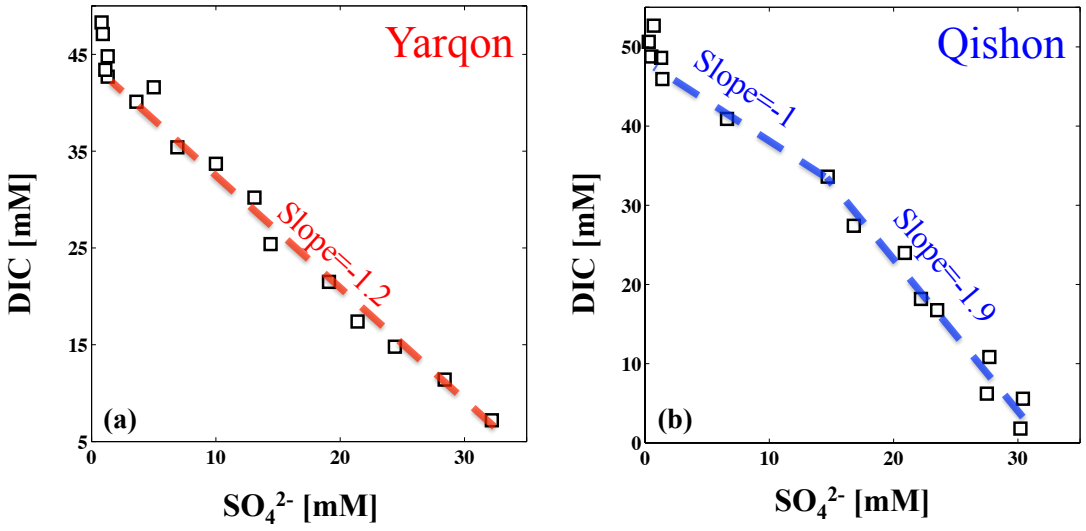

Figure 4.4: Dissolved inorganic carbon (DIC) vs. sulfate concentration from the Yarqon (a) and the Qhison (b). The slope is -1.2 at the Yarqon whereas it is -1.9 at the Qishon in the upper part of the core and it decreases to -1 in the bottom part.

This stoichiometry by itself, however, does not provide definitive evidence for the microbial processes occurring in these sediments. This is because there might be other sources and sinks of dissolved inorganic carbon (or sulfate) in the sediment that could interfere with the stoichiometrically predicted ratios. For example, oxidation of organic matter by electron acceptors other than sulfate, or subsurface precipitation of carbonate minerals could both interfere with the ratio of sulfate to dissolved inorganic carbon. Furthermore, subsurface sulfide oxidation could also interfere with the sulfate- dissolved inorganic carbon ratio. Although these may be a problem in this environment, I still conclude that the sharply different sulfate-to- dissolved inorganic carbon ratios between the sites indicate sulfate-driven AOM dominates in the Yarqon sediments and in the Qishon, the upper 10 cm are dominated by organo-clastic sulfate reduction and sulfate-driven AOM is occurring below.

Over all, although there are similarities in the concentration profiles of pore fluid sulfate, dissolved inorganic carbon and the methane concentrations between the Yarqon and Qishon estuary sites, the rate of change of the sulfate vs. dissolved inorganic carbon and the carbon isotopes (of both methane and dissolved inorganic carbon) are fundamentally different. I suggest that these differences can be attributed to different depth distributions of the microbial activity or to the reactivity of organic matter. In the Qishon, the microbial activity is spatially stacked like the 'classic' marine sulfate-driven AOM profiles, with the upper section (0-7cm) dominated by sulfate-driven organic matter oxidation, the middle section (7-15 cm) dominated by sulfate-driven AOM and the bottom section (15-30cm) dominated by methanogenesis (Figure 4.2 and 4.3). In contrast, in the Yarqon, the methane is either being produced and consumed at the same depth or is being produced elsewhere and is diffusing into the studied core, and there is little evidence that sulfate is consumed through anything other than sulfate-driven AOM.

4.3.2 Sulfur and oxygen isotope insight into the sulfate-methane coupling

As suggested above, the pore fluid profile of dissolved inorganic carbon and sulfate do not, alone, provide enough detail about the mechanism of sulfate-driven AOM in either the Yarqon or Qishon sediments. In contrast the carbon isotopes of

the dissolved inorganic carbon suggest that the distribution of methane production and consumption may be different at the two sites. Given that we have the potential for different processes between these two sites, the question is whether there is a difference in the mechanism of sulfate reduction between these two sites. As mentioned in the thesis introduction, the sulfur and oxygen isotope composition of pore fluid sulfate can yield unique insight into the understanding of the mechanism of sulfate reduction when coupled either to organic matter oxidation or to AOM.

Although both the sulfur and oxygen isotope composition of sulfate increase at both sites, the relative change in the $\delta^{18}O_{SO4}$ versus $\delta^{34}S_{SO4}$ is unique at each site, hinting that the mechanism of sulfate reduction differs between the different sulfate-driven AOM zones (Figure 4.5). The $\delta^{18}O_{SO4}$ vs. $\delta^{34}S_{SO4}$ cross-plot from the Yarqon shows two stages; until 10cm depth the $\delta^{18}O_{SO4}$ increases moderately relative to the $\delta^{34}S_{SO4}$ (=0.37— Figure 4.5a), but deeper in the sediment the $\delta^{18}O_{SO4}$ remains constant while $\delta^{34}S_{SO4}$ increases. At the Qishon the slope between the $\delta^{18}O_{SO4}$ and $\delta^{34}S_{SO4}$ is almost double that of the Yarqon, but becomes more moderate at depth (Figure 4.5a— solid line). However, due to poor sampling resolution (low sulfate concentration yields small amount of barite which is then not sufficient for $\delta^{18}O_{SO4}$ and $\delta^{34}S_{SO4}$ analysis), I suggest that the moderation of the slope in the Qishon may actually be concave, as has been seen at other sites (e.g. Böttcher et al., 1998; Aller et al., 2010; Antler et al., 2013) and not necessarily a two-step curve (Figure 4.5a- dashed line).

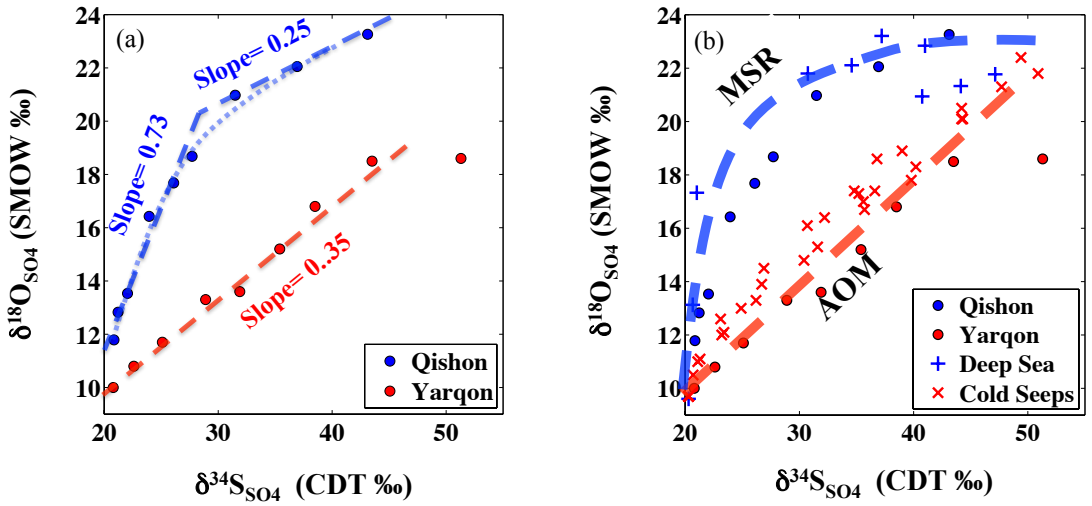

Figure 4.5: $\delta^{18}O_{SO4}$ vs. $\delta^{34}S_{SO4}$ from the Yarqon (site Y3- red) and the Qishon (site QB2- blue) estuaries (Israel), the solid lines are two-stages linear fit, and the dashed line is the option of concaved curve (a), and data from Organic-carbon poor deep-sea sediment (Turchyn et al., 2006) and cold seeps (Aharon and Fu 2000). The dashed lines are schematic.

Extending this type of dataset to other sulfate-methane transition zones would allow us to probe how different mechanisms of sulfate-driven AOM are manifest in subsurface isotope geochemistry. However, the paucity of isotope data from similar marginal marine environments makes this comparison tricky. The slope of $\delta^{18}O_{SO4}$ vs. $\delta^{34}S_{SO4}$ seems to be pointing to environmental controls on the mechanism of sulfate reduction. For example, Aharon and Fu (2000) studied the relationship between $\delta^{18}O_{SO4}$ and $\delta^{34}S_{SO4}$ in the Gulf of Mexico and found that the slope emerging between $\delta^{18}O_{SO4}$ vs. $\delta^{34}S_{SO4}$ is as low as 0.29 during sulfate reduction associated with gas seeps. On the other hand, in natural environments where no methane was detected and microbial sulfate reduction proceeds via organoclastic oxidation, the slope between $\delta^{18}O_{SO4}$ vs. $\delta^{34}S_{SO4}$ is normally steeper than 0.8 (compiled by Antler et al., 2013). I plot these two extremes of the slope of $\delta^{18}O_{SO4}$ vs. $\delta^{34}S_{SO4}$ together with data from the current study (Figure 4.5b): I used the data from Turchyn et al. (2006) (ODP site 1086, leg 175, located in the West African Margin in 780 m deep water) as a representative of an organoclastic sulfate reduction dominated site, and the data from Aharon and Fu (2000) (located in the Gulf of Mexico, water depth of 591m) as

representative of a site where sulfate-driven AOM dominates. The data in blue on the furthest left represent microbial sulfate reduction only through organic matter oxidation (the data is from a organic carbon-poor deep-sea sediment site) while the data in red is the data from the gas seep in the Gulf of Mexico (Aharon and Fu, 2000). The Yarqon and Qhison data fall between these extremes, however the data from the Qishon are closer to the organic-carbon-poor deep-sea sediment site and the data from the Yarqon are more similar in slope to the gas seep site with dominated sulfate-driven AOM.

The shape of the $\delta^{18}O_{SO4}$ vs. $\delta^{34}S_{SO4}$ cross-plot holds information about the recycling of sulfur intermediates during microbial sulfate reduction, as discussed in the introduction (Brunner et al., 2005; Turchyn et al., 2006; Wortmann et al., 2007; Brunner et al., 2012; Antler et al., 2013). The quicker the $\delta^{18}O_{SO4}$ changes relative to $\delta^{34}S_{SO4}$ (or the steeper the slope on a cross plot like in Figure 4.5) the more sulfate is brought into the cell, exchanges oxygen atoms with water, and is returned back to the extracellular sulfate pool, relative to the amount that is reduced (Bruner et al., 2005; Antler et al., 2013). In contrast, when the $\delta^{34}S_{SO4}$ evolves more rapidly than the $\delta^{18}O_{SO4}$ (a shallower slope on a cross plot like Figure 4.5), then more sulfate is brought into the cell and reduced, and less is intercellularly recycled back to sulfate. Changes in the slope of the isotopes in $\delta^{18}O_{SO4}$ vs. $\delta^{34}S_{SO4}$ space likely indicate changes in the mechanism of which sulfate is been reduced (changes in the intercellular forward and backward fluxes).

There are other factors that can impact the relationship between $\delta^{18}O_{SO4}$ and $\delta^{34}S_{SO4}$ that may be important within these estuary sediments. For example anaerobic sulfide oxidation within marine sediments would produce sulfate that has a low $\delta^{34}S_{SO4}$ and a $\delta^{18}O_{SO4}$ close to the $\delta^{18}O$ of the water (e.g. Aller et al., 2010); this would drive the uppermost pore fluids both lower in their sulfur and oxygen isotope compositions. Also, if sulfide is partially reoxidized and then undergoes disproportionation this would also impact the slope of $\delta^{18}O_{SO4}$ vs. $\delta^{34}S_{SO4}$, although this would have a variable effect on the isotopes given the pathway of disproportionation (Cypionka et al., 1998; Böttcher et al., 2001; Böttcher et al., 2005; Böttcher and Thamdrup, 2001; Aharon and Fu, 2003). I assume that these processes

are less important in these estuary sediments than the dominant process of sulfate-driven AOM. In addition, if the sulfate concentration is not in steady state, as the sulfate concentration profile in the Qishon may suggest, this can impact the relationship between $\delta^{18}O_{SO4}$ and $\delta^{34}S_{SO4}$. Aller et al. (2010) has shown that the impact of the non-steady state sulfate concentrations on the $\delta^{18}O_{SO4}$ vs. $\delta^{34}S_{SO4}$ is not dramatic. In addition, in the Qishon and the Yarqon, the characteristic time scale of diffusion of sulfate is at least an order of magnitude higher than in the sediment that Aller et al. (2010) studied and therefore the $\delta^{18}O_{SO4}$ vs. $\delta^{34}S_{SO4}$ relationship should be much more resilient to perturbations in sulfate concentration. Finally, the uppermost pore water consists mainly of seawater at both sites with similar oxygen isotopic composition of the water. This rules out that the difference between the two sites is a result of a different water source.

For these two estuaries, I suggest that as the slope of $\delta^{18}O_{SO4}$ vs. $\delta^{34}S_{SO4}$ decreases with depth at both studied sites this indicates a shift in the mechanism of microbial sulfate reduction (Figure 4.5a). In the Yarqon, where this moderation is not linked to other geochemical changes with depth in the core, I suggest that this moderation may reflect a subtle change of the percentage of recycling of sulfur intermediates, or the point where the oxygen isotopes have reached 'apparent equilibrium' with water. On the other hand, in the Qishon, the change in the slope of the $\delta^{18}O_{SO4}$ vs. $\delta^{34}S_{SO4}$ cross-plot is synchronous with the break in slope in dissolved inorganic carbon:sulfate space (Figure 4.4) and the change in the carbon isotopes of pore fluid dissolved inorganic carbon. This suggests that the sulfur and oxygen isotopes in sulfate shift in the Qishon in response to a change in the type of the electron donor used by the sulfate reducing bacteria from organic matter to methane. The reason for this difference in the mechanism of the sulfate reduction may be connected to the depositional setting of each of the site. I speculate, that the high organic content (TOC) in the Qishon (~10%) versus the Yarqon (~2.5%) may promote organoclastic sulfate reduction over sulfate-driven AOM (Sivan et al., 2007; Pohlman et al., 2013) at the upper part of the sediment.

Recent studies have found that the pathway by which sulfate is being reduced during sulfate-driven AOM may be fundamentally different than during microbial

sulfate reduction (Holler et al., 2011, Milucka et al., 2012). During sulfate-driven AOM, zero-valent sulfur was found to be a key intermediate, which later can be disproportionated resulting in sulfide and sulfate (Milucka et al., 2012). The impact of this fundamentally different mechanism on the $\delta^{18}O_{SO4}$ vs. $\delta^{34}S_{SO4}$ is not yet clear. Steeper $\delta^{18}O_{SO4}$ vs. $\delta^{34}S_{SO4}$ is typically correlated to higher percentage of recycling of sulfur intermediates (Brunner et al., 2005; Brunner et al., 2012; Antler et al., 2013). My results suggest that during sulfate-driven AOM, less sulfur intermediates are being re-oxidized back to sulfate compared to organoclastic sulfate reduction.

Another possibility is that the linear trend found in the $\delta^{18}O_{SO4}$ vs. $\delta^{34}S_{SO4}$ cross plot at sites with sulfate-driven AOM is a result of mixing through diffusion of sulfate with two isotopic end members. This explanation however has been challenged due to the different environmental setting of the sediments from the Yarqon estuary and the Gulf of Mexico, with significantly different temperature, porosity, water pressure and sedimentation rate, which impact the rate of diffusion of sulfate and its different isotopologues.

4.4 Summary and conclusions

In this chapter I presented pore fluid isotopes and concentration measurements from two estuaries, the Yarqon and the Qishon. These pore fluid profiles had steep redox gradients, including depletion of sulfate concentration with depth and a corresponding increase in the concentrations of dissolved inorganic carbon and methane. Although these two estuaries are similar in many regards, the zonation of various processes differs between the two sites. The data indicate that in the Qishon, organoclastic sulfate reduction takes place in the upper part of the sediment and sulfate-driven AOM occurs below. In contrast, at the Yarqon, the entire sediment is mostly dominated by sulfate-driven AOM. I suggest that the use of multiple isotopic and geochemical measurements elucidate these differences.

In addition, the $\delta^{18}O_{SO4}$ vs. $\delta^{34}S_{SO4}$ pattern at these two sites is different; this suggests different pathways for the sulfate to be reduced and recycled. My data, together with data from the literature reveals that the $\delta^{18}O_{SO4}$ vs. $\delta^{34}S_{SO4}$ for the

Qishon is similar to sites from organic-carbon poor deep-sea sediments where organoclastic is dominates, whereas the Yarqon is similar to cold seeps, which are dominated by sulfate-driven AOM. I suggest that the different $\delta^{18}O_{SO4}$ vs. $\delta^{34}S_{SO4}$ patterns are the result of different mechanisms during this processes. However experiments with natural sediments are required to rule out the effect of diffusion or advection that may result in linear correlation between $\delta^{18}O_{SO4}$ vs. $\delta^{34}S_{SO4}$ in cold seeps. These patterns have the potential to provide a unique geochemical fingerprint for each process, and therefore aid us in assessing the location of these processes within marine or marginal marine sediments. In addition, this fingerprint could potentially be preserved in the geological record in the form of carbonate-associated sulfate particularly in authigenic carbonates. This will be explored later in the thesis.

Chapter 5

Sulfur and oxygen isotope tracing of sulfate driven anaerobic methane oxidation in the South-Eastern Mediterranean

In the last chapter I explored how, within estuarine sediments, changes in sulfate and methane concentrations in pore water can be used to assess the nature and coupling of sulfate consumption to methane oxidation. In that chapter I was able to demonstrate that the intracellular mechanism of MSR is different when sulfate reduction is coupled to methane oxidation versus when it is coupled to organic carbon oxidation. Now I would like to explore the nature of the mechanism of MSR in sulfate-driven AOM. The zone where this sulfate-driven AOM occurs doesn't always look the same, and can be divided broadly into two types largely related to the methane flux. The first type is a sharp sulfate-methane transition depth where chemical reactions zones are distinct: a methane-devoid zone in the upper parts of the sediment and sulfate-devoid zone below. In this case, microbial sulfate reduction quantitatively consumes the methane diffusing upwards from the lower zone of methane production. The second type of sulfate-driven AOM occurs where methane 'seeps' from the sediment surface into the water column; in this case there is no sharp transition zone in the geochemistry of the pore fluids between where sulfate and methane are present, and methane escapes full consumption and can 'bubble' out of the sediment. Because sulfate-driven AOM leads to an increase in pH and alkalinity, carbonate precipitation is often associated both with methane seeps and at the sulfate-methane transition zone. Both of these types of sulfate-methane transition zones can be observed in the sediment of the Eastern Mediterranean Sea, albeit at different depths and locations.

The shallow sediments of the South-Eastern Mediterranean continental shelf are affected by the current oligotrophic conditions and contain low overall organic carbon concentrations (<1 weight%), and have not been extensively investigated previously. In spite of the low overall organic carbon content in these sediments, Schattner et al. (2012) interpreted a band of high-amplitude scattered reflectivity observed in high (~0.3 m) resolution seismic profiles across this part of the continental shelf (northern Israel) to reflect the presence of a 'gas front' within the seafloor sediments at water depths between 37 and 112 m. This presence of gas, deep in the sediments suggests that somewhere above the gas a sulfate-methane transition zone would exist in these sediments. Schattner et al. (2012) also observed repeatedly (over ~3 years) acoustic reflectivity in the water column above the seafloor, which they concluded represented active gas seepage. Thus it seems that there is both a sulfate-methane transition zone in the sediments as well as the possible presence of a methane seep.

In many ways these findings weren't a surprise. The deeper water South-Eastern Mediterranean Sea is a hotspot of methane and other hydrocarbon seepage (Coleman & Ballard 2001; Heijs et al. 2007; Loncke 2004; Mascle et al. 2006; Omoregie et al. 2008; Omoregie et al. 2009). During the 2011 exploration season of the *Nautilus E/V*, gas/fluid-charged sediments emitting methane and other hydrocarbons, possibly associated with deeper reservoirs of natural gas, were discovered at a water depth of approximately 1000m in the area of small faults and scarps within Palmachim disturbance feature in the Levantine basin (Coleman et al. 2012). These sediments were associated with visible gas bubbling at the sampling location and the presence of biogenic carbonates, resulting from the AOM-induced alkalinity shift (Knittel & Boetius 2009). I participated in this cruise and in one other cruise to shallower sediments on the Eastern Mediterranean shelf. In this chapter I will explore the relationship between sulfur and oxygen isotopes in dissolved sulfate during sulfate-driven AOM at methane seeps and at the sulfate methane transition zone in both the deep and shallow sediments of the South-Eastern Mediterranean from samples acquired during 2011 *Nautil*us E/V field session and 2013 R.V. Shikmona off the shore of Israel.

5.1 Methods

5.1.1 Study sites

Samples were collected during the 2011 *Nautil*us E/V field season at a water depth of 1134 meters. Nautilus E/V is equipped with *Hercules* and *Argus* Remotely Operated Vehicle (ROV) systems, which are able to collect high-resolution video, oceanographic data, and precision sampling. Acre 'black patch' and Palmachim 'gas seep' cores were taken with 7 cm diameter, 30 cm long pushcores. The 'black patch' was observed and sampled at the Acre location, 32°56.1464′ N 34°46.9735′ E, at water depth of 1099 m (Acre core—Figure 5.1). Since the patch was present on a slope of a pockmark (70°-90°), the cores were taken at this location perpendicularly to the sediment surface by hovering ROV and were virtually horizontal. Separate cores were taken for the quantitative and isotopic analysis of methane and sulfate and for the determination of microbial populations. The 'gas seep' location was sampled at the Palmachim disturbance, at 32°08.9668′ N 34°07.6177′E (Palmachim) (Figure 5.1).

In shallower sediments, Core PC-6 (32.921567′ N 34.902367′ E) was obtained in August 2013 on the R.V. Shikmona in undisturbed seafloor sediments at water depth of 49m (Figure 5.1). The sediment core (5.5 m long) was collected by a benthos 2175 piston corer. The study site location was chosen because it was on top of high-amplitude scattered reflectivity, interpreted to be related with the presence of free gas bubbles (Schattner et al. (2012) 'Gas Front'). The actual coring location corresponds in general to relatively shallow interpreted gas related reflectivity. The sediment cores were sliced on board every 40-50 cm within minutes of the core extraction from the seafloor.

For methane measurements at Acre and Palmachim, a special corer with side holes (1 cm in diameter—similar to the core used in chapter 4) has been designed for quick and more precise subsampling in order to reduce the amount of methane lost

during sampling. Because methane is still likely lost during sampling, our measurements are minimum methane concentrations.

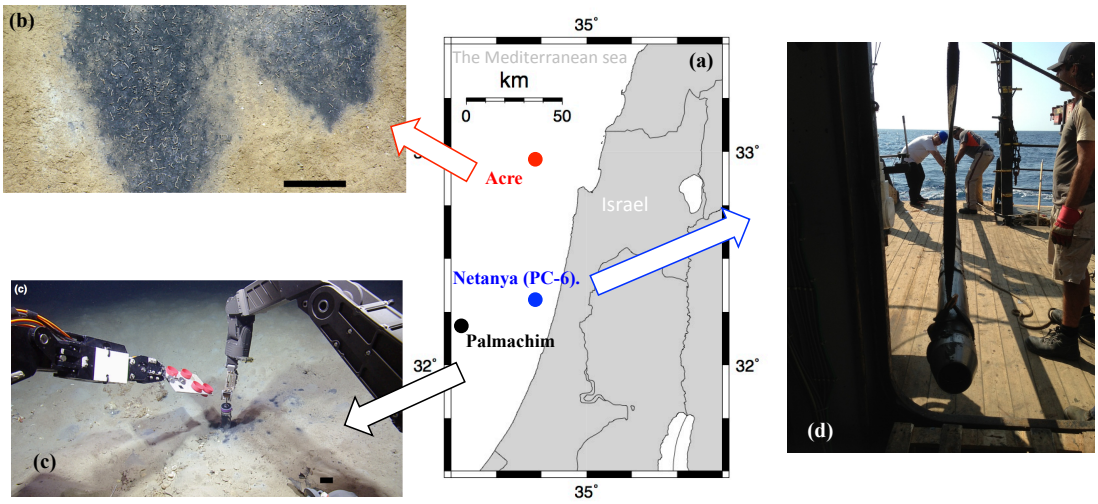

Figure 5.1: Map of the study area in a map of the Eastern Mediterranean region (a). Sampling at Arce (b), Palmachim (c) and Netanya (d) sites.

5.2 Results

The sediment and pore water profiles from the shallow core PC-6 and the deeper cores at Acre and Palmalchin are shown in Figures 5.2 and 5.3. Sulfate concentrations decrease from 27 mM to 5 mM over 7 cm at Acre, and from 32 to 16 mM over 12 cm at Palmachim (Figure 5.2a). Methane concentrations at the Acre site were variable around 0.27 mM in the upper part of the core peaking at 0.77 mM at 1.5 cm and 1.4 mM at 4.5 cm. At Palmachim, methane concentrations were lower at 0.03 mM in the upper part of the core, but peaked at 0.77 mM at 14 cm (Figure 5.2). The dissolved inorganic carbon increased from 4mM to 11mM over 11cm at Acre.

At the shallower site, PC-6, sulfate concentrations decreased with depth until reaching the sulfate methane transition zone at 3.5 meters below the seafloor. Methane concentrations then increased to 0.5 mM over the next meter. The dissolved

inorganic carbon concentration increased with depth from 2 mM to 25 mM (Figure 5.3).

The isotope results are presented in Figures 5.2 and 5.3. At Acre, the maximum $\delta^{34}S_{SO4}$ - 54‰ - was found between 6 and 9 cm below the sediment-water interface, the $\delta^{18}O_{SO4}$ at this depth reaching 20.4‰. As a reminder, seawater has a $\delta^{34}S_{SO4}$ of 20.3‰ and a $\delta^{18}O_{SO4}$ of 8.6‰; Figure 5.2e. The $\delta^{13}C_{CH4}$ had a minimum of -80 ‰ at 5.5 cm. The $\delta^{18}O_{SO4}$ / $\delta^{34}S_{SO4}$ and $\delta^{13}C_{CH4}$ profiles are mirror images of one another, as sulfur and oxygen isotopes in sulfate increase, the carbon isotope composition of the methane decreased (Figure 5.2e). At Palmachim, the $\delta^{34}S_{SO4}$ and $\delta^{18}O_{SO4}$ increased 32 ‰ and 14‰, respectively, reaching their maximum at 10.5 cm below the sediment water interface. The $\delta^{13}C_{DIC}$ also decreased sharply, from -19‰ -52‰ over these 10.5 cm (Figure 5.2f). At the shallower site, PC-6 both $\delta^{34}S_{SO4}$ and $\delta^{18}O_{SO4}$ increase with depth 35‰ and 25‰, respectively (Figure 5.3d and e). The $\delta^{13}C_{DIC}$ decreased to -25‰ at the sulfate-methane transition zone. Below that depth the $\delta^{13}C_{DIC}$ increased to -20 ‰ (Figure 5.3f). Only two measurements of $\delta^{13}C_{CH4}$ are available below the sulfate-methane transition zone, measured at -93‰ (Figure 5.3g).

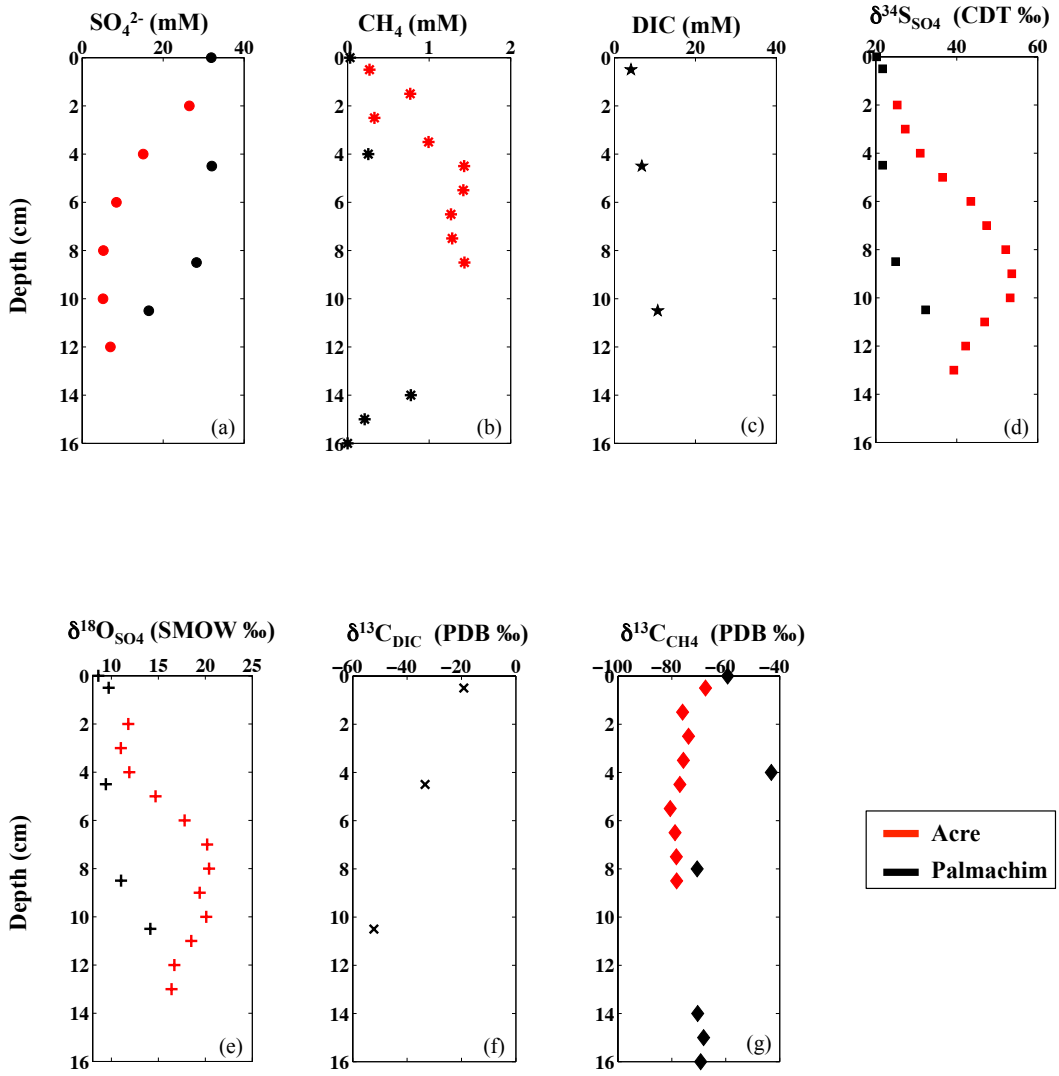

Figure 5.2: Chemical and isotopic depth profiles in pore water from sediment cores collected during the 2011 Nautilus E/V field season and on the R.V. Shikmona from the Mediterranean continental shelf of Israel at 1000m water depth.

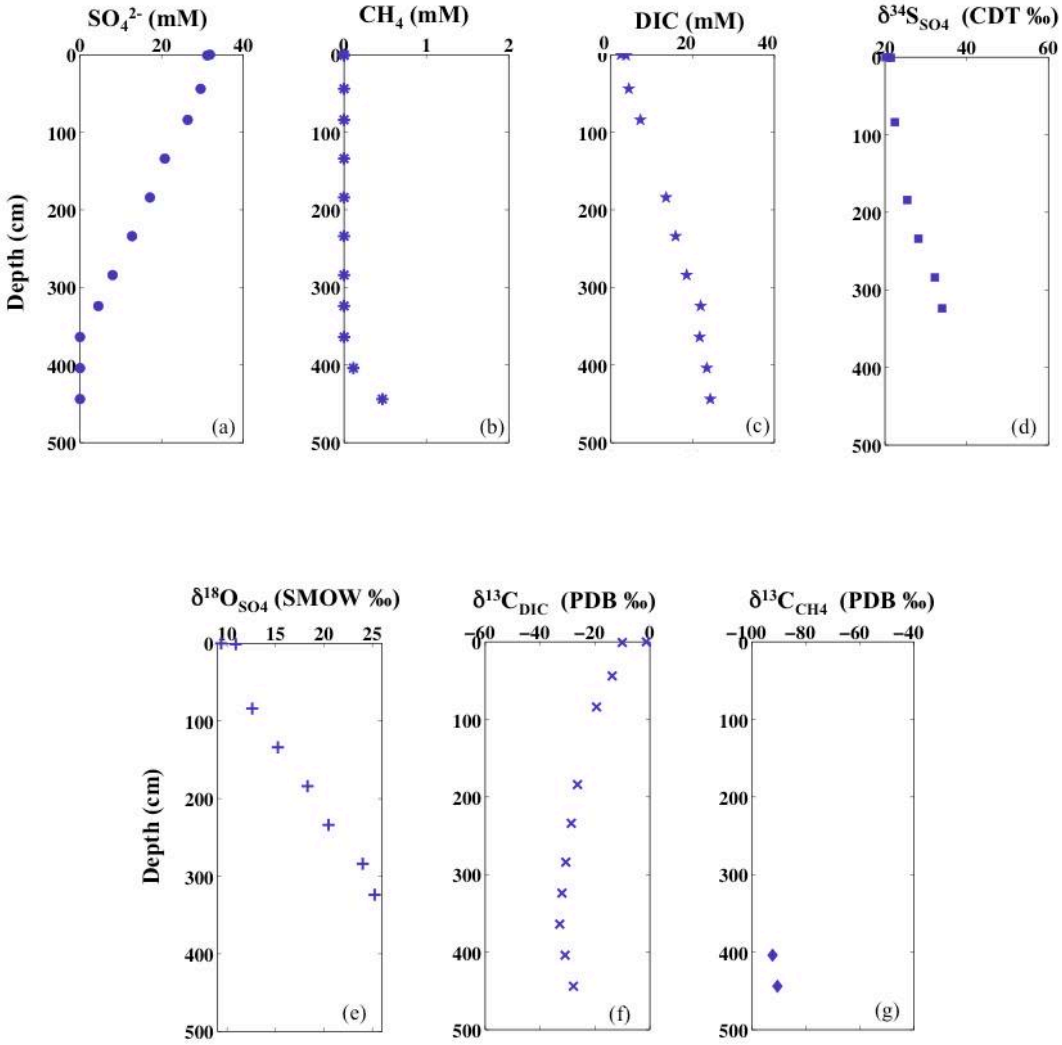

Figure 5.3: Chemical and isotopic depth profiles in pore water from sediment cores collected in August 2013 off the coast of Netanya (PC-6) at 50m water depth.

5.3 Discussion

5.3.1 Methanogenesis and methanotrophy in the South-Eastern Mediterranean

The pore fluid geochemistry provides evidence of the different microbial processes that occur within the sediment. In all sites studied, both the two deep and one shallow, methane concentrations increase and sulfate concentrations decrease

with depth below the sediment-water interface (Figure 5.2 and 5.3); this is suggestive of methane production and oxidation and microbial sulfate reduction. The hypothesis that these sites contain methanogenesis, methanotrophy, and microbial sulfate reduction is supported by the changes in the carbon isotope composition of the methane and the changes in the sulfur and oxygen isotope composition of the sulfate, as introduced in the previous chapter.

The presence of high concentrations of methane at these sites does not alone require microbial methanogenesis, as there are two processes for methane production. Methane produced during the decomposition of organic matter under high pressure and temperature condition is thermogenic. The carbon isotope composition of thermogenic methane is between -20 and -60‰ (Schoell, 1988). The second natural production pathway for methane occurs in anaerobic environments by archaea. The carbon isotopic composition of methane originated from this process is ~-50 to -110‰ (Schoell, 1988). All the sites discussed in this chapter show an extremely depleted $\delta^{13}C_{CH4}$ value that ranges between ~-40 and -90‰. Such a light isotopic signature is indicative that methane at these sites was made microbially.

Another important question regarding the dynamic of methane in these sites is the location of methane production. We can use the geochemistry to determine whether the methane was produced in situ or it advected from greater depths, similar to Chapter 4. Specifically the carbon isotope composition of dissolved inorganic carbon tends to decrease when methane is oxidized, and increase when methane is produced. For example at site PC-6, there is a large increase in the $\delta^{13}C_{DIC}$ in the deep part of the sediments which is due to methanogenesis, and it fits the hypothesis of *in-situ* production of methane just below the sulfate-methane transition zone. However, there is no direct evidence of *in-situ* methanogenesis at either deep sits Arce and Palmachim. These two cores did contain abundant Achaea that are often associated with methanogenesis such as *Methanococcus* and *Methanococcoides* (Rubin-Blum et al., 2014): this suggests microbial methane production although there is no 'smoking gun' for this process as microbial presence does not necessarily require their activity.

Due to the nature of hydrocarbon seeps, it is difficult to determine the precise relationship between sulfate and methane, based on the concentration profiles at Palmachim and Arce alone; methane in these sites is 'in excess', and it escapes as bubbles from the sediment to the overlying water, so the standard diffusion-dominated pore fluid profiles are not as readily established. To explore this further, the dissolved inorganic carbon and $\delta^{13}C_{DIC}$ can be used to try to determine the source of the dissolved inorganic carbon, and if it comes from methane oxidation or other organic matter oxidation. To calculate the carbon isotopic composition of the source molecule ($\delta^{13}C_{source}$) I use the an isotopic mass balance equation as followed:

$$\delta^{13}C_{source}=\frac{\delta^{13}C_{DIC(z)}\cdot DIC_{(z)}-\delta^{13}C_{DIC(0)}\cdot DIC_{(0)}}{DIC_{(z)}-DIC_{(0)}} \quad (5.1)$$

where $\delta^{13}C_{source}$ is the carbon isotopic composition of the source, $\delta^{13}C_{DIC(z)}$, $DIC_{(z)}$, $\delta^{13}C_{DIC(0)}$ and $DIC_{(0)}$ are the carbon and the isotopic composition at z and 0 depth, respectively.

The dissolved inorganic carbon concentrations at the Palmachim site increase to around 10 mM (from 2mM at the sediment-water interface) with $\delta^{13}C_{DIC}$ of -52 ‰. The mass balance calculation suggests that the sharp decrease in the $\delta^{13}C_{DIC}$ within the pore fluid requires a source of dissolved inorganic carbon with a $\delta^{13}C$ between -73 to -67 ‰, which is close to the $\delta^{13}C_{CH4}$ that we measured (~ -70‰ in the deeper part of the Palmachim core —Figure 5.2g). This suggests that in the Palmachim sediments, the entire dissolved inorganic carbon pool within the pore fluids is produced from the oxidation of methane but the carbon isotopes don't support methanogenesis within this core section. Unfortunately, the dissolved inorganic carbon and $\delta^{13}C_{DIC}$ measurements are absent at Acre so I cannot calculate the isotope constraints on methane oxidation versus other organic molecules.

Another interesting feature that can be found at Acre is an increase in sulfate concentrations in the deeper part of the core. At this depth, where sulfate concentrations increase, we also note that the $\delta^{18}O_{SO4,}$ $\delta^{34}S_{SO4}$ and $\delta^{13}C_{CH4}$ decrease. This is possible due to the unique setting of this core (Figure 5.1). This core was taken

horizontally from a cliff. This unique setting, implies that there might be unique boundary conditions and seawater enveloping this black patch. Therefore, based on the geochemistry I hypothesize that the black patch from Acre is a horizontal, cylindrical-shape, localized, organic matter-rich feature.

At the shallower site Netanya (core PC-6), the sulfate profile shows a linear trend toward the sulfate-methane transition zone. Similar decreases have been observed in many profiles around the world and are interpreted that sulfate is reduced only by methane at the sulfate-methane transition zone rather than by other organic carbon compounds above (e.g. Niewöhner *et al*. 1998; Boetius *et al.* 2000; Aharon an Fu, 2000; Sivan *et al*. 2007; introduction to this thesis). Since this site is dominated by diffusion, looking at the dissolved inorganic carbon isotopic mass balance, similar to the calculation I did with Palmachin, in order to determine the source of the dissolved inorganic carbon will result in a bias toward the lighter isotope. In addition, at sites dominated by diffusion, it has been shown that carbon isotope equilibrium often occurs between the dissolved inorganic carbon and methane (Yoshinaga et al., 2014). Alternatively, by examining the stoichiometry of sulfate concentrations and the dissolved inorganic carbon it is possible to determine whether sulfate is reduced through AOM versus through organic matter (similar to the work in the estuaries in Chapter 4). The ratio between the depletion of sulfate and the increase in dissolved inorganic carbon plus the change in calcium, magnesium and strontium at site Netanya pore water is -1.1 (Fig 5.4). This stoichiometry is expected for sulfate-driven AOM, so I conclude that this is the dominant process at site PC-6. In summary, in all sites shallow and deep there is clear evidence that sulfate-driven AOM is the dominant process by which sulfate is being reduced.

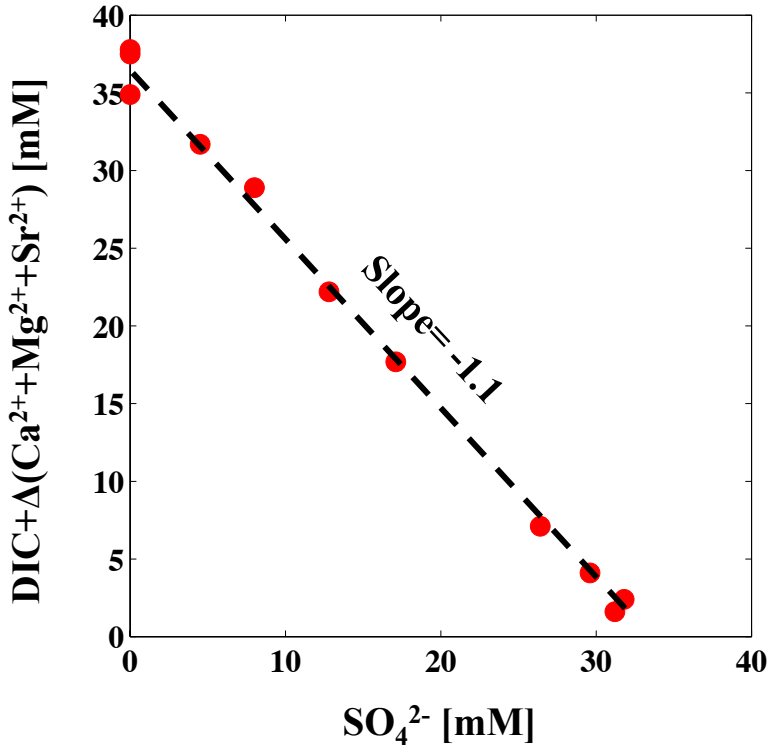

Figure 5.4: dissolved inorganic carbon (DIC) plus the change in calcium, magnesium and strontium vs. sulfate concentration from the Netanya (PC-6) pore water. The dashed line is the best-fit regression line.

5.3.2 Sulfur and oxygen isotope insight into the sulfate-methane coupling

The shape of the cross-plot between sulfur and oxygen isotopes in dissolved sulfate ($\delta^{18}O_{SO4}$ vs. $\delta^{34}S_{SO4}$) can be used to explore the way that sulfate is reduced during sulfate-driven AOM (e.g. Avrahamov et al., 2014; Deunser et al., 2014; Sivan et al., 2014). As I have explored throughout this thesis, when both sulfur and oxygen isotopes in sulfate are measured, they form a particularly useful tool to resolve the various redox changes of sulfur as it is transformed from sulfate to sulfide and back. Although both the sulfur and oxygen isotope composition of sulfate increases with depth at all sites, the relative change in the $\delta^{18}O_{SO4}$ versus $\delta^{34}S_{SO4}$ is unique at each site, hinting that the mechanism of sulfate reduction differs among the different sulfate-driven AOM zones (Figure 5.5). At the Palmachim and Acre sites very

moderate slopes are found in the $\delta^{18}O_{SO4}$ vs. $\delta^{34}S_{SO4}$ cross plot, 0.44±0.065 and 0.34±0.06, respectively. Given that this slope can vary between 0.27 and 10, I consider these two sites to be very similar and similar slopes can be found in other hydrocarbon seeps and estuaries where hydrocarbons are rich. At the PC-6 site, the slope between the $\delta^{18}O_{SO4}$ and $\delta^{34}S_{SO4}$ is much steeper than in Acre and Palmachim (1.7± 0.2), but becomes moderate at depth (Figure 5.5).

Similarly to what I explored in Chapter 4, it is helpful to put into context the $\delta^{18}O_{SO4}$ vs. $\delta^{34}S_{SO4}$ data of the three sites studied in this chapter with other $\delta^{18}O_{SO4}$ vs. $\delta^{34}S_{SO4}$ data from sites where sulfate-driven AOM was found. This will allow me to extend the discussion to the differences among tabulated data. I compare my data to two other published locations with sulfate-driven AOM. The first is Gulf of Mexico $\delta^{18}O_{SO4}$ vs. $\delta^{34}S_{SO4}$ isotopes data, that were taken from Ahaorn and Fu (2000) from a methane seep. The second is ODP site 1082 (Turchyn et al., 2006) located in the South West Atlantic that has a sulfate-methane transition zone at 25 meters below the sediment-water interface (Figure 5.5b).

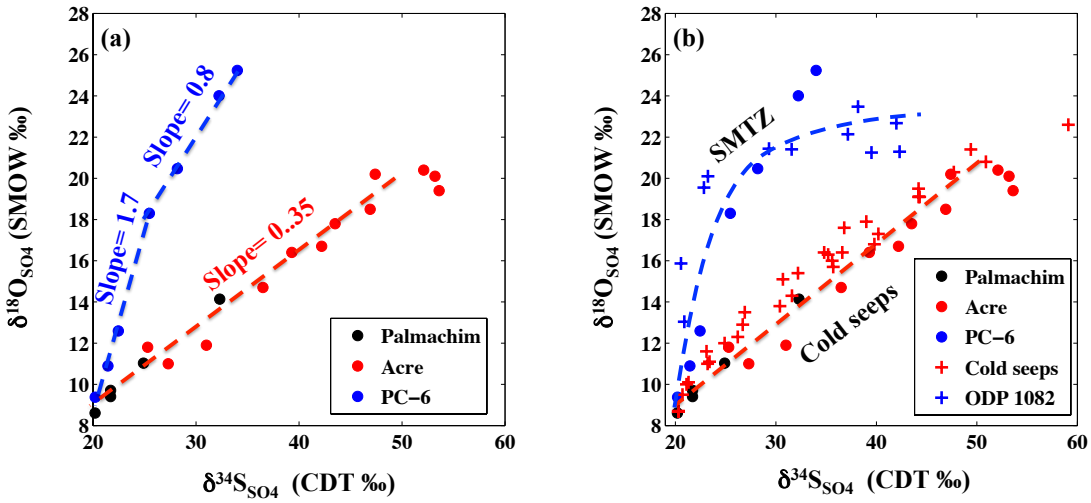

Figure 5.5: $\delta^{18}O_{SO4}$ vs. $\delta^{34}S_{SO4}$ from Palmachim, Arce and Netanya (PC-6) pore water sulfate. The lines are two-stages linear fit (a), and data from Organic-carbon poor deep-sea sediment (ODP 1082-- Turchyn et al., 2006) and cold seeps (Aharon and Fu 2000) (b). The dashed lines are schematic.

It has recently been discovered that there is back reaction of sulfide and dissolved inorganic carbon to sulfate and methane, respectively, during sulfate-driven AOM (Holler et al., 2011; Yoshinaga et al., 2014):

$$SO_4^{2-} + CH_4 \Longleftrightarrow HS^- + HCO_3^- + H_2O \quad (5.2)$$

Yoshinaga et al. (2014) showed that the rate of increase in the $\delta^{13}C_{CH4}$ below the sulfate-methane transition zone (called $\Delta\ \delta^{13}C_{CH4}$— Figure 5.6) is inversely correlated with the sulfate fluxes toward the sulfate-methane transition zone due to carbon isotopic equilibrium between $\delta^{13}C_{CH4}$ and $\delta^{13}C_{DIC}$. This isotope equilibrium happens because the reaction takes place close to thermodynamic equilibrium ($\Delta G \rightarrow 0$). This back reaction should promote isotopic equilibrium between sulfur in sulfate and sulfide as well as carbon in dissolved inorganic carbon and methane. Oxygen isotopes in sulfate will also be affected by this back reaction, since new oxygen atoms are being acquired during the reoxidation. Therefore, the back reaction will leave a mark on the $\delta^{18}O_{SO4}$ vs. $\delta^{34}S_{SO4}$ curve during sulfate driven AOM.

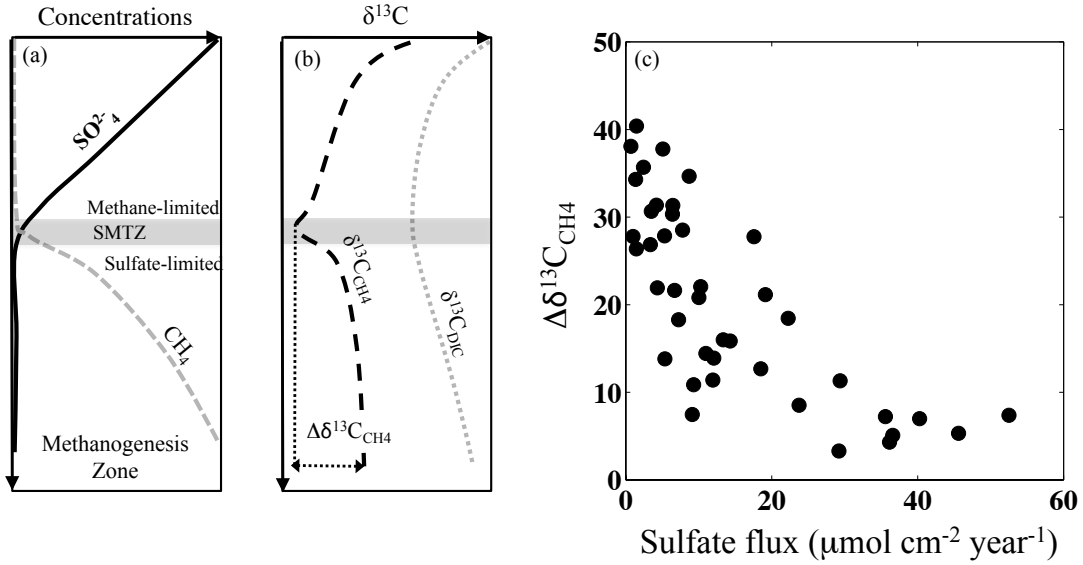

Figure 5.6: Schematic profiles of SO_4^{2-} and CH_4 concentrations (a), of CH_4 and DIC and the relationship between the carbon isotopic shift ($\Delta\ \delta^{13}C_{CH4}$) and sulfate flux. After Yoshinaga et al. (2014).

In order to assess the impact of sulfate supply on the sulfur vs. oxygen isotope slope in sulfate-driven AOM and in order to analyze what this tells us about the dynamic of sulfate-driven AOM, I will explore the relationship between the slope of the $\delta^{18}O_{SO4}$ vs. $\delta^{34}S_{SO4}$ curves and sulfate flux. The sulfate diffusive flux was calculated according to Fick's first law of diffusion:

$$J_{SO4}=-\varphi \cdot D_S \cdot \frac{d\left(SO_4^{2-}\right)}{dZ} \quad (5.3)$$

where φ is the porosity, D_s is the effective diffusion coefficient in the sediment and $d(SO_4^{2-})/dz$ is the one-dimensional sulfate concentration gradient. The molecular diffusion coefficient for sulfate in seawater (D_0) was calculated based on Donahue et al. (2008):

$$D_0=(4.655+0.2125 \cdot T) \cdot 10^{-6} \quad (5.4)$$

where D_0 is the molecular diffusion coefficient of sulfate ($cm^2\ sec^{-1}$) and T is the temperature (ºK). The assumption that $Ds=D_0 \cdot \phi^2$ (Berner et al., 1980) was used for estimating the effect of tortuosity.

Figure 5.7 shows the slope of $\delta^{18}O_{SO4}$ vs. $\delta^{34}S_{SO4}$ plot vs. the calculated sulfate flux from sites where sulfate-driven AOM was detected; the three reported in this chapter, and several from the literature. It can be seen that this plot can be divided in two sections. At large sulfate fluxes the $\delta^{18}O_{SO4}$ vs. $\delta^{34}S_{SO4}$ slope does not change significantly as a function of the flux of sulfate and the slopes clusters around 0.3 to 0.45; as explored in Chapter 2, this implies sulfur and oxygen isotopes are impacted only by kinetic isotope fractionation. At low sulfate fluxes, the slopes are larger and negatively correlated with the increasing flux. It is important to note that the high fluxes comprise sites where an excess of methane was found, such as cold seeps and estuaries, whereas the latter represents sites where distinct deeper sulfate-methane transition zones were observed. This implies that the relationship between the supply of sulfate and the back reaction during sulfate-driven AOM is more complex then previously assumed.

To investigate further the correlation between the slope of the $\delta^{18}O_{SO4}$ vs. $\delta^{34}S_{SO4}$ cross-plot and the sulfate flux from marine sediments, I calculated this slope from two published experiments where sulfate-driven AOM was done in the laboratory. Figure 5.8 shows the calculated slope versus the methane concentration in these experiments. It can be seen that the correlation between the slope and sulfate flux in the natural environment is the same as this correlation versus methane concentration in laboratory experiments, but also the lower limit of this slope is similar (~0.35±0.1). Overall, these results indicate that the slope on the $\delta^{18}O_{SO4}$ vs. $\delta^{34}S_{SO4}$ cross-plot is fundamentally a function of the methane concentration/supply, which in marine sediments control the sulfate flux from the overlying ocean into the sediments. In cases where methane is in excess, the $\delta^{18}O_{SO4}$ vs. $\delta^{34}S_{SO4}$ results in a close to linear behaviour with very moderate slope.

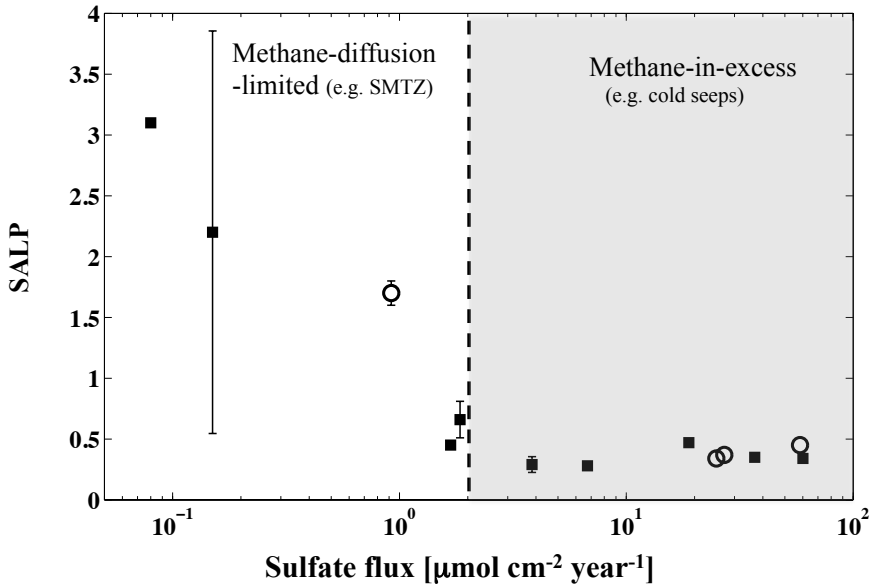

Figure 5.7: The slope on $\delta^{18}O_{SO4}$ vs. $\delta^{34}S_{SO4}$ plot (SALP) vs. the calculated sulfate flux from different sites. Closed symbols data from the literature, open symbols, sites from this study. The grey area includes sites where methane is in excess and the white area sites with sharp sulfate methane transition zone.

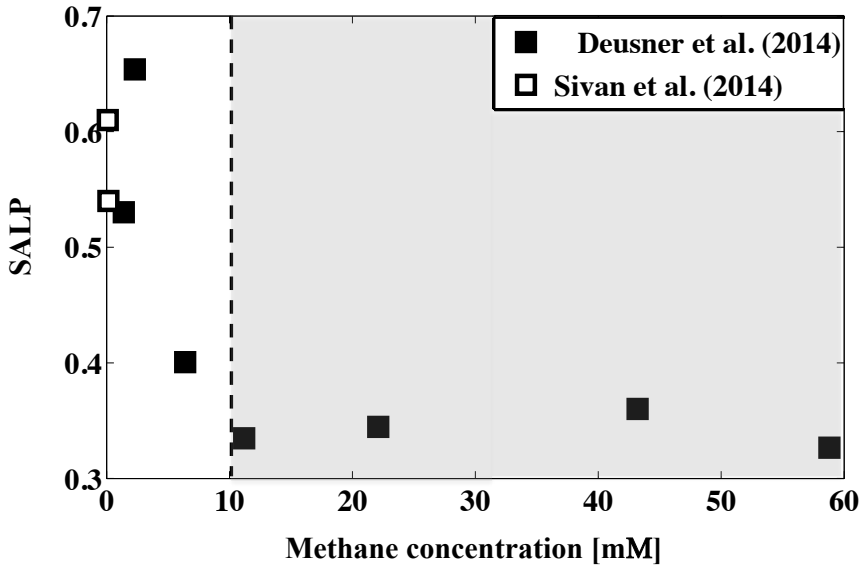

Figure 5.8: The slope on $\delta^{18}O_{SO4}$ vs. $\delta^{34}S_{SO4}$ plot (SALP) vs. methane concentration from laboratory experiments. Open symbols- data from Sivan et al. (2014), closed symbols- data from Deunser et al. (2014).

5.3.3 A sensitivity analysis for oxygen and sulfur isotopes in sulfate during sulfate-driven AOM

The strong correlation between $\delta^{18}O_{SO4}$ and $\delta^{34}S_{SO4}$ during sulfate-driven AOM at 'methane-in-excess' environments can explain by a process that impacts sulfur and oxygen isotopes in a similar manner. One possibility would be mixing between two end-members with different $\delta^{18}O_{SO4}$ and $\delta^{34}S_{SO4}$. However, because of the variety of settings studied, where the temperature, water pressure, salinity and sulfate concentration range significantly, it is difficult to invoke binary mixing to explain this data. This is also supported by the reactive-transport model developed in Chapter 2, which found that the physical parameters in the natural environment play only a secondary role in shaping the slope in $\delta^{18}O_{SO4}$ versus $\delta^{34}S_{SO4}$ space. This suggests that this unique isotope correlation is, ultimately, inert to the physical conditions that dominate mixing in any particular environment.

One way to produce a linear relationship between $\delta^{18}O_{SO4}$ and $\delta^{34}S_{SO4}$ is through Rayleigh-style distillation, where a kinetic isotope effect impacts both $\delta^{18}O_{SO4}$ and $\delta^{34}S_{SO4}$ as sulfate is consumed; in this case, the $\delta^{18}O_{SO4}$ less reflects any oxygen isotope equilibration with water. This distillation pattern would require negligible reoxidation of sulfur intermediates, since any reoxidation incorporates external oxygen atoms in the resulting sulfate. It was recently suggested for methane oxidation by ANME-2 from cold-seep environments that one of every eight (~12%) of the reduced sulfur intermediates formed is reoxidized back to sulfate through disproportionation of polysulfide intermediates (Milucka et al., 2012, Holler et al., 2011). I will now use numerical model to estimate the impact of this level of reoxidation on the slope between $\delta^{18}O_{SO4}$ and $\delta^{34}S_{SO4}$.

In order to understand the relative evolution of sulfur and oxygen isotopes in sulfate during sulfate-driven AOM, I derive a basic numerical model based on the enzymatic model proposed by Milucka et al. (2012). In the Milucka et al. (2012) enzymatic model, methane oxidation and sulfate reduction to elemental sulfur (or all the way to sulfide) is performed by methanotrophic archaea alone (ANME). Zero-valent sulfur then reacts with sulfide to form disulphide, which subsequently disproportionates into sulfate and sulfide. For each eight-sulfate molecules that are brought into the cell, one recycles back to sulfate during this disulfide disproportionation and the other seven molecules are reduced to sulfide.

Some of the specifics of this enzymatic model remain enigmatic which presents challenges for my numerical approach to the problem. For example, both sulfur and oxygen isotopes are partitioned during the various enzymatic steps with unknown kinetic and equilibrium fractionation factors. Here, I perform a carful sensitivity analysis, in order to deal with this uncertainty. The assumptions in my model include (summarized in Figure 5.9):

1) The kinetic isotope fractionation between sulfate and zero-valent sulfur is 25±10 ‰ (Rees, 1973)
2) The kinetic oxygen isotopic fractionation is equal to 25% of the sulfur isotopic fractionation between sulfate and zero-valent sulfur (Mizutani, Y. and Rafter 1969; See also Chapter 2 and Chapter 3).

3) The kinetic isotope fractionation between zero-valent sulfur and sulfide is 25±10 ‰ (Rees, 1973).
4) The isotopic composition of the disulfide was taken as the average value between zero-valent sulfur and sulfide. This is since each one of them contributes the same number of sulfur atoms to the resulting disulfide.
5) The sulfur isotopic fractionation between disulfide and sulfate is 15±15 ‰ (Böttcher et al., 2001).
6) The sulfur isotopic fractionation between disulfide and sulfide is -5±5 ‰ (Böttcher et al., 2001).
7) The result $\delta^{18}O_{SO4}$ during disulfide disproportionation is 20±5 ‰ (Böttcher et al., 2001).

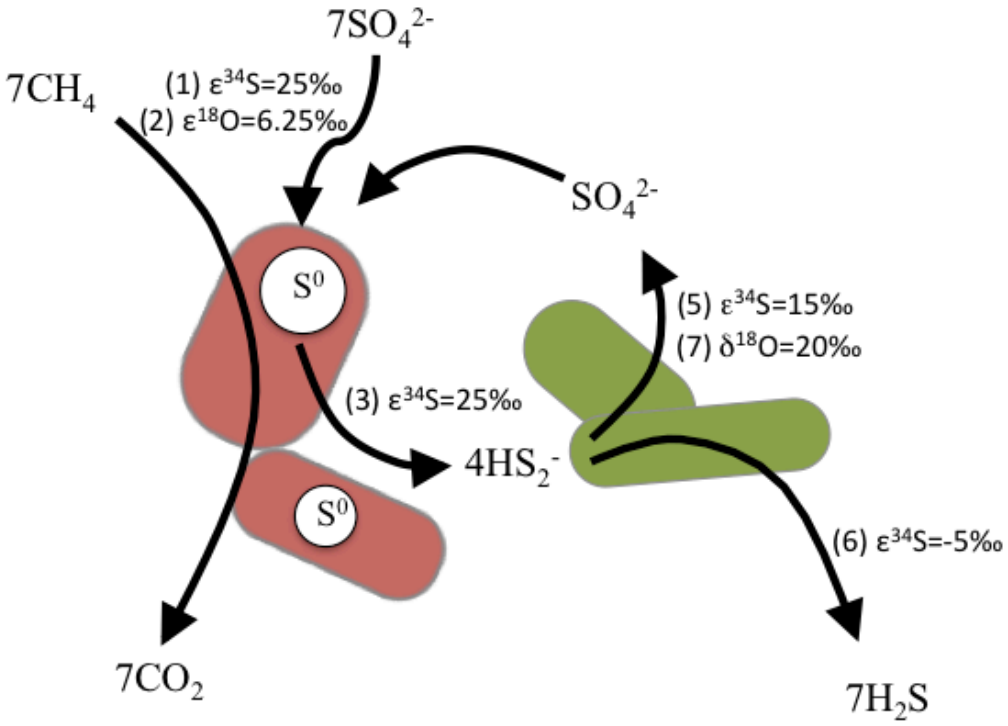

Figure 5.9: Sulfur pathway during sulfate-driven AOM (After Milucka et al., 2012) and the isotopic fractionation associated with each of the steps.

Figure 5.10 summaries all the possible solutions for $\delta^{18}O_{SO4}$ vs. $\delta^{34}S_{SO4}$ within the uncertainties of my assumptions. The result for the model suggests that even with these unknowns, all the solutions have a near linear relationship with a slope that varies between 0.24 and 0.4. If I consider only the primary values, my model

suggests that if more than 40% of the sulfate entering the cell is reoxidized, it will impact the slope between $\delta^{18}O_{SO4}$ vs. $\delta^{34}S_{SO4}$ such that the slope is higher than 0.4 (Figure 5.11). My data is therefore consistent with the level of intermediate-sulfur oxidation postulated in the Milucka et al (2012) model for sulfate-driven AOM.

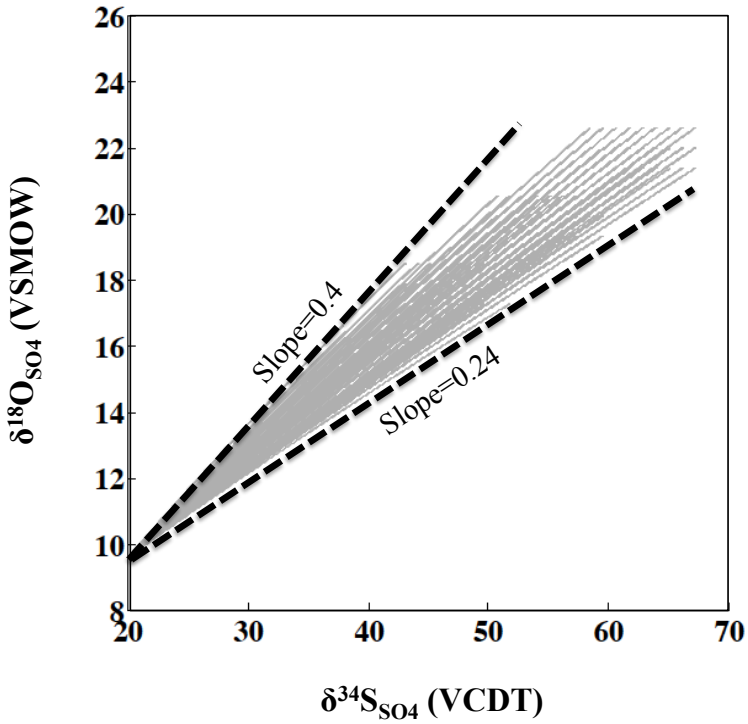

Figure 5.10: The $\delta^{18}O_{SO4}$ vs. $\delta^{34}S_{SO4}$ results from the proposed model. Each of the grey lines represent a solution based on the different combination of the isotope fractionation of sulfur and oxygen isotopes at each step. Dashed lines are the envelope of all the possible solutions within the proposed uncertainty.

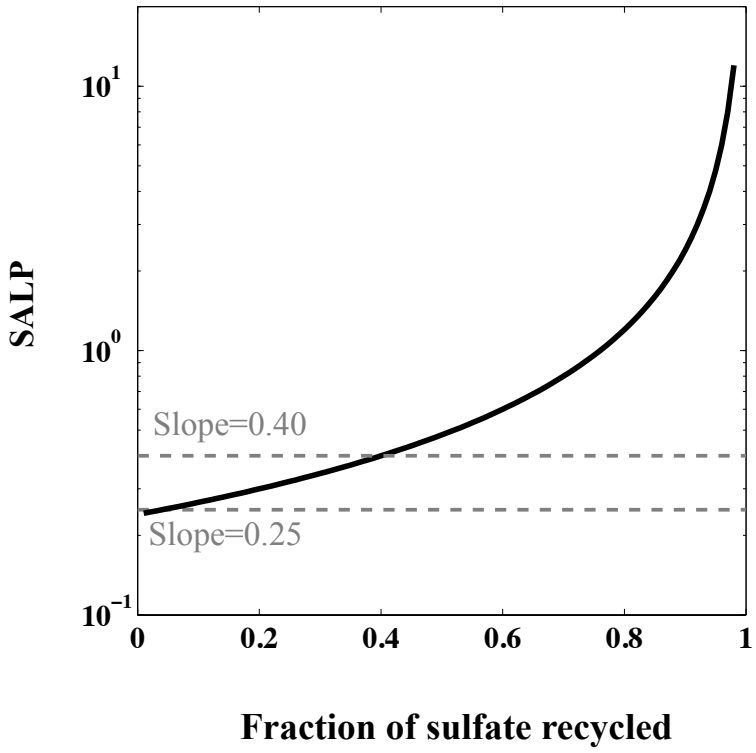

Figure 5.11: The change in the slope of $\delta^{18}O_{SO4}$ vs. $\delta^{34}S_{SO4}$ (SALP) as a function of the fraction of sulfate recycled.

As we understand that the process of sulfate-driven AOM operates close to thermodynamic equilibrium (e.g. Holler et al., 2011), the degree of back reaction is highly dependent on the concentration of the reactant. Therefore, if the concentrations of methane and sulfate are high, there should be a decreasing and even negligible percentage of back reaction. In methane seeps, methane is transported in the form of bubbles, keeping the dissolved methane concentration close to saturation. The methane flux is so high that an exceedingly small fraction of intermediate valence state sulfur is reoxidized or recycled. Hence, the fractionation of both sulfur and oxygen isotopes in dissolved sulfate will be the fractionation during the reduction of sulfate to sulfide. At locations where there is a sulfate-methane transition zone the methane supply is low there is much more back reaction of sulfide to sulfate which results in a steep $\delta^{18}O_{SO4}$ vs. $\delta^{34}S_{SO4}$ slope and eventually the oxygen isotopes reach equilibrium (see Figure 5.12 for summary). Here I suggest that there is a threshold of

methane supply; where methane supply is higher than this threshold, this out-competes the sulfate transport and we see bubbles. Where the methane flux is low, this is equalized by the sulfate flux and a constant slope emerges.

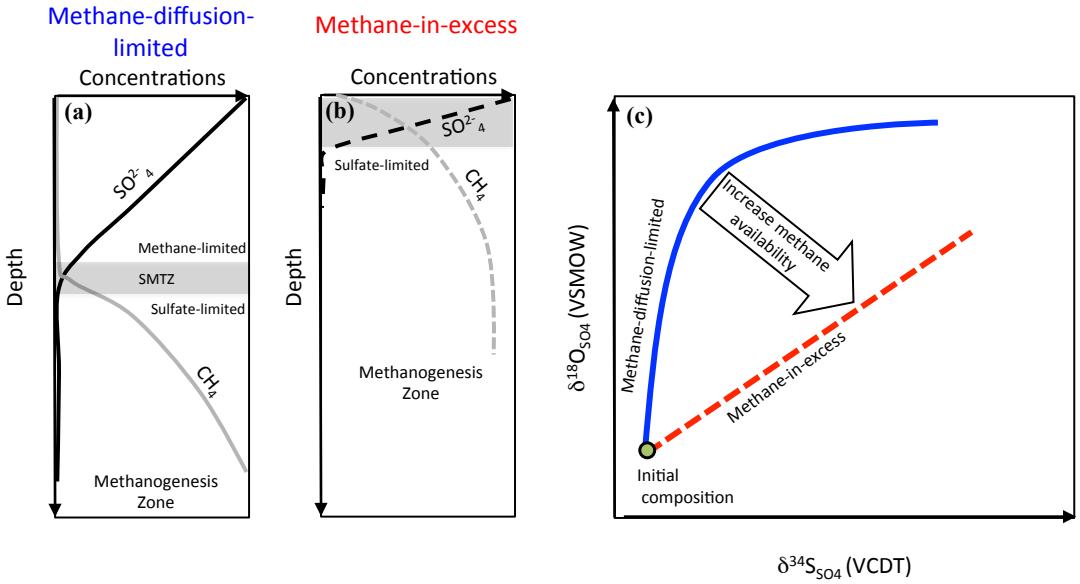

Figure 5.12: Schematic chemical profiles of methane-diffusion-limited (a) methane-in-excess environments (b) and the respective curve of $\delta^{18}O_{SO4}$ vs. $\delta^{34}S_{SO4}$ (c). the grey area represent the sulfate-driven AOM zone.

5.4 Summary

In this chapter I presented pore fluids results from three different sites at the South-Eastern Mediterranean. In all sites, evidence for methanogenesis and sulfate-driven anaerobic methane oxidation were found to be the dominant process. However, the cross-plot between $\delta^{18}O_{SO4}$ and $\delta^{34}S_{SO4}$ of the pore fluid sulfate reveals that a pattern emerges in shallow core PC-6, where a sharp sulfate-methane transition zone was found, versus the deep sites Palmachim and Arce, which are cold methane seeps. I later demonstrated that this different pattern is indicative of the type of environment and specifically related to the flux of methane. This slope emerges because when methane is in excess, both sulfur and oxygen isotopes are affected only by kinetic fractionation, but when methane is less abundant there is more back reaction of sulfide which results in a decoupling between sulfur and oxygen isotopes in dissolved

sulfate. I suggest here that although the net reaction is similar in gas seeps and SMTZ, they represent two different environments and cannot longer be treated in the same manner. In the next chapter I will explore the applications of this unique isotopic fingerprint in methane seeps.

Chapter 6

Perspective: a unique isotopic fingerprint during sulfate-driven anaerobic oxidation of methane

The transient release of biogenic or thermogenic methane from sedimentary or other subsurface environments has the potential to greatly impact global climate because methane is a strong greenhouse gas (MacDonald, 1990). Catastrophic release of methane from marine sediments has been invoked to explain transient climate perturbations throughout Earth history, most notably the Paleocene-Eocene Thermal Maximum, 55 million years ago (Dickens et al., 1995). Today, the majority of methane produced within the subsurface, however, will be oxidized within the subsurface or near the sediment-water interface (Reeburgh, 2007).

In this thesis, I demonstrated that much information can be gained by cross plotting $\delta^{18}O_{SO4}$ versus $\delta^{34}S_{SO4}$ during the onset of microbial sulfate reduction, as both isotopes are initially evolving to heavier values in a close-to-linear manner before isotope equilibrium for $\delta^{18}O_{SO4}$ is reached. The slope of this isotope-enrichment phase relates to the rate of sulfate reduction, where faster rates of sulfate reduction result in the $\delta^{34}S_{SO4}$ increasing more rapidly than the $\delta^{18}O_{SO4}$ (a shallower slope), while slower rates of microbial sulfate reduction result in the $\delta^{18}O_{SO4}$ increasing more rapidly than the $\delta^{34}S_{SO4}$ (a steeper slope – Chapter 3, see also Böttcher et al., 2008; Aharon and Fu, 2000; Antler et al., 2013). I interpreted this relationship as an increase in the reoxidation of sulfur intermediates when the rate of sulfate reduction decreases and while this relationship is broadly accepted, the specifics need refinement. For example, in Chapter 4, I found that under nearly-identical rates of

microbial sulfate reduction, organoclastic microbial sulfate reduction and sulfate-driven AOM result in markedly different slopes between $\delta^{18}O_{SO4}$ and $\delta^{34}S_{SO4}$. In this chapter, I will demonstrate for the first time that the slope between $\delta^{18}O_{SO4}$ and $\delta^{34}S_{SO4}$ has a unique value when sulfate reduction is coupled to methane oxidation in 'methane-in-excess' environments – such as cold seeps - versus when sulfate-driven AOM is occurring in 'methane-diffusion-limited' environments (where there is a sharp sulfate-methane transition zone), or during organoclastic microbial sulfate reduction.

The sites that I presented in this thesis can be sort into three types of environments: 1) 'methane-in-excess' environments where methane exists in bubbles, 2) 'methane-diffusion-limited' environments where sulfate and methane do not coexist, and 3) 'methane-devoid' or organoclastic microbial sulfate reduction, environments where sulfate-driven AOM is not the dominant process:

1) The Yarqon estuary is the largest coastal river in Israel, and contains high organic carbon load and almost seawater salinity and high methane concentrations (up to 2mM – 'methane-in-excess') (Chapter 4).

2) The 'Black patch' was discovered during 2011 *Nautil*us E/V field season in front the cost of Arce (Israel) inside a pockmarked field. The black patch and has cylindrical symmetry and high methane concentrations (up to 1.5 mM – 'methane-in-excess ') (Chapter 5).

3) The Palmachim 'Gas seep' was sampled at the 'Palmachim disturbance' offshore Israel at water depth of 1134 m, and has visible methane gas bubbling ('methane-in-excess') (Chapter 5).

4) The Qishon estuary drainage area occupies 1100 km^2, with intensive agricultural activity and industry taking place within the basin and dominates by organoclastic sulfate reduction (Chapter 4).

5) The Southeastern Mediterranean shelf (Site PC6- Netanya- Israel). This site shows a distinct sulfate-methane transition zone at depth of 3.6 m (Chapter 5) suggesting that 'methane-diffusion-limited' sulfate-driven AOM.

The slope of the $\delta^{18}O_{SO4}$ versus $\delta^{34}S_{SO4}$ cross-plots from the 'methane-in-excess' environments, fall into a narrow range compared to the data collected from 'methane-diffusion-limited' and organoclastic -sulfate reduction environments (Figure 6.1). The unique slope in the $\delta^{18}O_{SO4}$ versus $\delta^{34}S_{SO4}$ data in 'methane-in-excess' environments is 0.37 ± 0.01 (95% confidence interval). The significance of this data set is shown in Figure 6.2, where a wider compilation of $\delta^{18}O_{SO4}$ and $\delta^{34}S_{SO4}$ data from the literature is presented along with the data from my thesis. The slope in each environment was calculated as the linear regression of the tangent on a $\delta^{18}O_{SO4}$ versus $\delta^{34}S_{SO4}$ cross-plot near the axis (I exclude sites with poor statistics-- $R^2<0.85$ and $n<3$). It can be seen that the slope of $\delta^{18}O_{SO4}$ versus $\delta^{34}S_{SO4}$ in methane seep environments aggregates around the slope in $\delta^{18}O_{SO4}$ versus $\delta^{34}S_{SO4}$ space from Figure 6.1. The locations with 'organoclastic sulfate-reduction' or 'methane-diffusion-limited' have a slope that varies significantly (Figure 6.2).

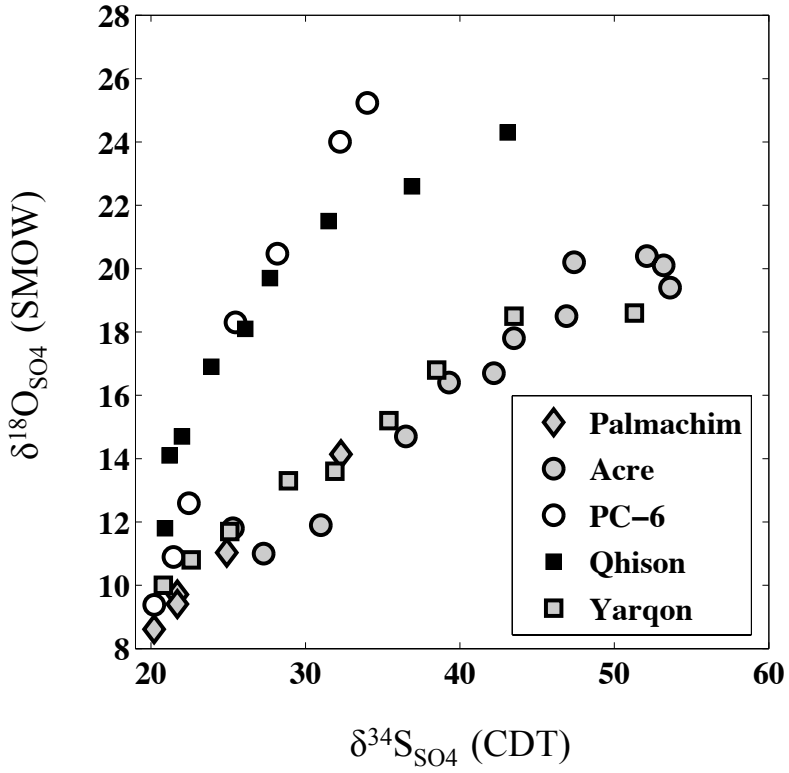

Figure 6.1: The $\delta^{18}O_{SO4}$ versus $\delta^{34}S_{SO4}$ data from methane-in-excess (gray symbols), methane-diffusion-limited (open symbols) and organoclastic sulfate reduction (closed symbols).

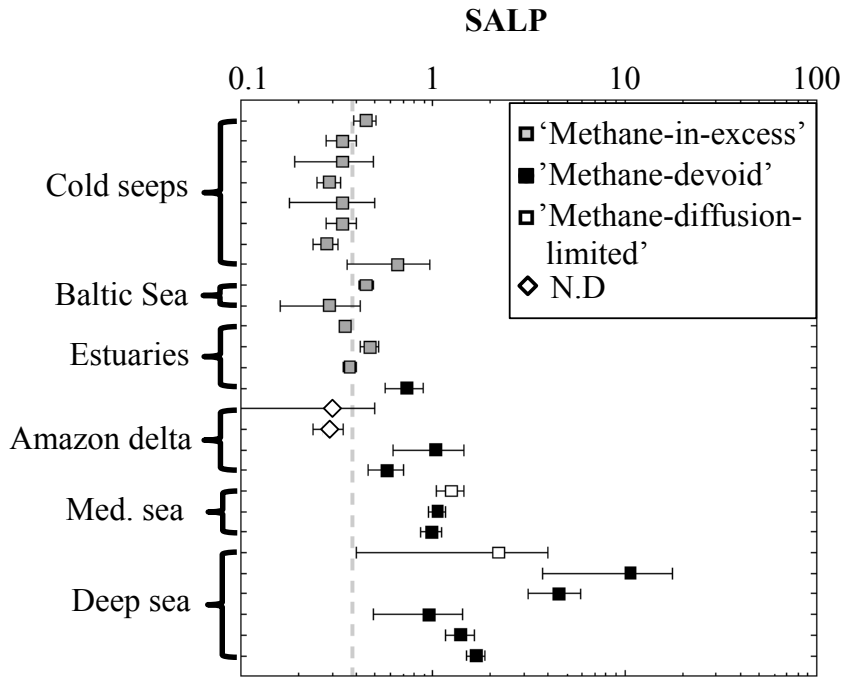

Figure 6. 2: The slope of the $\delta^{18}O_{SO4}$ versus $\delta^{34}S_{SO4}$ cross-plot (SALP) compiled from different environments. 'N.D'- sites where methane measurements are not available. The dashed line is the average slope of all the 'methane-in-excess' sites. Error bars represent a 95% confidence interval. Complete lists of references and data are available in table A.4.4.1.

The strong correlation between $\delta^{18}O_{SO4}$ and $\delta^{34}S_{SO4}$ during sulfate-driven AOM at 'methane-in-excess' environments can be explained by a process that impacts sulfur and oxygen isotopes in a similar manner. One possibility would be mixing between two end-members with different $\delta^{18}O_{SO4}$ and $\delta^{34}S_{SO4}$. However, because of the variety of settings studied, where the temperature, water pressure, salinity and sulfate concentration range significantly, it is difficult to invoke binary mixing to explain this data. This is also supported by a reactive-transport model, formulated by Antler et al. (2013) and introduced in Chapter 2, which found that the physical parameters in the natural environment play only a secondary role in shaping the slope in $\delta^{18}O_{SO4}$ versus $\delta^{34}S_{SO4}$ space. This suggests that this unique isotope correlation is, ultimately, inert to the physical conditions that dominate mixing in any particular environment.

In Chapter 5 I demonstrated that one way to produce a linear relationship between $\delta^{18}O_{SO4}$ and $\delta^{34}S_{SO4}$ is through Rayleigh-style distillation, where a kinetic isotope effect impacts both $\delta^{18}O_{SO4}$ and $\delta^{34}S_{SO4}$ as sulfate is consumed. In that chapter, the results for my sensitivity analysis among the range of possible enzymatic isotope fractionations demonstrated that all solutions with negligible reoxidation (12%) have a near linear relationship with a slope that varies between 0.24 and 0.4. In addition, my model suggests that up to 40% of the intracellular sulfur could be reoxidized before the slope distinct from the natural range in the slope in 'methane-in-excess' environments.

In environments with 'methane-diffusion-limited' sulfate-driven AOM, the $\delta^{18}O_{SO4}$ versus $\delta^{34}S_{SO4}$ cross-plot can deviate from the unique slope found in 'methane-in-excess' environments. This more rapid increase of $\delta^{18}O_{SO4}$ versus $\delta^{34}S_{SO4}$ is due to a larger impact of oxygen isotope equilibrium between sulfur intermediates and water and a subsequent reoxidation of these sulfur intermediates impacting the extracellular $\delta^{18}O_{SO4}$ (e.g., Brunner et al., 2005). In these 'methane-diffusion-limited' environments, methane concentrations are lower and the microbial reaction approaches thermodynamic equilibrium, which means increased back reaction of intermediate-sulfur species to sulfate (Holler et al., 2011; Yoshinaga et al., 2014). It was recently suggested that enzymatic reversibility in sulfate-driven AOM is a function of the methane flux, where high methane flux correlates with low reversibility (Yoshinaga et al., 2014); my results support this conclusion. At 'methane-in-excess' environments, the methane flux is so high that an exceedingly small fraction of intermediate valence state sulfur is reoxidized or recycled. This ultimately results in a unique isotopic signature of $\delta^{18}O_{SO4}$ versus $d^{34}S_{SO4}$ in these environments that can be used to distinguish between 'methane-in-excess' and 'methane-diffusion-limited' environments.

Cold methane seeps are often accompanied by carbonate precipitation as well as other authigenic minerals such as barite (e.g., Fu et al., 1994). This is because anaerobic methane oxidation leads to an increase in pH and alkalinity. These authigenic minerals can fossilize; carbonate accretions are found throughout the

geological record (e.g., Jiang et al., 2003; Kiel, 2015), often containing exceptionally ^{13}C depleted carbonate highly suggestive of the methane source (e.g., Peckmann and Thiel, 2004). However, ^{13}C-depleted carbonate, produced from methane oxidation, does not distinguish the paleoenvironment of methane consumption or its link to microbial sulfate reduction. It was previously suggested that the $\delta^{18}O_{SO4}$ and $\delta^{34}S_{SO4}$ in barite can be used to identify fossilized methane seeps (Johnson et al., 2004). I have compiled the $\delta^{18}O_{SO4}$ and $\delta^{34}S_{SO4}$ from barite found in recent methane seeps and plot these data with pore fluid $\delta^{18}O_{SO4}$ and $\delta^{34}S_{SO4}$ from modern 'methane-in-excess' environments (Figure 6.3). The barite sulfur and oxygen isotope measurements fall within the envelope created by modern pore fluid $\delta^{18}O_{SO4}$ and $\delta^{34}S_{SO4}$ data. This suggests that the unique isotopic fingerprint that I found in pore fluid $\delta^{18}O_{SO4}$ and $\delta^{34}S_{SO4}$ (Figure 6.1) has the potential to be preserved in the geological record and as new tool for identifying fossilised ancient methane seeps. Since this isotopic fingerprint is expressed as a linear line, the strength of my finding is that the slope does not depend on the initial isotopic composition but on the relationship among the various data points.

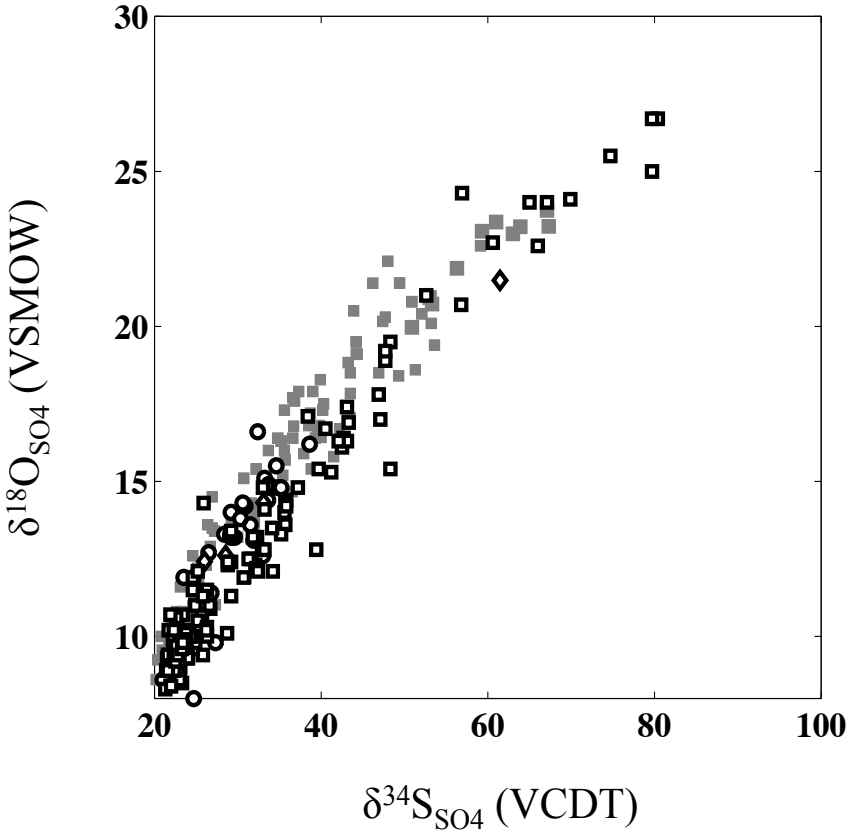

Figure 6.3: The $\delta^{18}O_{SO4}$ versus $\delta^{34}S_{SO4}$ data from cold methane seeps and seeps analogues (gray) and barite deposits associated with cold methane seeps (open symbols) from the Gulf of Mexico (Rhombus–Fu and Aharon, 1997, Squares–Feng and Roberts, 2011) and from the Sea of Okhotsk (Circles–Greniert et al., 2002).

Conclusions

My data compilation and sensitivity analysis (see chapter 5) demonstrates that there is a lower limit to the slope between $\delta^{18}O_{SO4}$ and $\delta^{34}S_{SO4}$ during the onset of microbial sulfate reduction, which results in a distinct isotopic signature in environments where methane is in excess. This distinct isotopic signature likely results from negligible reoxidation of sulfur species when the electron donor is abundant. In addition, a change in the microbial community structure between 'methane-in-excess' and 'methane-diffusion-limited' environment is possible since different anaerobic methanotrophs thrive under different supplies of methane. I

therefore suggest that the sulfur and oxygen isotopes in dissolved sulfate can be used to track the relationship between methane and sulfate both in modern marine sediments and in the geological record. This appears to be a robust tool as it scales across many environments with different depositional settings.

I suggest that sulfur and oxygen isotope in dissolved sulfate can be used to track the relationship between methane and sulfate in marine sediments and in the geological record. This seems to be robust tool as it scales across many environments with different depositional settings. Measurements from barite deposits associated with methane seeps demonstrate that this unique isotopic signature found in pore fluid sulfate is potentially preserved. Diagenetic barite is often found in marine sediments and rocks and has a diagnostic pitted texture compared with biogenic barite (Paytan et al., 2002); typically this barite is not analysed isotopically because it acquires a subsurface isotope signature so is less useful for paleoceanographic reconstruction of the biogeochemical sulfur cycle. The logical follow up study could analyse these diagenetic barites or authigenic carbonate from the Cenozoic and late Cretaceous to assess the nature of methane fluxes in certain locations over geological time. The preservation potential of this signal is high as these minerals are usually part of large lithological build-ups associated with methane seeps. In addition, it is easy to test if the minerals hold the original isotope signal. For instance, barite that precipitates during sulfate-driven AOM has a typical morphology and SEM images may reveals if the barite has been grown diagenetically (Greinerta et al., 2012). As for carbonate-associated-sulfate, any reprecipitation of carbonates will also affect the $\delta^{13}C$ of the carbonate and since the original $\delta^{13}C$ is extremely depleted it is easy to estimate if there is any alteration of the original signal. A second possibility would be to analyse authigenic carbonate or diagenetic barite across intervals where methane seeps have been invoked to cause transient climate perturbations. For example, could a fingerprint of the hypothesized North Atlantic methane leak proposed to cause the Paleocene-Eocene Thermal maximum (Chun et al., 2010) be found in the geological record?

Summary

Isotope partitioning and the relative reversibilities of several enzymatic steps during microbial sulfate reduction (MSR) and sulfate-driven anaerobic oxidation of methane (AOM) influence the measured isotopes ratios of $^{33}S/^{32}S$, $^{34}S/^{32}S$ and $^{18}O/^{16}O$ in the residual sulfate as MSR proceeds. Previous studies have shown that the availability and type of organic substrate consumed during MSR control the magnitude of the isotope fractionation between ^{34}S and ^{33}S versus ^{32}S, but the influence of the electron donor on the fractionation of oxygen isotopes is less well understood. In this Thesis I further our understanding of microbial sulfur metabolism with particular focus on the organic matter type and availability through pure culture experiments and studies in the natural environment.

First I explored the combined multiple sulfur ($^{33}S/^{32}S$, $^{34}S/^{32}S$) and oxygen ($^{18}O/^{16}O$) isotope fractionation in pure cultures of a marine *Desulfovibrio* sp. DMSS-1 grown on different organic substrates. The use of the coupled oxygen and major and minor sulfur isotopes allows me to resolve more than two enzymatic branch points with in the microbial cells during MSR. My measurements show that the isotope fractionation of both oxygen and major and minor sulfur isotopes correlate with the cell-specific rate of MSR, with faster reduction rates producing smaller isotopic fractionation for all isotopes. This relationship indicates that more intracellular sulfur intermediates may be reoxidized when the flux of electrons from the electron donor is low. The use of multiple isotopes allowed me to conclude that not only does the isotope fractionation change as a function of the cell-specific sulfate reduction rate, the isotope fractionation also changes with the degree of reversibility of each step during MSR. I suggested that in environmental settings where the availability of the electron donor can change dramatically there may be more changes in the microbial mechanism of MSR that can be more pronounced.

I then used multiple stable isotope measurements in two highly stratified estuaries located along the Mediterranean coast of Israel (the Yarqon and the Qishon)

to explore the consumption of sulfate through sulfate-driven AOM versus organoclastic MSR. At both sites, pore fluid sulfate is rapidly consumed within the upper 15-20 cm. Although the pore fluid sulfate and dissolved inorganic carbon (DIC) concentration profiles change over a similar range with respect to depth, the sulfur and oxygen isotopes in the pore fluid sulfate and the carbon isotopes in the pore fluid DIC are fundamentally different. This pore fluid isotope geochemistry indicates that the microbial mechanism of sulfate reduction differs between the studied sites. I suggested that in the Yarqon estuary, sulfate is consumed entirely through AOM, whereas in the Qishon, both AOM and bacterial sulfate reduction through organic matter oxidation coexist. These results have implications for understanding the microbial mechanisms behind sulfate-driven AOM. In addition, I compiled data from marine and marginal marine environments that supports my conclusion that the intracellular pathways of sulfate reduction varies among environments with sulfate-driven AOM.

In the next chapter I explored sulfate-driven AOM in two environments from the three different sites in the southeastern Mediterranean. Methane can be transported within the pore space of marine sediments either via diffusion or as bubbles. When methane travels in bubbles, these bubbles often escape complete oxidation and reach the overlying water where the methane emerges from the sediment in "cold" seeps. In these three sites in the southeastern Mediterranean methane is seeping from two sites but transported by diffusion at the other. My analyses demonstrated strong correlation between the slope on a plot of $\delta^{18}O_{SO4}$ vs. $\delta^{34}S_{SO4}$ and the flux of sulfate; the flux of sulfate at these sites is linked to the transport dynamics of methane. In addition, at high fluxes of sulfate, particularly at the sites where methane is seeping or 'in excess', I founded that there is a lower limit of the slope between $\delta^{18}O_{SO4}$ and $\delta^{34}S_{SO4}$ that results in what I called a distinct isotopic signature. My numerical model results suggest that this distinct isotopic signature likely results from negligible reoxidation of sulfur species when the electron donor is abundant. In addition, a change in the microbial community structure between 'methane-in-excess' and 'methane-diffusion-limited' environment is possible since different anaerobic methanotrophs thrive under different supplies of methane.

Finally, I summarized the thesis by demonstrating that by using the sulfur and oxygen isotope composition of sulfate, a unique isotopic signature emerges during microbial sulfate reduction coupled to methane oxidation in all measured bubbling cold seeps. This isotope signature differs to that when sulfate is reduced by either organic matter oxidation or by the slower, diffusive flux of methane within marine sediments. I also showed through a comparison with the literature data, that this unique isotope fingerprint is preserved in the rock record in authigenic build-ups of barite associated with methane cold seeps. I therefore suggested that the sulfur and oxygen isotopes in dissolved sulfate can be used to track the relationship between methane and sulfate both in modern marine sediments and in the geological record. This appears to be a robust tool as it scales across many environments with different depositional settings.

References

Aharon P. and Fu B. (2000) Microbial sulfate reduction rates and sulfur and oxygen isotope fractionations at oil and gas seeps in deepwater Gulf of Mexico. Geochim. Cosmochim. Acta 64(2), 233–246.

Aharon P. and Fu B. (2003) Sulfur and oxygen isotopes of coeval sulfate–sulfide in pore fluids of cold seep sediments with sharp redox gradients. Chem. Geol. 195, 201-218.

Aller R. C., Madrid V., Chistoserdov A., Aller J. Y. and Heilbrun C. (2010) Unsteady diagenetic processes and sulfur biogeochemistry in tropical deltaic muds: Implications for oceanic isotope cycles and the sedimentary record. Geochim. Cosmochim. Acta 74, 4671-4692.

Aller R.C., (2004) Conceptual models of early diagenetic processes: the muddy seafloor as an unsteady, batch reactor. J. Mar. Res 62, 815-835

Alperin, M. J., Reeburgh, W. S., and Whiticar, M. J. (1988). Carbon and hydrogen isotope fractionation resulting from anaerobic methane oxidation. Glob. Biogeochem. Cycles, 2(3), 279–288.

Antler, G., Turchyn, A.V., Rennie, V., Herut, B., and Sivan, O., (2013), Coupled sulfur and oxygen isotope insight into bacterial sulfate reduction in the natural environment Geochim. Cosmochim. Acta, 118, p. 98–117, doi:10.1016/j.gca.2013.05.005.

Avrahamov, N., Antler, G., Yechieli, Y., Gavrieli, I., Joye, S.B., Saxton, M., Turchyn, A.V., and Sivan, O., (2014), Anaerobic oxidation of methane by sulfate in hypersaline groundwater of the Dead Sea aquifer: Geobiology, v. 12, no. 6, p. 511–528, doi:10.1111/gbi.12095.

Bak, F., and Cypionka, H. (1987). A novel type of energy metabolism involving fermentation of inorganic sulphur compounds. Nature, 326, 891-892.

Balci N., Shanks W., Bernhard M. and Mandernack K. (2007) Oxygen and sulfur isotope systematics of sulfate produced by bacterial and abiotic oxidation of pyrite. Geochim. Chosmochim. Acta 71, 3796–3811.

Barnes, R. O., and Goldberg, E. D. (1976). Methane production and consumption in anoxic marine sediments. Geology, 4(5), 297–300.

Berner R. A. (1980) Early diagenesis: A theoretical approach. Princeton Univ Pr.

Berner R.A., The long-term carbon cycle, fossil fuels, and atmospheric oxygen. Nature, 426, 323-326 (2003)

Berner, R. A., Lasaga, A. C., and Garrels, R. M. (1983). The carbonate-silicate geochemical cycle and its effect on atmospheric carbon dioxide over the past 100 million years. Am. J. Sci, 283(7), 641-683.

Berg, P., Risgaard-Petersen, N., and Rysgaard, S. (1998). Interpretation of measured concentration profiles in sediment pore water. Limnol.Oceanogr., 43(7), 1500-1510.

Betts R. H. and Voss R. H. (1970) The kinetics of oxygen exchange between the sulfite ion and water. Can. J. Chem. 48, 2035–2041.

Blair, N.E., and Aller, R.C., (1995). Anaerobic methane oxidation in Amazon Shelf sediments. Geochim. Cosmochim. Acta 59, 3707–3715.

Blake, R. E., Surkov, A. V., Böttcher, M. E., Ferdelman, T. G. and Jørgensen, B. B. (2006) Oxygen isotope composition of dissolved sulfate in deep-sea sediments:

Eastern Equatorial Pacific Ocean. Proc Ocean Drill Prog Sci Results, vol. 201 (eds. B. B. Jørgensen, S. L. D'Hondt and D. J. Miller). ODP, pp. 1–24.

Boetius, A., Ravenschlag, K., Schubert, C. J., Rickert, D., Widdel, F., Gieseke, A., Amann, R., Jørgensen, B.B., Witte, U., and Pfannkuche, O. (2000). A marine microbial consortium apparently mediating anaerobic oxidation of methane. Nature, 407(6804), 623–6.

Booth, I. R. (1985) Regulation of cytoplasmic pH in bacteria. Microbiol. Rev. 49, 359–378.

Borowski, W. S., Hoehler, T. M., Alperin, M. J., Rodriguez, N. M., and Paull, C. K. (2000). Significance of anaerobic methane oxidation in methane-rich sediments overlying the Blake Ridge gas hydrates. Proc Ocean Drill Prog Sci Results, 164, 87–99.

Böttcher, M.E., Brumsack, H.J., and de Lange, G.J., (1998) Sulfate reduction and related stable isotope (34S, 18O) variations in interstitial waters from the eastern Mediterranean. In (Eds. Robertson, A.H.F., Emeis, K.-C., Richter, C., and Camerlenghi, A.), Proc. ODP, Sci. Results, 160: College Station, TX (Ocean Drilling Program), 365–373.

Böttcher M. E., Bernasconi S. M. and Brumsack H.J. (1999) Carbon, sulfur, and oxygen isotope geochemistry of interstitial waters from the western Mediterranean. In Proceedings of the Ocean Drilling Program, Scientific Results, vol. 161 (eds. R. Zahn, M. C. Comas and A. Klaus), pp. 413–421. Proc Ocean Drill Prog Sci Results. Ocean Drilling Program, College Station, TX.

Böttcher M. E. and Thamdrup B. (2001) Anaerobic sulfide oxidation and stable isotope fractionation associated with bacterial sulfur disproportionation in the presence of MnO2. Geochim. Cosmochim. Acta. 65, 1573–1581.

Böttcher M. E., Thamdrup B. and Vennemann T. W. (2001) Oxygen and sulfur isotope fractionation during anaerobic bacterial disproportionation of elemental sulfur. Geochim. Cosmochim. Acta 65, 1601–1609.

Böttcher M. E., Thamdrup B., Gehre M. and Theune A. (2005) 34S/32S and 18O/16O Fractionation during sulfur disproportionation by Desulfobulbus propionicus. Geomicrobiology J. 22, 219.

Böttcher M. E., Ferdelman T. G., Jørgensen B. B., Blake R. E., Surkov A. V. and Claypool G. E. (2006) Sulfur isotope fractionation by the deep biosphere within sediments of the Eastern Equatorial Pacific and Peru Margin. Proc Ocean Drill Prog Sci Results, Vol. 201 (eds. B.B. Jørgensen, S.L. D'Hondt and D.J. Miller). ODP, p.p 1-21.

Bowles, M. W., Mogollón, J. M., Kasten, S., Zabel, M. and Hinrichs, K. U. (2014). Global rates of marine sulfate reduction and implications for sub–sea-floor metabolic activities. Science, 344, 889-891.

Bradley A.S., Leavitt W. D. AND Johnston D. T. (2011). Revisiting the dissimilatory sulfate reduction pathway. Geobiology 9, 446–457.

Brüchert V. (2004) Physiological and ecological aspects of sulfur isotope fractionation during bacterial sulfate reduction. In Sulfur Biogeochemistry – Past and Present, vol. 379 (eds. J. P. Amend, K. J. Edwards and T. W. Lyons), pp. 1–16. Geological Society of America Special Paper. Geol. Soc. Am., Boulder CO, USA.

Brunner B. and Bernasconi S. M. (2005) A revised isotope fractionation model for dissimilatory sulfate reducing in sulfate reducing bacteria. Geochim. Cosmochim. Acta 69, 4759–4771.

Brunner B., Bernasconi S. M., Kleikemper J. and Schroth M. J. (2005) A model for oxygen and sulfur isotope fractionation in sulfate during bacterial sulfate reduction processes. Geochim. Cosmochim. Acta 69, 4773–4785.

Brunner B., Mielke R. E., Coleman M. (2006) Abiotic oxygen isotope equilibrium fractionation between sulfite and water. American Geophysical Union, Fall Meeting 2006, Eos Trans AGU 87, abstract No. V11C-0601.

Brunner B., Yu J.-Y., Mielke R., MacAskill J., Madzunkov S., McGenity T. and Coleman M. (2008) Different isotope and chemical patterns of pyrite oxidation related to lag and exponential growth phases of Acidithiobacillus ferrooxidans reveal a microbial growth strategy. Earth Planet. Sci. Lett.270, 63–72.

Brunner, B., Einsiedl, F., Arnold, G. L., Müller, I., Templer, S., and Bernasconi, S. M. (2012). The reversibility of dissimilatory sulphate reduction and the cell-internal multi-step reduction of sulphite to sulphide: insights from the oxygen isotope composition of sulphate. Isot. Environ, Healt. S., 48(1), 33-54.

Burdige, D. J., and Komada, T. (2011). Anaerobic oxidation of methane and the stoichiometry of remineralization processes in continental margin sediments. Limnol. Oceanog., 56(5), 1781–1796.

Canfield, D. E. (1989). Reactive iron in marine sediments. Geochim. Cosmochim. Acta, 53(3), 619-632.

Canfield, D.E., (2001a). Biogeochemistry of sulfur isotopes. In: Valley, J.W., Cole, D.R. (Eds.), Reviews in Mineralogy and Geochemistry, vol. 43. Mineral. Soc. Am., Blacksburg, VA, pp. 607–636.

Canfield D. E. (2001b) Isotope fractionation by natural populations of sulfate-reducing bacteria. Geochim. Cosmochim. Acta 65, 1117–1124.

Canfield, D. E. (2004). The evolution of the Earth surface sulfur reservoir. Am. J. of Sci., 304(10), 839-861.

Canfield D. E., Olesen C. A. and Cox R. P. (2006) Temperature and its control of isotope fractionation by a sulfate-reducing bacterium. Geochim. Cosmochim. Acta 70, 548–561.

Canfield, D. E., Farquhar, J., and Zerkle, A. L. (2010). High isotope fractionations during sulfate reduction in a low-sulfate euxinic ocean analog. Geology, 38(5), 415-418.

Chambers, L. A., Trudinger, P. A., Smith, J. W., and Burns, M. S. (1975). Fractionation of sulfur isotopes by continuous cultures of Desulfovibrio desulfuricans. Can. J. Microb., 21(10), 1602-1607.

Chiba H. and Sakai H. (1985) Oxygen isotope exchange-rate between dissolved sulfate and water at hydrothermal temperatures. Geochim. Cosmochim. Acta 49, 993–1000.

Chu, C. F., Ebie, Y., Xu, K. Q., Li, Y. Y., and Inamori, Y. (2010). Characterization of microbial community in the two-stage process for hydrogen and methane production from food waste. Int. J. Hydrogen Energ., 35(15), 8253-8261.

Cicerone, R. J., and Oremland, R. S. (1988). Biogeochemical aspects of atmospheric methane. Global biogeochemical cycles, 2(4), 299-327.

Cline, J. D. (1969). Spectrophotometric determination of hydrogen sulfide in natural water. Limnol. Oceanog., 14(3), 454-458.

Coleman, D. F., and Ballard, R. D. (2001). A highly concentrated region of cold hydrocarbon seeps in the southeastern Mediterranean Sea. Geo-Mar. Lett., 21(3), 162-167.

Coleman, D. F., Austin, J. A., Ben-Avraham, Z., Makowsky, Y., and Tchernov, D. (2012). Seafloor pockmarks, deepwater corals, and cold seeps along the continental margin of Israel. Oceanography, 25(supplement 1), 40-41

Crowe, S. A., Paris, G., Katsev, S., Jones, C., Kim, S. T., Zerkle, A. L. and Canfield, D. E. (2014). Sulfate was a trace constituent of Archean seawater. Science, 346(6210), 735-739.

Cypionka H., Smock A., and Böttcher M. E. (1998) A combined pathway of sulfur compound disproportionation in Desulfovibrio desulfuricans. FEMS Microbiol Lett. 166, 181–186.

D'Hondt S., Jørgensen B. B., Miller D. J., Batzke A., Blake R., Cragg B. A., Cypionka H., Dickens G. R., Ferdelman T., Hinrichs K., Holm N. G., Mitterer R., Spivack A., Wang G., Bekins B., Engelen B., Ford K., Gettemy G., Rutherford S. D., Sass H., Skilbeck C. G., Aiello I. W., Guèrin G., House C. H., Inagaki F., Meister P., Naehr T., Niitsuma S., Parkes R. J., Schippers A., Smith D. C., Teske A., Wiegel J., Padilla C. N. and Acosta J. L. S. (2004) Distributions of Microbial Activities in Deep Subseafloor Sediments. Science 306, 2216-2221.

Deusner, C., Holler, T., Arnold, G.L., Bernasconi, S.M., Formolo, M.J., and Brunner, B., (2014), Sulfur and oxygen isotope fractionation during sulfate reduction coupled to anaerobic oxidation of methane is dependent on methane concentration: Earth Planet. Sci. Lett., v. 399, p. 61–73, doi:10.1016/j.epsl.2014.04.047.

Dickens, G.R., O'Neil, J.R., Rea, D.K., and Owen, R.M., (1995), Dissociation of oceanic methane hydrate as a cause of the carbon isotope excursion at the end of the Paleocene: Paleoceanography, v. 10, p. 965–971, doi:10.1029/95PA02087.

Donahue M. A., Werne J. P., Meile C. and Lyons T. W. (2008) Modeling sulfur isotope fractionation and differential diffusion during sulfate reduction in sediments of the Cariaco Basin. Geochim. Cosmochim. Acta 72, 2287-2297.

Eckert T., Brunner B., Edwards E. A. and Wortmann U. G. (2011) Microbially mediated re-oxidation of sulfide during dissimilatory sulfate reduction by Desulfobacter latus. Geochim. Cosmochim. Acta 75, 3469-3485.

Eliani-Russak E. Herut, B. and Sivan O. (2013). The role of highly sratified nutrient-rich small estuaries as a source of dissolved inorganic nitrogen to coastal seawater, the Qishon (SE Mediterranean) case. Mar. Pollut. Bull., 71, 250–258.

Farquhar J., Canfield D. E., Masterson A., Bao H. and Johnston D. (2008) Sulfur and oxygen isotope study of sulfate reduction in experiments with natural populations from F_llestrand, Denmark. Geochim. Cosmochim. Acta 72, 2805–2821.

Farquhar J., Johnston D. T. and Wing B. A. (2007) Implications of conservation of mass effects on mass-dependent isotope fractionations: Influence of network structure on sulfur isotope phase space of dissimilatory sulfate reduction. Geochim. Cosmochim. Acta 71, 5862–5875.

Farquhar J., Johnston D. T., Wing B. A., Habicht K. S., Canfield D. E., Airieau S. and Thiemens M. H. (2003) Multiple sulphur isotopic interpretations of biosynthetic pathways: implications for biological signatures in the sulphur isotope record. Geobiology 1, 27–36.

Farquhar, J., Cliff, J., Zerkle, A. L., Kamyshny, A., Poulton, S. W., Claire, M., and Harms, B. (2013). Pathways for Neoarchean pyrite formation constrained by mass-independent sulfur isotopes. Proc. Natl. Acad. Sci. U.S.A., 110(44), 17638-17643.

Feng, D., and Roberts, H.H., (2011), Geochemical characteristics of the barite deposits at cold seeps from the northern Gulf of Mexico continental slope: Earth Planet. Sci. Lett., v. 309, p. 89–99, doi:10.1016/j.epsl.2011.06.017.

Fritz P., Basharmal G. M., Drimmie R. J., Ibsen J. and Qureshi R. M. (1989) Oxygen isotope exchange between sulfate and water during bacterial reduction of sulfate. Chem. Geol. 79, 99–105.

Froelich P., Klinkhammer G., Bender M., Luedtke N., Heath G. R., Cullen D., Dauphin P., Hammond D., Hartman B. and Maynard V. (1979) Early oxidation of organic matter in pelagic sediments of the eastern equatorial Atlantic: suboxic diagenesis. Geochim. Cosmochim. Acta 43, 1075-1090.

Fu, B., Aharon, P., Byerly, G.R., and Roberts, H.H., (1994), Barite chimneys on the Gulf of Mexico slope: Initial report on their petrography and geochemistry: Geo-Mar. Lett., v. 14, p. 81–87, doi:10.1007/BF01203718.

Fu, B., and Aharon, P., (1997), Origin and Depositional Model of Barite Deposits Associated with Hydrocarbon Seeps on the Gulf of Mexico Slope Offshore Louisiana: Gulf Coast Association of Geological Societies Transactions, v. 47, p. 13–20.

Gafny, S., Goren, M., and Gasith, A. (2000). Habitat condition and fish assemblage structure in a coastal mediterranean stream (Yarqon, Israel) receiving domestic effluent. In M. Jungwirth, S. Muhar, and S. Schmutz (Eds.), Assessing the Ecological Integrity of Running Waters Developments in Hydrobiology (pp. 319–330). Dordrecht: Springer Netherlands. doi:10.1007/978-94-011-4164-2

Greinert, J., Bollwerk, S.M., Derkachev, A., Bohrmann, G., and Suess, E., (2002), Massive barite deposits and carbonate mineralization in the Derugin Basin, Sea of Okhotsk: precipitation processes at cold seep sites: Earth Planet. Sci. Lett., 203, p. 165–180, doi:10.1016/S0012-821X(02)00830-0.

Habicht K. S., Gade M., Thamdrup B., Berg P. and Canfield D. E. (2002) Calibration of sulphate levels in the Archean Ocean. Science 298, 2372–2374.

Harrison A. G. and Thode H. G. (1958) Mechanism of the bacterial reduction of sulphate from isotope fractionation studies. Trans. Faraday Soc. 53, 84–92.

Heidel C., Tichomirowa M. (2011) The isotopic composition of sulfate from anaerobic and low oxygen pyrite oxidation experimenzs with ferric iron - New insights into oxidation mechanisms. Chem. Geol. 281, 305-316.

Heijs, S. K., Aloisi, G., Bouloubassi, I., Pancost, R. D., Pierre, C., Damsté, J. S., and Forney, L. J. (2006). Microbial community structure in three deep-sea carbonate crusts. Microbial Ecol., 52(3), 451-462.

Hinrichs, K. U., Hayes, J. M., Sylva, S. P., Brewer, P. G., and DeLong, E. F. (1999). Methane-consuming archaebacteria in marine sediments. Nature, 398(6730),

Hoehler, T. M., Alperin, M. J., Albert, D. B., and Martens, C. S. (1994). Field and laboratory studies of methane oxidation in an anoxic marine sediment: Evidence for a methanogen-sulfate reducer consortium. Glob. Biogeochem. Cycles, 8(4), 451–463.

Holler T., Wegener G., Niemann H., Deusner C., Ferdelman T. G., Boetius A., Brunner B., Widdel F. (2011). Carbon and sulfur back flux during anaerobic microbial oxidation of methane and coupled sulfate reduction. Proc. Natl. Acad. Sci. U.S.A. 108, 1484- 1490.

Holmkvist, L., Ferdelman, T. G., and Jørgensen, B. B. (2011). A cryptic sulfur cycle driven by iron in the methane zone of marine sediment (Aarhus Bay, Denmark). Geochim, Cosmochim. Acta, 75(12), 3581-3599.

Horner D. A. and Connick R. E. (2003) Kinetics of oxygen exchange between the two isomers of bisulfite ion, disulfite ion ($S_2O_5^{2-}$), and water as studied by oxygen-17 Nuclear Magnetic Resonance Spectroscopy. Inorg. Chem. 42, 1884–1894.

Jiang, G., Kennedy, M.J., and Christie-Blick, N., (2003), Stable isotopic evidence for methane seeps in Neoproterozoic postglacial cap carbonates: Nature, v. 426, p. 822–826, doi:10.1038/nature02201.

Johnson, C. A., Kelley, K. D., and Leach, D. L., (2004), Sulfur and Oxygen Isotopes in Barite Deposits of the Western Brooks Range, Alaska, and Implications for the Origin of the Red Dog Massive Sulfide Deposits: Econ. Geol., v. 99, p. 1435-1448, doi: 10.2113/gsecongeo.99.7.1435.

Johnston, D. T., Wing, B. A., Farquhar, J., Kaufman, A. J., Strauss, H., Lyons, T. W. and Canfield, D. E. (2005). Active microbial sulfur disproportionation in the Mesoproterozoic. Science, 310(5753), 1477-1479.

Johnston D. T., Farquhar J. and Canfield D. E. (2007) Sulfur isotope insights into microbial sulfate reduction: when microbes meet model. Geochim. Cosmochim. Acta 71, 3929–3947.

Johnston, D. T., Poulton, S. W., Fralick, P. W., Wing, B. A., Canfield, D. E., and Farquhar, J. (2006). Evolution of the oceanic sulfur cycle at the end of the Paleoproterozoic. Geochim. Cosmochim. Acta, 70(23), 5723-5739.

Johnston, D. T. (2011). Multiple sulfur isotopes and the evolution of Earth's surface sulfur cycle. Earth-Sci. Rev., 106(1), 161-183.

Johnston, D. T., Gill, B. C., Masterson, A., Beirne, E., Casciotti, K. L., Knapp, A. N., and Berelson, W. (2014). Placing an upper limit on cryptic marine sulphur cycling. Nature.

Jørgensen B. B. (1979) A theoretical model of the stable sulfur isotope distribution in marine sediments. Geochim. Cosmochim. Acta 43, 363–374

Kamyshny, A., Zerkle, A. L., Mansaray, Z. F., Ciglenečki, I., Bura-Nakić, E., Farquhar, J., and Ferdelman, T. G. (2011). Biogeochemical sulfur cycling in the water column of a shallow stratified sea-water lake: Speciation and quadruple sulfur isotope composition. Mar. Chem., 127(1), 144-154.

Kaplan I. R. and Rittenberg S. C. (1963) Microbiological fractionation of sulphur isotopes. J. Gen. Microbiol. 34, 195–212.

Kasten S. and Jørgensen B. B. (2000) Sulfate Reduction in Marine Sediments. in Marine geochemistry (eds, H. D. Schulz and M. zabel). Springer, Berlin, pp. 263-281.

Kiel, S., (2015) Did shifting seawater sulfate concentrations drive the evolution of deep-sea methane-seep ecosystems?: Proc. Roy. Soc. of Lond. B Bio. Sci., v. 282 DOI: 10.1098/rspb.2014.2908

Knittel, K., and Boetius, A. (2009). Anaerobic oxidation of methane: progress with an unknown process. Annu. Rev. Microb., 63, 311-334.

Knöller, K., Vogt, C., Richnow, H. H., and Weise, S. M. (2006). Sulfur and oxygen isotope fractionation during benzene, toluene, ethyl benzene, and xylene degradation by sulfate-reducing bacteria. Environ. Sci. technol.,40(12), 3879-3885.

Knossow, N., Blonder, B., Eckert, W., Turchyn, A. V., Antler, G., and Kamyshny, A. (2015). Annual sulfur cycle in a warm monomictic lake with sub-millimolar sulfate concentrations. Geochem. t., 16(1), 7.

Kobayashi K, Tachibana S, IshimotoM (1969) Intermediary formation of trithionate in sulfite reduction by a sulfate-reducing bacterium. J. Biochem. (Tokyo) 65, 155.

Kohl I.E. and Bao H. (2011) Triple-oxygen-isotope determination of molecular oxygen incorporation in sulfate produced during abiotic pyrite oxidation (pH = 2–11). Geochim. Cosmochim. Acta 75, 1785-1798

Kohl I.E., Asatryan R. and Bao H. (2012). No oxygen isotope exchange between water and APS–sulfate at surface temperature: Evidence from quantum chemical modeling and triple-oxygen isotope experiments. Geochim. Cosmochim. Acta 95, 106-118

Leavitt, W. D., Cummins, R., Schmidt, M. L., Sim, M. S., Ono, S., Bradley, A. S., and Johnston, D. T. (2014). Multiple sulfur isotope signatures of sulfite and thiosulfate reduction by the model dissimilatory sulfate-reducer, Desulfovibrio alaskensis str. G20. Front. Microb., 5

Leavitt, W. D., Halevy, I., Bradley, A. S., and Johnston, D. T. (2013). Influence of sulfate reduction rates on the Phanerozoic sulfur isotope record. Proc. Natl. Acad. Sci. U.S.A., 110(28), 11244-11249.

Lloyd R. M. (1968) Oxygen isotope behavior in sulfate–water system. J. Geophys. Res. 73, 6099–6110.

Loncke, L., Mascle, J., and Parties, F. S. (2004). Mud volcanoes, gas chimneys, pockmarks and mounds in the Nile deep-sea fan (Eastern Mediterranean): geophysical evidences. Mar. Petrol. Geo., 21(6), 669-689.

Lovley, D. R., and Klug, M. J. (1983). Sulfate reducers can outcompete methanogens at freshwater sulfate concentrations. Appl. Environ. Microb., 45(1), 187-192.

Luther, G. W. (1991). Pyrite synthesis via polysulfide compounds. Geochimica et Cosmochimica Acta, 55(10), 2839-2849.

MacDonald, G.J., 1990, Role of methane clathrates in past and future climates: Climatic Change, v. 16, p. 247–281, doi:10.1007/BF00144504.

Malinverno, A., and Pohlman J.W.(2011) Modeling sulfate reduction in methane hydrate-bearing continental margin sediments: Does a sulfate-methane transition require anaerobic oxidation of methane?. G3, 12, Q07006.

Mandernack K., Krouse H. R. and Skei J. M. (2003) A stable sulfur and oxygen isotopic investigation of sulfur cycling in an anoxic marine basin, Framvaren Fjord, Norway. Chem. Geol. 195, 181–200.

Mangalo M., Einsiedl F., Meckenstock R. U. and Stichler W. (2008) Influence of the enzyme dissimilatory sulfite reductase on stable isotope fractionation during sulfate reduction. Geochim. Cosmochim. Acta 71, 4161–4171.

Mangalo M., Meckenstock R. U., Stichler W. and Einsiedl F. (2007) Stable isotope fractionation during bacterial sulfate reduction is controlled by reoxidation of intermediates. Geochim. Cosmochim. Acta 71, 4161–4171.

Martens, C. S., Albert, D. B., and Alperin, M. J. (1999). Stable isotope tracing of anaerobic methane oxidation in the gassy sediments of Eckernforde Bay, German Baltic Sea. Am. J. Sci., 299(7-9), 589-610.

Martens, C. S., and Berner, R. A. (1974). Methane production in the interstitial waters of sulfate-depleted marine sediments. Science (New York, N.Y.), 185(4157), 1167–9.

Mascle, J., Sardou, O., Loncke, L., Migeon, S., Caméra, L., and Gaullier, V. (2006). Morphostructure of the Egyptian continental margin: insights from swath bathymetry surveys. Mar. Geophys. Res., 27(1), 49-59.

Mikucki, J. A., Pearson, A., Johnston, D. T., Turchyn, A. V., Farquhar, J., Schrag, D. P. and Lee, P. A. (2009). A Contemporary Microbially Maintained Subglacial Ferrous" Ocean". Science, 324(5925), 397-400.

Milucka, J., Ferdelman, T. G., Polerecky, L., Franzke, D., Wegener, G., Schmid, M., Lieberwirth, I., Wagner, M., Widdel, and Kuypers, M. M. M. (2012). Zero-valent sulphur is a key intermediate in marine methane oxidation. Nature, 491(7425), 541–6.

Mizutani Y. and Rafter T. A. (1969) Oxygen isotopic composition of sulphates—Part 4; bacterial fractionation of oxygen isotopes in the reduction of sulphates and in the oxidation of sulphur. N. Z. J. Sci. 12, 60–68.

Mizutani Y. and Rafter T. A. (1973) Isotopic behavior of sulphate oxygen in the bacterial reduction of sulphate. Geochem. J. 6, 183–191.

Müller, I. A., Brunner, B., Breuer, C., Coleman, M., and Bach, W. (2013). The oxygen isotope equilibrium fractionation between sulfite species and water. Geochim. Cosmochim. Acta, 120, 562-581.

Niemann, H., Lösekann, T., de Beer, D., Elvert, M., Nadalig, T., Knittel, K., Amann, R., Sauter, E.J., Schlüter, M., Klages, M., Foucher, J.P. and Boetius, A. (2006). Novel microbial communities of the Haakon Mosby mud volcano and their role as a methane sink. Nature, 443(7113), 854–8.

Niewöhner C., Hensen C., Kasten S., Zabel M. and Schulz H. D. (1998) Deep Sulfate Reduction Completely Mediated by Anaerobic Methane Oxidation in Sediments of the Upwelling Area off Namibia. Geochim. Cosmochim. Acta 62, 455-464.

Oliveira, T. F., Vonrhein, C., Matias, P. M., Venceslau, S. S., Pereira, I. A., and Archer, M. (2008). The crystal structure of Desulfovibrio vulgaris dissimilatory sulfite reductase bound to DsrC provides novel insights into the mechanism of sulfate respiration. J. Bio. Chem., 283(49), 34141-34149.

Omoregie, E. O., Mastalerz, V., De Lange, G., Straub, K. L., Kappler, A., Røy, H., and Boetius, A. (2008). Biogeochemistry and community composition of iron- and sulfur-precipitating microbial mats at the Chefren mud volcano (Nile Deep Sea Fan, Eastern Mediterranean). Appl. Environ. Microb., 74(10), 3198-3215.

Omoregie, E. O., Niemann, H., Mastalerz, V., De Lange, G. J., Stadnitskaia, A., Mascle, J., and Boetius, A. (2009). Microbial methane oxidation and sulfate reduction at cold seeps of the deep Eastern Mediterranean Sea. Marine Geology, 261(1), 114-127.

Ono, S., Wing, B., Johnston, D., Farquhar, J., and Rumble, D. (2006). Mass-dependent fractionation of quadruple stable sulfur isotope system as a new tracer of sulfur biogeochemical cycles. Geochimica et Cosmochimica Acta,70(9), 2238-2252.

Ono, S., Sim, M. S., a and Bosak, T. (2014). Predictive isotope model connects microbes in culture and nature. Proc. Natl. Acad. Sci. U.S.A, 111(51), 18102-18103.

Orphan, V J, House, C. H., Hinrichs, K. U., McKeegan, K. D., and DeLong, E. F. (2001). Methane-consuming archaea revealed by directly coupled isotopic and phylogenetic analysis. Science (New York, N.Y.), 293(5529), 484–7.

Orphan, Victoria J, House, C. H., Hinrichs, K.-U., McKeegan, K. D., and DeLong, E. F. (2002). Multiple archaeal groups mediate methane oxidation in anoxic cold seep sediments. Proc. Natl. Acad. Sci. U.S.A., 99(11), 7663–8.

Paris, G., Adkins, J. F., Sessions, A. L., Webb, S. M., and Fischer, W. W. (2014). Neoarchean carbonate–associated sulfate records positive Δ33S anomalies. Science, 346(6210), 739-741.

Paytan, A., Mearon, S., Cobb, K., and Kastner, M. (2002). Origin of marine barite deposits: Sr and S isotope characterization. Geology, 30(8), 747-750.

Peckmann, J., and Thiel, V., 2004, Carbon cycling at ancient methane–seeps: Chemical Geology, v. 205, p. 443–467, doi:10.1016/j.chemgeo.2003.12.025.

Pohlman J.W., Riedel M., Bauer J.E., Canuel E.A., Paull C.K., Lapham L., Grabowski K.S., Coffin R.B. and Spence G.D (2013). Anaerobic methane oxidation in low-organic content methane seep sediments. Geochim. Cosmochim. Acta, 108, 184–201.

Pyzik, A. J., and Sommer, S. E. (1981). Sedimentary iron monosulfides: kinetics and mechanism of formation. Geochim. Cosmochim. Acta, 45(5), 687-698.

Raymo, M. E., Ruddiman, W. F. and Froelich, P. N. (1988). Influence of late Cenozoic mountain building on ocean geochemical cycles. Geology, 16(7), 649-653.

Reeburgh W.S. (2007) Oceanic Methane Biogeochemistry. Chem. Rev. 107, pp 486–513.

Reeburgh, W. S. (1976). Methane consumption in Cariaco Trench waters and sediments. Earth Planet. Sci. Lett., 28(3), 337–344.

Rees C. E. (1973) A steady-state model for sulphur isotope fractionation in bacterial reduction processes. Geochim. Cosmochim. Acta 37, 1141–1162.

Rennie, V. C., and Turchyn, A. V. (2014). The preservation of and in carbonate-associated sulfate during marine diagenesis: A 25 Myr test case using marine sediments. Earth Planet. Sci. Lett., 395, 13-23.

Riedinger, N., Brunner, B., Formolo, M. J., Solomon, E., Kasten, S., Strasser, M., and Ferdelman, T. G. (2010). Oxidative sulfur cycling in the deep biosphere of the Nankai Trough, Japan. Geology, 38(9), 851-854.

Rubin-Blum, M., et al. Hydrocarbon-related microbial processes in the deep sediments of the Eastern Mediterranean Levantine Basin. FEMS Microbiol. Ecol. 87, 780–796 (2014).

Schattner, U., Lazar, M., Harari, D., and Waldmann, N. (2012). Active gas migration systems offshore northern Israel, first evidence from seafloor and subsurface data. Cont. Shelf Res., 48, 167-172.

Schoell, M. (1988). Multiple origins of methane in the earth. Chem. Geo.,71(1), 1-10

Sim M. S., Bosak T. and Ono S. (2011a) Large Sulfur Isotope Fractionation Does Not Require Disproportionation. Science 333, 74-77.

Sim M. S., Ono S., Donovan K., Templer S. P. and Bosak T. (2011b) Effect of electron donors on the fractionation of sulfur isotopes by a marine Desulfovibrio sp. Geochim. Cosmochim. Acta 75, 4244-4259.

Sisma-Ventura, G., Guzner, B., Yam, R., Fine, M., Shemesh, A., (2009). The reef builder Dendropoma petraeum—a proxy of short and long term climatic events in the eastern Mediterranean. Geochim. Cosmochim. Acta, 73, 4376–4383.

Sivan, O., Antler, G., Turchyn, A.V., Marlow, J., and Orphan, V.J., (2014), Iron oxides stimulate sulfate driven anaerobic methane oxidation in seeps. Proc. Natl. Acad. Sci. U.S.A., v. 111, p. E4139–E4147, doi:10.1073/pnas.1412269111.

Sivan, O., Schrag, D. P., and Murray, R. W. (2007). Rates of methanogenesis and methanotrophy in deep-sea sediments. Geobiology, 5(2), 141–151.

Sleep N.H. and Zahnle K., Carbon dioxide cycling and implications for climate on ancient Earth, J. Geophys. Res 106 1373-1399 (2001).

Stam M. C., Mason P. R. D., Laverman A. M., Pallud C. and Cappellen P. V. (2011) 34S/32S fractionation by sulfate-reducing microbial communities in estuarine sediments. Geochim. Cosmochim. Acta 75, 3903-3914.

Strauss, H., et al. (2012) Sulphur diagenesis in the sediments of the Kiel Bight, SW Baltic Sea, as reflected by multiple stable sulphur isotopes. Isot. Environ. Health Stud., 48, 166-179 .

Suess, E., et al., (1999), Gas hydrate destabilization: Enhanced dewatering, benthic material turnover and large methane plumes at the Cascadia convergent margin: Earth Planet. Sci. Lett., v. 170, p. 1–15, doi:10.1016/S0012-821X(99)00092-8.

Szabo, A., Tudge, A., Macnamara, J., and Thode, H. G. (1950). The distribution of S34 in nature and the sulfur cycle. Science, 111(2887), 464-465.

Thamdrup, B., Finster, K., Hansen, J. W., and Bak, F. (1993). Bacterial disproportionation of elemental sulfur coupled to chemical reduction of iron or manganese. Appl. Environ. Microb., 59(1), 101-108.

Thode, H. G., Monster, J., and Dunford, H. B. (1961). Sulphur isotope geochemistry. Geochim. Cosmochim. Acta, 25(3), 159-174.

Tudge, A. P., and Thode, H. G. (1950). Thermodynamic properties of isotopic compounds of sulphur. Can. J. of Res., 28(9), 567-578

Turchyn A.V., Brüchert V., Lyons T. W., Engel G. S., Balci N., Schrag D. P. and Brunner B. (2010) Kinetic oxygen isotope effects during dissimilatory sulfate reduction: A combined theoretical and experimental approach. Geochim. Cosmochim. Acta 74, 2011-2024.

Turchyn A.V., Sivan O. and Schrag D. (2006) Oxygen isotopic composition of sulfate in deep sea pore fluid: evidence for rapid sulfur cycling. Geobiology 4, 191-201

Valentine, D. L. (2002). Biogeochemistry and microbial ecology of methane oxidation in anoxic environments: a review. Antonie van Leeuwenhoek, 81(1-4), 271-282.

Van Cappellen, P., and Wang, Y. (1996). Cycling of iron and manganese in surface sediments; a general theory for the coupled transport and reaction of carbon, oxygen, nitrogen, sulfur, iron, and manganese. Am. J. Sci., 296(3), 197-243.

Walker J.C.G. et al. (1981) A negative feedback mechanism for the long-term stabilization of the Earth's surface temperature. J. Geophys Res 86, 9776-9782.

Wankel, S. D., Bradley, A. S., Eldridge, D. L., and Johnston, D. T. (2013). Determination and application of the equilibrium oxygen isotope effect between water and sulfite. Geochim. Cosmochim. Acta, 125, 694-711.

Ward, D. M., Brassell, S. C., and Eglinton, G. (1985). Archaebacterial lipids in hot-spring microbial mats. Nature, 318, 656 – 659.

Wehrmann, L. M., Templer, S. P., Brunner, B., Bernasconi, S. M., Maignien, L., and Ferdelman, T. G. (2011). The imprint of methane seepage on the geochemical record and early diagenetic processes in cold-water coral mounds on Pen Duick Escarpment, Gulf of Cadiz. Mar. Geo., 282(1), 118-137.

Westrich J.T and Berner R.B (1984) The role of sedimentary organic matter in bacterial sulfate reduction: The G model tested. Limnol.Oceanogr. 29, 236-249.

Whiticar, M.J, Faber, E., and Schoell, M. (1986). Biogenic methane formation in marine and freshwater environments: CO2 reduction vs. acetate fermentation—Isotope evidence. Geochimica et Cosmochimica Acta , 50(5), 693–709.

Whiticar, M.J. (1999). Carbon and hydrogen isotope systematics of bacterial formation and oxidation of methane. Chem. Geo., 161(1-3), 291–314.

Widdel, F., Kohring, G. W., and Mayer, F. (1983). Studies on dissimilatory sulfate-reducing bacteria that decompose fatty acids. Arch. Microbiol., 134(4), 286-294.

Wing, B. A., and Halevy, I. (2014). Intracellular metabolite levels shape sulfur isotope fractionation during microbial sulfate respiration. Proc. Natl. Acad. Sci. U.S.A., 111(51), 18116-18125

Wortmann U. G. (2006) A 300 m long depth profile of metabolic activity of sulfate reducing bacteria in the continental margin sediments of South Australia (ODP Site 1130) derived from inverse reaction-transport modeling. G3 7, Q05012.

Wortmann U. G. and Chernyavsky B. M. (2011) The significance of isotope specific diffusion coefficients for reaction-transport models of sulfate reduction in marine sediments. Geochim. Cosmochim. Acta 75, 3046-3056.

Wortmann U. G., Bernasconi S. M. and Böttcher M. E. (2001) Hypersulfidic deep biosphere indicates extreme sulfur isotope fractionation during single-step microbial sulfate reduction. Geology 29, 647–650.

Wortmann U. G., Chernyavsky B., Bernasconi S. M., Brunner B., Böttcher M. E. and Swart P. K. (2007) Oxygen isotope biogeochemistry of pore water sulfate in the deep biosphere: dominance of isotope exchange reactions with ambient water during microbial sulfate reduction (ODP Site 1130). Geochim. Cosmochim. Acta 71, 4221–4232.

Wuebbles, D., and Hayhoe, K. (2002). Atmospheric methane and global change. Earth-Sci. Rev., 57(3-4), 177–210.

Yao, W., and Millero, F. J. (1996). Oxidation of hydrogen sulfide by hydrous Fe (III) oxides in seawater. Mar. Chem., 52(1), 1-16.

Young, E. D., Galy, A., and Nagahara, H. (2002). Kinetic and equilibrium mass-dependent isotope fractionation laws in nature and their geochemical and cosmochemical significance. Geochim. Cosmochim. Acta, 66(6), 1095-1104.

Yoshinaga, M.Y., Holler, T., Goldhammer, T., Wegener, G., Pohlman, J.W., Brunner, B., Kuypers, M.M.M., Hinrichs, K.-U., and Elvert, M., (2014), Carbon isotope equilibration during sulphate-limited anaerobic oxidation of methane: Nature Geoscience, v. 7, p. 190–194, doi:10.1038/ngeo2069.

Zak I., Sakai H. and Kaplan I. R. (1980) Factors controlling the 18O/16O and 34S/32S isotope ratios of ocean sulfates, evaporates and interstitial sulfates from modern deep sea sediments. In Isotope Marine Chemistry. Institute of Geophysics and Planetary Physics, University of California Los Angeles, California 90024, USA, pp. 339–373 (Chapter 17).

Zeebe R. E. (2010) A new value for the stable oxygen isotope fractionation between dissolved sulfate ion and water. Geochim. Cosmochim. Acta 74, 818–828.

Zerkle, A. L., Kamyshny, A., Kump, L. R., Farquhar, J., Oduro, H., and Arthur, M. A. (2010). Sulfur cycling in a stratified euxinic lake with moderately high sulfate: constraints from quadruple S isotopes. Geochimica et Cosmochimica Acta,74(17), 4953-4970.

Zopfi, J., Ferdelman, T. G., and Fossing, H. (2004). Distribution and fate of sulfur intermediates—sulfite, tetrathionate, thiosulfate, and elemental sulfur—in marine sediments. Geol. Soc. Am. Spec. Pap, 379, 97-116.

Appendix 1: Mathematical derivation of the change in oxygen isotopes during microbial sulfate reduction

First we consider the following reaction:

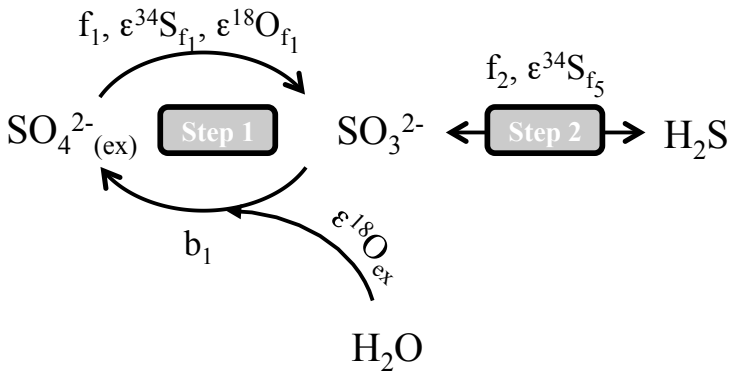

At steady flow the mass balance equation for the sulfate can be written as:

$$\frac{d[SO_4^{-2}]}{dt} = f_1 - b_1 = f_2 \quad \text{(A.1.1)}$$

And

$$dt = \frac{d[SO_4^{-2}]}{f_1 - b_1} \quad \text{(A.1.2)}$$

If the oxygen isotopic exchange between the sulfite and the ambient water >> than f_1, b_1 and f_2, the isotopic mass balance equation for $\delta^{18}O_{(SO4)}$ can be written as:

$$\frac{d\left([SO_4^{-2}]\cdot\delta^{18}O_{(SO4)}\right)}{dt} = b_1\cdot\left(\delta^{18}O_{(H2O)}+\varepsilon_{exchange}\right) - f_1\cdot\left(\delta^{18}O_{(SO4)}+\varepsilon_{SO4\text{-}SO3}\right) \quad \text{(A.1.3)}$$

According to the derivative's chine rule and eq. A.1.2:

$$\frac{d\left(\left[SO_4^{-2}\right]\cdot\delta^{18}O_{(SO4)}\right)}{dt}=\left[SO_4^{-2}\right]\cdot\frac{d\left(\delta^{18}O_{(SO4)}\right)}{dt}+\delta^{18}O_{(SO4)}\cdot(b_1-f_1) \quad (A.1.4)$$

And therefore:

$$\left[SO_4^{-2}\right]\cdot\frac{d\left(\delta^{18}O_{(SO4)}\right)}{dt}=b_1\cdot\left(\delta^{18}O_{(H2O)}+\varepsilon_{ex}-\delta^{18}O_{(SO4)}\right)-f_1\cdot(\varepsilon_{SO4\text{-}SO3}) \quad (A.1.5)$$

Rearranging eq. A.1.5 results with:

$$\frac{d\left(\delta^{18}O_{(SO4)}\right)}{b_1\cdot\left(\delta^{18}O_{(H2O)}+\varepsilon_{ex}-\delta^{18}O_{(SO4)}\right)-f_1\cdot(\varepsilon_{SO4\text{-}SO3})}=\frac{dt}{\left[SO_4^{-2}\right]} \quad (A.1.6)$$

The combination between eq. A.1.6 and A.1.2 yield:

$$\frac{d\left(\delta^{18}O_{(SO4)}\right)}{b_1\cdot\left(\delta^{18}O_{(H2O)}+\varepsilon_{ex}-\delta^{18}O_{(SO4)}\right)-f_1\cdot(\varepsilon_{SO4\text{-}SO3})}=\frac{1}{b_1-f_1}\cdot\frac{d\left[SO_4^{-2}\right]}{\left[SO_4^{-2}\right]} \quad (A.1.7)$$

The solution of eq. A.1.7

$$\ln\left(\frac{\varphi_2\left(\delta^{18}O_{(H2O)}+\varepsilon_{ex}-\delta^{18}O_{(SO4)}\right)-\varphi_1\cdot(\varepsilon_{SO4\text{-}SO3})}{\varphi_2\left(\delta^{18}O_{(H2O)}+\varepsilon_{ex}-\delta^{18}O_{(SO4)(0)}\right)-\varphi_1\cdot(\varepsilon_{SO4\text{-}SO3})}\right)=\frac{-b_1}{b_1-f_1}\cdot\ln\left(\frac{\left[SO_4^{-2}\right]}{\left[SO_4^{-2}\right]_{(0)}}\right) \quad (A.1.8)$$

Defining $b_1/f_1 \equiv \varphi_1$

$$\ln\left(\frac{\left(\delta^{18}O_{(H2O)}+\varepsilon_{ex}-\delta^{18}O_{(SO4)}\right)-\frac{1}{\varphi_1}\cdot(\varepsilon_{SO4\text{-}SO3})}{\left(\delta^{18}O_{(H2O)}+\varepsilon_{ex}-\delta^{18}O_{(SO4)(0)}\right)-\frac{1}{\varphi_1}\cdot(\varepsilon_{SO4\text{-}SO3})}\right)=-\left(\frac{\varphi_1}{\varphi_1-1}\right)\cdot\ln\left(\frac{\left[SO_4^{-2}\right]}{\left[SO_4^{-2}\right]_{(0)}}\right) \quad (A.1.9)$$

According to

$$\delta^{18}O_{(SO4)(A.E)}=\left(\delta^{18}O_{(H2O)}+\varepsilon_{ex}\right)-\frac{1}{\varphi_1}\cdot(\varepsilon_{SO4\text{-}SO3}) \quad (A.1.10)$$

Embedding equation A1.10 into A.1.9:

$$\ln\left(\frac{\delta^{18}O_{(SO4)(A.E)}-\delta^{18}O_{(SO4)}}{\delta^{18}O_{(SO4)(A.E)}-\delta^{18}O_{(SO4)(0)}}\right)=-\left(\frac{\varphi_1}{\varphi_1-1}\right)\cdot\ln\left(\frac{\left[SO_4^{-2}\right]}{\left[SO_4^{-2}\right]_{(0)}}\right) \quad (A.1.11)$$

and can be written in more general form:

$$\ln\left(\frac{\delta^{18}O_{(SO4)(A.E)}-\delta^{18}O_{(SO4)}}{\delta^{18}O_{(SO4)(A.E)}-\delta^{18}O_{(SO4)(0)}}\right)=-\theta\cdot\ln\left(\frac{\left[SO_4^{-2}\right]}{\left[SO_4^{-2}\right]_{(0)}}\right) \quad (A.1.12)$$

Where θ_O is only a function of the ratio between the backward and forward fluxes. According to Rayleigh distillation:

$$\frac{\delta^{34}S_{(SO4)}-\delta^{34}S_{(SO4)(0)}}{\varepsilon_S}=\ln\left(\frac{\left[SO_4^{-2}\right]}{\left[SO_4^{-2}\right]_{(0)}}\right) \quad (A.1.13)$$

And ultimately:

$$\ln\left(\frac{\delta^{18}O_{(SO4)(A.E)}-\delta^{18}O_{(SO4)}}{\delta^{18}O_{(SO4)(A.E)}-\delta^{18}O_{(SO4)(0)}}\right)=-\theta\cdot\frac{\delta^{34}S_{(SO4)}-\delta^{34}S_{(SO4)(0)}}{\varepsilon_S} \quad (A.1.14)$$

This relationship should conserved at higher complexity of reaction (e.g. the reaction presented in Figure 2.2 —Brunner et al., 2005; Brunner 2012).

Appendix 2: Function analysis

Continuity

This appendix addresses the question of the continuity of the following function:

$$\delta^{18}O_{SO4(t)}=\begin{cases} \dfrac{\varepsilon^{18}O_{total}}{\varepsilon^{34}S_{total}}\cdot\left(\delta^{34}S_{SO4(t)}-\delta^{34}S_{SO4(0)}\right)+\delta^{18}O_{SO4(0)} & \phi_1\cdot\phi_2\cdot\phi_3=0 \\ \delta^{18}O_{SO4(A.E)}-\exp\left(-\theta_O\cdot\dfrac{\delta^{34}S_{SO4(t)}-\delta^{34}S_{SO4(0)}}{\varepsilon^{34}S_{Stotal}}\right)\ldots & 0<\phi_1\cdot\phi_2\cdot\phi_3<1 \\ \quad\cdot\left(\delta^{18}O_{SO4(A.E)}-\delta^{18}O_{SO4(0)}\right) & \end{cases} \quad (A.2.1)$$

where $\varepsilon^{34}S_{total}$ and $\varepsilon^{18}O_{total}$ are the measured sulfur and oxygen isotope fractionations, respectively, and $\delta^{34}S_{SO4(t)}$, $\delta^{34}S_{SO4(0)}$, $\delta^{18}O_{SO4(t)}$ and $\delta^{18}O_{SO4(0)}$ are the isotopic compositions of sulfur and oxygen in the residual sulfate at time t and time 0, respectively. $\delta^{18}O_{SO4(A.E)}$ is the isotopic composition of oxygen in the residual sulfate at apparent equilibrium, and θ_O is a parameter initially formulated by Brunner et al. (2005).

By definition:

$$\theta_O=\frac{\phi_1\cdot\phi_3}{1-\phi_1\cdot\phi_3} \quad (A.2.2)$$

$$\delta^{18}O_{SO4(A.E)}=\delta^{18}O_{H2O}+\varepsilon^{18}O_{ex}+\frac{\varepsilon^{18}O_{f\_1}}{\phi_1\cdot\phi_3}+\frac{\varepsilon^{18}O_{f\_3}}{\phi_3} \quad (A.2.3)$$

$$\varepsilon^{34}S_{total}=S^{34}S_{f\_1}+\phi_1\cdot S^{34}S_{f\_3}+\phi_1\cdot\phi_3\cdot S^{34}S_{f\_4} \quad (A.2.4)$$

One can notice by inspection that A.2.3 diverges for $\phi_1 = 0$ or $\phi_3 = 0$. This is the reason why $\delta^{18}O_{SO4(t)}$ needs to be defined as a piecewise function, and its continuity needs to be studied for the singular point.

I would like to examine the behaviour of $\delta^{18}O_{SO4(t)}$ where ϕ_3 tends to 0, that is where all the sulfite produced in the cell is reoxidized back to sulfate. One can observe that the following limits are sensible as the constants can be neglected with respect to the divergent terms:

$$\lim_{\phi 3 \to o} \delta^{18}O_{SO4(A.E)} \approx \frac{\varepsilon^{18}O_{f\_1}}{\phi_1 \cdot \phi_3} + \frac{\varepsilon^{18}O_{f\_3}}{\phi_3} \quad (A.2.5)$$

$$\lim_{\phi 3 \to o} \theta_O \approx \phi_1 \cdot \phi_3 \quad (A.2.6)$$

$$\lim_{\phi 3 \to o} \varepsilon^{34}S_{total} \approx S^{34}S_{f\_1} + \phi_1 \cdot S^{34}S_{f\_3} \quad (A.2.7)$$

and since:

$$\lim_{x \to o} \exp(x) \approx 1+x$$

we can write:

$$\lim_{\phi 3 \to o} \exp\left(-\theta_O \cdot \frac{\delta^{34}S_{SO4(t)} - \delta^{34}S_{SO4(0)}}{\varepsilon^{34}S_{Stotal}}\right) \approx 1 - \theta_O \cdot \frac{\delta^{34}S_{SO4(t)} - \delta^{34}S_{SO4(0)}}{\varepsilon^{34}S_{Stotal}} \quad (A.2.8)$$

Hence, we can substitute equation A.2.8 into the function A.2.1

$$\delta^{18}O_{SO4(0)} = \delta^{18}O_{SO4(A.E)} - \delta^{18}O_{SO4(A.E)} + \delta^{18}O_{SO4(0)} + \ldots \\ \theta_O \cdot \frac{\delta^{34}S_{SO4(t)} - \delta^{34}S_{SO4(0)}}{\varepsilon^{34}S_{Stotal}} (\delta^{18}O_{SO4(A.E)} - \delta^{18}O_{SO4(0)}) \quad (A.2.9)$$

Rearranging equation A.2.9:

$$\frac{\delta^{18}O_{SO4(t)} - \delta^{18}O_{SO4(0)}}{\delta^{34}S_{SO4(t)} - \delta^{34}S_{SO4(0)}} = \frac{\theta_O}{\varepsilon^{34}S_{total}} \left(\delta^{18}O_{SO4(A.E)} - \delta^{18}O_{SO4(0)}\right) \quad (A.2.10)$$

inserting equation A.2.5 into equation A.2.10

$$\frac{\delta^{18}O_{SO4(t)} - \delta^{18}O_{SO4(0)}}{\delta^{34}S_{SO4(t)} - \delta^{34}S_{SO4(0)}} \approx \frac{\theta_O}{\varepsilon^{34}S_{total}} \left(\frac{\varepsilon^{18}O_{f\_1}}{\phi_1 \cdot \phi_3} + \frac{\varepsilon^{18}O_{f\_3}}{\phi_3}\right) \quad (A.2.11)$$

inserting equation A.2.6 and A.2.7 into equation A.2.11:

$$\frac{\delta^{18}O_{SO4(t)}-\delta^{18}O_{SO4(0)}}{\delta^{34}S_{SO4(t)}-\delta^{34}S_{SO4(0)}}\approx\frac{\phi_1\cdot\phi_3}{S^{34}S_{f\_1}+\phi_1\cdot S^{34}S_{f\_3}}\left(\frac{\varepsilon^{18}O_{f\_1}}{\phi_1\cdot\phi_3}+\frac{\varepsilon^{18}O_{f\_3}}{\phi_3}\right)\quad(A.2.12)$$

and finally:

$$\frac{\delta^{18}O_{SO4(t)}-\delta^{18}O_{SO4(0)}}{\delta^{34}S_{SO4(t)}-\delta^{34}S_{SO4(0)}}\approx\frac{\varepsilon^{18}O_{f\_1}+\phi_1\cdot\varepsilon^{18}O_{f\_3}}{S^{34}S_{f\_1}+\phi_1\cdot S^{34}S_{f\_3}}\quad(A.2.13)\quad\underline{\textbf{Q.E.D}}$$

The functional form of $\delta^{18}O_{SO4}$, where $\phi_3\rightarrow 0$ is also the solution where $\delta^{18}O_{SO4}$ is affected only by kinetic isotope fractionation (similar to $\delta^{34}S_{SO4}$).

Therefore $\delta^{18}O_{SO4}$ is well defined by two continuous functions and can be written as:

$$\delta^{18}O_{SO4(t)}=\begin{cases}\frac{\varepsilon^{18}O_{total}}{\varepsilon^{34}S_{total}}\cdot\left(\delta^{34}S_{SO4(t)}-\delta^{34}S_{SO4(0)}\right)+\delta^{18}O_{SO4(0)} & \phi_1\cdot\phi_2\cdot\phi_3=0\\ \delta^{18}O_{SO4(A.E)}-\exp\left(-\theta_O\cdot\frac{\delta^{34}S_{SO4(t)}-\delta^{34}S_{SO4(0)}}{\varepsilon^{34}S_{Stotal}}\right)\cdots & 0<\phi_1\cdot\phi_2\cdot\phi_3<1\\ \qquad\cdot\left(\delta^{18}O_{SO4(A.E)}-\delta^{18}O_{SO4(0)}\right)\end{cases}\quad(A.2.14)$$

Mathematical term for the slope of the apparent linear phase (SALP)

I define the slope of the apparent linear phase (SALP), as an approximation of the $\delta^{18}O_{SO4}$ vs. $\delta^{34}S_{SO4}$ curve to a linear line where gradient of the slope is always the highest at the onset of this curve (in marine settings). Therefore, I will analyse the behaviour of this curve around the point $\delta^{18}O_{SO4(0)}$, $\delta^{34}S_{SO4(0)}$. Recalling that the first order Taylor expression approximates a function to a straight line I will formulate the mathematical term for the apparent linear phase.

Since at $\phi_1\cdot\phi_2\cdot\phi_3=0$ the $\delta^{18}O_{SO4}$ vs. $\delta^{34}S_{SO4}$ curve already gives a straight line I will only deal with the case where $0<\phi_1\cdot\phi_2\cdot\phi_3<1$.

First we can recognize that the $\delta^{18}O_{SO4}$ dependence on $\delta^{34}S_{SO4}$ is of the form:
$a \cdot e^{bx} + c \approx a + c + b \cdot a \cdot x$

Therefore:

$$\delta^{18}O_{SO4(t)} = -\delta^{18}O_{SO4(A.E)} + \delta^{18}O_{SO4(0)} + \delta^{18}O_{SO4(A.E)} - \theta_O \cdot \frac{\delta^{34}S_{SO4(t)} - \delta^{34}S_{SO4(0)}}{\varepsilon^{34}S_{Stotal}} \cdot \left(\delta^{18}O_{SO4(A.E)} - \delta^{18}O_{SO4(0)}\right)$$

rearranging:

$$\delta^{18}O_{SO4(t)} = \delta^{18}O_{SO4(0)} - \theta_O \cdot \frac{\delta^{34}S_{SO4(t)} - \delta^{34}S_{SO4(0)}}{\varepsilon^{34}S_{Stotal}} \cdot \left(\delta^{18}O_{SO4(A.E)} - \delta^{18}O_{SO4(0)}\right)$$

in this equation $\delta^{18}O_{SO4}$ is linearly correlated to $\delta^{34}S_{SO4}$.

The slope of this straight line (SALP) is therefore:

$$SALP = -\theta_O \cdot \frac{\left(\delta^{18}O_{SO4(A.E)} - \delta^{18}O_{SO4(0)}\right)}{\varepsilon^{34}S_{Stotal}}$$

QED

Appendix 3: Codes

Plotting $E^{33}S$ vs. $e^{34}S_{total}$ diagram

%This code generates the $E^{33}S$ vs. $\varepsilon^{34}S_{total}$ (Chapter 2)

```
clear all

f=figure;
hold on;

theta=0.5147;%equilibrium between 34S and 33S fractionation

a3=0.975; %sulfur 34 fractionation step 3
a4=0.975; %sulfur 34 fractionation step 4
a5=0.975;%sulfur 34 fractionation step 5


a333=a3^theta;%sulfur 33 fractionation step 3
a334=a4^theta;%sulfur 33 fractionation step 4
a335=a5^theta;%sulfur 33 fractionation step 5

T=[0.01 1 2 3 4 5 6 7  8 9 9.9999999]*10^-1;

T1=linspace(0.001,0.99999999,30);

T2=[9.999999]*10^-1;

for i=1:length(T2)

   X4=T2(i);

   for j=1:length(T)
      X3=T(j);
      X1=T1;

      a34(1:length(T1),j)=((X1.*X3.*X4)+X1*X3*(1-X4)*a5+X1*(1-X3)*a4*a5+...
      (1-X1)*a3*a4*a5)/(a3*a4*a5); %calculating total 34S fractionation
      a33(1:length(T1),j)=((X1.*X3.*X4)+X1*X3*(1-X4)*a335+X1*(1-X3)*a334*a335+...
      (1-X1)*a333*a334*a335)/(a333*a334*a335); %calculating total 33S fractionation

   Delta(1:length(T1),j)=1000*((a33(1:length(T1),j))-(a34(1:length(T1),j)).^0.515);
   %Calculating 33E

   end

   %Plotting
  figure (f)
 switch i
      case 2
      plot(epsilon34(1:length(T1),:),Delta(1:length(T1),:),'color',[.8 .8 .8],'linewidth',1)
```

```
      case 1
      plot(epsilon34(1:length(T1),:),Delta(1:length(T1),:),'color',[.0 .0 .0],'linewidth',1)

 end
  for j=1:length(T)
      X1=T(j);
      X3=T1;

      a34(1:length(T1),j)=((X1.*X3.*X4)+X1*X3*(1-X4)*a5+X1*(1-X3)*a4*a5+...
      (1-X1)*a3*a4*a5)/(a3*a4*a5);%Calculating total 34S fractionation
      a33(1:length(T1),j)=((X1.*X3.*X4)+X1*X3*(1-X4)*a335+X1*(1-X3)*a334*a335+...
      (1-X1)*a333*a334*a335)/(a333*a334*a335); %Calculating total 33S fractionation

  Delta(1:length(T1),j)=1000*((a33(1:length(T1),j))-(a34(1:length(T1),j))).^0.515);
     %Calculating 33E


   end
  %Plotting
   figure (f)
   switch i
      case 2
      plot(epsilon34(1:length(T1),:),Delta(1:length(T1),:),'color',[.8 .8 .8],'linewidth',1)

      case 1
      plot(epsilon34(1:length(T1),:),Delta(1:length(T1),:),'color',[.0 .0 .0],'linewidth',1)
   end

end

z=get(f,'children');
set(z(end),'YDir','reverse','XDir','reverse','FontName','Times new
Roman','FontSize',[16],'FontWeight','Bold');
axis square

Published with MATLAB® R2014a
```

Plotting θ_o vs. $e^{34}S_{total}$ diagram

%This code generates the θ_0 vs. $\varepsilon^{34}S_{total}$ (Chapter 2)

```
f=figure;
hold on;

T=[1 2 3 4 5 6 7  8 9 9.9999999]*10^-1;

T1=linspace(0.1,0.9999999,30);

T2=[4 7]*10^-1;

for i=1:length(T2)
```

```
   X4=T2(i);

   for j=1:length(T)
      X3=T(j);
      X1=T1;

      a34(1:length(T1),j)=((X1.*X3.*X4)+X1*X3*(1-X4)*a5+X1*(1-X3)*a4*a5+...
      (1-X1)*a3*a4*a5)/(a3*a4*a5);%total 34S fractionation

   epsilon34(1:length(T1),j)=1000*(1-a34(1:length(T1),j)); %fractionation for sulfur
    C(1:length(T1),j)=X1.*X3./(1-X1.*X3);%theta calculation


   end
%plotting
  figure (f)
 switch i
      case 2
      semilogy(epsilon34(1:length(T1),:),C(1:length(T1),:),'color',[.8 .8 .8],'linewidth',1)

      case 1
     semilogy(epsilon34(1:length(T1),:),C(1:length(T1),:),'color',[.0 .0 .0],'linewidth',1)
   end

   for j=1:length(T)
      X1=T(j);
      X3=T1;


      a34(1:length(T1),j)=((X1.*X3.*X4)+X1*X3*(1-X4)*a5+X1*(1-X3)*a4*a5+...
      (1-X1)*a3*a4*a5)/(a3*a4*a5);%total 34S fractionation

   epsilon34(1:length(T1),j)=1000*(1-a34(1:length(T1),j)); %fractionation for sulfur
    C(1:length(T1),j)=X1.*X3./(1-X1.*X3); %theta calculation


   end


   end

     figure (f)
  switch i
      case 2
      semilogy(epsilon34(1:length(T1),:),C(1:length(T1),:),'color',[.8 .8 .8],'linewidth',1)

      case 1
     semilogy(epsilon34(1:length(T1),:),C(1:length(T1),:),'color',[.0 .0 .0],'linewidth',1)
   end



z=get(f,'children');
set(z(end),'YDir','reverse','XDir','reverse','FontName','Times new
Roman','FontSize',[16],'FontWeight','Bold');
```

axis square
Undefined function or variable 'a5'.

Published with MATLAB® R2014a

Reactive transport model

```
function [SO4 S32O4 S34O4 SO164 SO184 D]= Timestep2(X,X32,X34,X16,X18,SRR,X1,X3,Ds)

% This function receives as an input the concentrations of the different sulfate isotopologues at time
% n
% and calculate the concentration at time n+1


% this function receives the concentration of sulfate (X), sulfur32 (X32), sulfur 34 (X34), Oxygen 16
%(X16), Oxygen 18 (X18), sulfate reduction rate (SRR) the intracellular fluxes ratios X1 and X3 (see
%chapter 2), and the effective diffusion coefficient of sulfate at time n

% the output is sulfate (SO4), sulfur32 (S32O4), sulfur 34 (S34O4), Oxygen 16 (SO164), Oxygen 18
%(SO184) at time n+1
% D is the maximum absolute difference between the concentration at time n and n+1


Rcdt=0.045005;
Rsmow= 0.0020052;

 X(X<0)=0;
 X32(X32<0)=0;
 X34(X34<0)=0;
 X16(X16<0)=0;
 X18(X18<0)=0;

d34Si=(X34./X32-Rcdt)/Rcdt*1000;
d18Oi=(X18./X16-Rsmow)/Rsmow*1000;



dt=1; %the time interval- sec
dz=1;% depth interval- cm
W=10^-1/365/24/60*10; %mm/min


SO4=nan*X;
S32O4=nan*X32;
S34O4=nan*X34;
SO164=nan*X16;
SO184=nan*X18;



A=SRR;

a=1.022;
```

```
for i=2:length(X)-1

   d34Sfrac=frac(X(i,:),X(i,:)-SRR,d34Si(i,:),X1(:),X3(:));
   d18Ofrac=OS(X(i,:),X(i,:)-SRR,d18Oi(i,:),X1(:),X3(:));


   Rs=(d34Sfrac)/1000*Rcdt+Rcdt;
   Ro=(d18Ofrac)/1000*Rsmow+Rsmow;

   SRR34=X34(i,:)'-(X(i,:)'-SRR).*Rs./(Rs+1);
   SRR32=X32(i,:)'-(X(i,:)'-SRR)./(Rs+1);



   SRR16=X16(i,:)'-(X(i,:)'-SRR)./(Ro+1);
   SRR18=X18(i,:)'-(X(i,:)'-SRR).*Ro./(Ro+1);


   if X(i,1)>X(1)*0.01
      SRR=A;
   else
      SRR=A*X(i,1)/(X(1)*0.01);
   end

    if SO4(i,:)<=X(1)*0.001 %|| isnan(d34Si(i,j)) || isnan(d34Si(i,j))
   SO4(i,:)=0;
   S32O4(i,:)=0;
   S34O4(i,:)=0;
   SO164(i,:)=0;
   SO184(i,:)=0;

   %solving the equation for each depth
     else
  for j=1:length(X3)



  S32O4(i,j)=dt*(Ds*(X32(i-1,j)-2*X32(i,j)+X32(i+1,j)))/dz^2-SRR32(j)+X32(i,j)+W*(X32(i,j)-
X32(i+1,j))/(2*dz);
  S34O4(i,j)=(dt*(Ds*(X34(i-1,j)-2*X34(i,j)+X34(i+1,j))/dz^2-SRR34(j))+X34(i,j))+W*(X34(i,j)-
X34(i+1,j))/(2*dz);

   SO164(i,j)=(dt*(Ds*(X16(i-1,j)-2*X16(i,j)+X16(i+1,j))/dz^2-SRR16(j))+X16(i,j))+W*(X16(i,j)-
X16(i+1,j))/(2*dz);
   SO184(i,j)=(dt*(Ds*(X18(i-1,j)-2*X18(i,j)+X18(i+1,j))/dz^2-SRR18(j))+X18(i,j))+W*(X18(i,j)-
X18(i+1,j))/(2*dz);


  end

      SO4(i,:)=dt*(Ds*(X(i-1,:)-2*X(i,:)+X(i+1,:))/dz^2+W*(X(i,:)-X(i+1,:))/(2*dz)-SRR)+X(i,:);


    end
end
```

```
SO4(1,:)=X(1,:);
SO4(length(X),:)=X(end,:);

S32O4(1,:)=X32(1,:);
S32O4(length(X32),:)=X32(end,:);

S34O4(1,:)=X34(1,:);
S34O4(length(X),:)=X34(end,:);

SO184(1,:)=X18(1,:);
SO184(length(X),:)=X18(end,:);

SO164(1,:)=X16(1,:);
SO164(length(X),:)=X16(end,:);

SO4(1,:)=X(1,:);
SO4(length(X),:)=X(end,:);



S32O4(S32O4<SRR)=0;
S34O4(S34O4<SRR)=0;
SO184(SO184<SRR)=0;
SO164(SO164<SRR)=0;
SO4(SO4<SRR)=0;


for i=1:length(X3)
D(i,:)=[max(abs(SO4(:,i)-X(:,i)));max(abs(SO164(:,i)-X16(:,i)));max(abs(SO184(:,i)-
X18(:,i)));max(abs(S32O4(:,i)-X32(:,i)));max(abs(S34O4(:,i)-X34(:,i)))];
end

D=max(D(:));
end


function d18Of=OS(SO4i,SO4f,d18Oi,X1,X3)

%this fanction calculate the oxygen isotope composition during
%bacterial sulfate reduction

%input: SO4i- initial sulfate concetration
%SO4f- final sulfate concetration
%d18Oi- initial oxigen isotopic composition
%X1 and X3- the fluxs ratio for steps 1 and 3 (see chapter 2)
%output: d18Of- final oxygen isotopic composition

f=SO4f/SO4i;

epsilon=-3+25*X1+25*X1.*X3;%sulfur fractionation

theta=X1.*X3./(1-X1.*X3);%thetaO value
```

```
AE=17+0+1./X3.*25/4-3./4./(X1.*X3);%apparent equilibrium value


d18Of=exp(theta.*log(f)).*(-AE+d18Oi')+AE;

end

function d34Sf=frac(SO4i,SO4f,d34Si,X1,X3)

%this function calculate the sulfur isotope composition during
%bacterial sulfate reduction

%input: SO4i- initial sulfate concentration
%SO4f- final sulfate concentration
%S18Oi- initial sulfur isotopic composition
%X1 and X3- the fluxs ratio for steps 1 and 3 (see chapter 2)
%output: S18Of- final sulfur isotopic composition

f=SO4f/SO4i;

 epsilon=-3+25*X1+50*X1.*X3;%sulfur fractionation

 d34Sf=d34Si'-epsilon.*log(f);

end
```

Published with MATLAB® R2014a

Appendix 4: Data Repository

A.4.1 Data tables for Chapter 3

$\delta^{18}O_{(H2O)}$= -5.6‰

Experiment	Sample	Time (days)	SO_4 (mM)	H_2S (mM)	Cells (#/ml)	$\delta^{34}S$ (SO4)	$\delta^{18}O$ (SO4)
Lactate	0.0	0.0	21.0	0.1	8.34E+06	-1.9	10.1
Lactate	1.0	1.2	20.3	0.3	3.11E+07	-1.6	9.9
Lactate	2.0	1.7	18.9	0.4	1.19E+08	-1.4	9.8
Lactate	3.0	2.2	17.4	1.6	2.72E+08	-1.1	9.8
Lactate	4.0	2.7	14.1	2.4	3.90E+08	-0.1	9.8
Lactate	5.0	3.0		4.2	5.51E+08	0.8	9.5
Lactate	6.0	3.2	10.4	5.0	7.21E+08	1.9	9.8
Lactate	7.0	3.7	10.5	5.3	8.34E+08	2.9	10.1
Lactate	8.0	3.9	10.3	5.1	9.73E+08	2.8	9.9

Experiment	Sample	Time (days)	$\delta^{33}S$ (SO4)	$\delta^{34}S$ (SO4)	$\delta^{33}S$ (H2S)	$\delta^{34}S$ (H2S)
Lactate	5.0	3.0	0.6	1.3	-3.1	-6.0
Lactate	6.0	3.2	0.7	1.6	-3.0	-5.7
Lactate	7.0	3.7	1.4	2.7	-2.9	-5.5

$\delta^{18}O_{(H2O)}$= 32.2‰

Experiment	Sample	Time (days)	SO_4 (mM)	H_2S (mM)	Cells (#/ml)	$\delta^{34}S$ (SO4)	$\delta^{18}O$ (SO4)
Lactate	0	0.2	17.9	0.6	4.18E+06	-0.6	9.6
Lactate	1	2.2	17.0	1.4	5.00E+07	-0.1	9.3
Lactate	2	2.9	15.1	4.1	1.04E+08	0.3	9.3
Lactate	3	3.1	14.1	4.6	2.21E+08	0.0	9.2
Lactate	4	3.4	12.4	5.3	3.04E+08	1.2	9.2
Lactate	5	3.8	9.2	5.1	4.46E+08	3.5	9.5
Lactate	6	4.0	8.9	8.3	4.87E+08	3.5	10.0
Lactate	7	4.4	9.0	8.4	4.18E+08	3.5	9.2

$\delta^{18}O_{(H2O)}$= 75.3‰

Experiment	Sample	Time (days)	SO_4 (mM)	H_2S (mM)	Cells (#/ml)	$\delta^{34}S$ (SO4)	$\delta^{18}O$ (SO4)
Lactate	0	0.2	20.3	0.3	5.83E+06	-0.7	9.3
Lactate	1	2.2	19.6	1.3	2.67E+07	-0.5	9.2

Lactate	2	2.9	18.2	3.0	1.06E+08	-0.2	9.4
Lactate	3	3.1	16.7	4.5	1.84E+08	0.3	8.7
Lactate	4	3.4	15.9	5.3	2.63E+08	0.4	9.8
Lactate	5	3.8	12.0	7.0	3.87E+08	2.5	9.5
Lactate	6	4.0	11.5	8.9	3.81E+08	2.8	9.9
Lactate	7	4.4	11.3	8.3	5.83E+08	3.7	10.1

$\delta^{18}O_{(H2O)}$= -5.6‰

Experiment	Sample	Time (days)	SO_4 (mM)	H_2S (mM)	Cells (#/ml)	$\delta^{34}S$ (SO4)	$\delta^{18}O$ (SO4)
Malate	0	0.0	21.9	0.0	7.21E+06	1.2	10.2
Malate	1	2.3	22.4	0.3	1.33E+07	1.7	10.3
Malate	2	3.0	18.2	0.5	3.11E+07	2.0	10.3
Malate	3	4.0	18.0	1.1	1.19E+08	2.6	10.6
Malate	4	4.8	16.3	2.3	2.72E+08	4.0	10.5
Malate	5	5.3	15.7	3.4	3.90E+08	5.4	10.8
Malate	6	5.8	14.1	4.7	5.51E+08	8.0	11.3
Malate	7	6.3	12.6	6.4	7.21E+08	9.6	12.0

$\delta^{18}O_{(H2O)}$= 72.9‰

Experiment	Sample	Time (days)	SO_4 (mM)	H_2S (mM)	Cells (#/ml)	$\delta^{34}S$ (SO4)	$\delta^{18}O$ (SO4)
Malate	0	0.3	21.4	0.0	2.45E+08	-0.8	9.4
Malate	1	3.5	20.3	0.4	1.13E+09	0.5	10.6
Malate	2	3.9	19.9	1.3	4.16E+09	0.9	11.0
Malate	3	4.5	18.7	2.8	9.31E+09	2.3	12.8
Malate	4	5.3	14.7	3.6	1.19E+10	5.1	17.1
Malate	5	5.9	14.2	4.1	1.35E+10	8.2	21.2
Malate	6	6.3	14.1	7.4	2.45E+10	8.1	21.7

Experiment	Sample	Time (days)	$\delta^{33}S$ (SO4)	$\delta^{34}S$ (SO4)	$\delta^{33}S$ (H2S)	$\delta^{34}S$ (H2S)
Malate	3	4.5	1.1	2.1	-11.1	-21.6
Malate	4	5.3	2.6	5.0	-10.7	-20.8
Malate	5	5.9	4.2	8.3	-10.3	-20.1

$\delta^{18}O_{(H2O)}$= -5.4‰

Experiment	Sample	Time (days)	SO_4 (mM)	H_2S (mM)	Cells (#/ml)	$\delta^{34}S$ (SO4)	$\delta^{18}O$ (SO4)
Fructose	0	0.0		0.1	6.42E+06	1.3	10.3
Fructose	1	3.8	20.1	0.2	7.44E+07	1.8	10.6
Fructose	2	5.1	19.7	0.1	8.44E+07	2.8	10.5
Fructose	3	5.9	19.8	0.6	1.02E+08	2.5	10.6

Fructose	4	6.9	19.3	0.8	2.10E+08	3.2	10.5
Fructose	5	7.7	19.1	1.2	2.36E+08	3.7	10.9
Fructose	6	8.1	18.0	1.9	4.45E+08	5.1	11.3
Fructose	7	8.7	17.8	2.3	5.87E+08	5.7	11.6
Fructose	8	9.1	18.0	2.8	6.42E+08	6.9	11.8

$\delta^{18}O_{(H2O)}$= 30.9‰

Experiment	Sample	Time (days)	SO_4 (mM)	H_2S (mM)	Cells (#/ml)	$\delta^{34}S$ (SO4)	$\delta^{18}O$ (SO4)
Fructose	0	0.0	20.3	0.2	1.26E+08	-0.5	9.3
Fructose	1	2.2	20.3	0.3		-0.5	9.5
Fructose	2	4.1	19.9	0.6	1.90E+09	-0.2	9.9
Fructose	4	5.8	19.2	1.4	4.44E+09	1.2	11.4
Fructose	5	7.2	17.7	2.5	8.04E+09	3.0	12.5
Fructose	6	7.9	14.8	3.7	1.23E+10	5.5	13.7
Fructose	7	8.2	15.1	3.8	1.26E+10	5.1	13.6

Experiment	Sample	Time (days)	$\delta^{33}S$ (SO4)	$\delta^{34}S$ (SO4)	$\delta^{33}S$ (H2S)	$\delta^{34}S$ (H2S)
Fructose	2	4.1	-0.4	-0.7	-12.4	-24.2
Fructose	4	5.8	0.9	1.7	-10.7	-20.8
Fructose	5	7.2	1.7	3.2	-11.3	-21.9
Fructose	7	8.2	2.5	4.9	-8.0	-15.5

$\delta^{18}O_{(H2O)}$= 74.7‰

Experiment	Sample	Time (days)	SO_4 (mM)	H_2S (mM)	Cells (#/ml)	$\delta^{34}S$ (SO4)	$\delta^{18}O$ (SO4)
Fructose	0	0.0	20.3	0.6	5.82E+06	-0.8	9.2
Fructose	1	2.2	20.2	0.8		-0.6	9.3
Fructose	2	4.1	20.5	1.3	3.22E+07	0.0	11.2
Fructose	3	5.8	17.9	2.1	8.44E+07	0.9	11.0
Fructose	4	7.2	11.9	8.5	9.29E+08	4.9	17.9
Fructose	5	7.2	15.9	6.8	6.13E+08	4.1	17.3
Fructose	6	7.2	16.0	6.9	5.82E+08	3.7	17.5

$\delta^{18}O_{(H2O)}$= -5.3‰

Experiment	Sample	Time (days)	SO_4 (mM)	H_2S (mM)	Cells (#/ml)	$\delta^{34}S$ (SO4)	$\delta^{18}O$ (SO4)
Ethanol	0	0.0		0.0	2.02E+08	1.1	10.3
Ethanol	1	1.9	20.8	0.1		1.6	10.3
Ethanol	2	5.8	19.0	1.8	5.70E+09	2.6	10.8

Ethanol	3	7.0	17.9	2.8	9.11E+09	3.1	10.7
Ethanol	4	8.1	16.4	4.7	1.54E+10	4.7	11.0
Ethanol	5	8.8	14.9	6.8	2.26E+10	5.9	11.4
Ethanol	6	9.3	14.7	6.4	2.11E+10	6.3	11.8
Ethanol	7	10.0	14.2	6.4	2.10E+10	6.5	11.6
Ethanol	8	10.6	14.5	6.1	2.02E+10	6.6	11.7

$\delta^{18}O_{(H2O)}$= 75.4‰

Experiment	Sample	Time (days)	SO_4 (mM)	H_2S (mM)	Cells (#/ml)	$\delta^{34}S$ (SO4)	$\delta^{18}O$ (SO4)
Ethanol	0	0.7	20.2	0.4	2.80E+08	-0.2	9.5
Ethanol	1	6.0	19.6	1.1	3.47E+09	0.0	10.1
Ethanol	3	8.1	18.6	2.5	8.27E+09	0.6	10.1
Ethanol	4	9.0	17.5	6.1	2.00E+10	1.7	11.8
Ethanol	5	9.8	15.6	5.9	1.96E+10	3.4	13.3
Ethanol	6	10.9	12.8	6.7	2.23E+10	6.3	17.0
Ethanol	7	11.8	11.4	8.5	2.80E+10	7.6	18.4

Experiment	Sample	Time (days)	$\delta^{33}S$ (SO4)	$\delta^{34}S$ (SO4)	$\delta^{33}S$ (H2S)	$\delta^{34}S$ (H2S)
Ethanol	4	9.0	0.7	1.5	-9.1	-17.6
Ethanol	5	9.8	1.9	3.7	-8.0	-15.5
Ethanol	6	10.9	3.3	6.5	-8.1	-15.7
Ethanol	7	11.8			-7.3	-14.2

$\delta^{18}O_{(H2O)}$= 31.5‰

Experiment	Sample	Time (days)	SO_4 (mM)	H_2S (mM)	Cells (#/ml)	$\delta^{34}S$ (SO4)	$\delta^{18}O$ (SO4)
Ethanol	0	0.8	20.2	0.4	2.36E+08	-0.7	9.3
Ethanol	1	6.0	19.0	1.7	5.39E+09	0.4	9.9
Ethanol	3	8.1	16.8	3.6	1.18E+10	2.3	11.6
Ethanol	4	9.0	15.1	7.4	2.45E+10	3.3	11.9
Ethanol	5	9.8	14.7	6.8	2.24E+10	3.7	12.8
Ethanol	6	10.9	11.2	8.6	2.86E+10	7.8	15.1
Ethanol	7	11.8	11.3	7.1	2.36E+10	8.1	15.3

$\delta^{18}O_{(H2O)}$= -4.7‰

Experiment	Sample	Time (days)	SO_4 (mM)	H_2S (mM)	Cells (#/ml)	$\delta^{34}S$ (SO4)	$\delta^{18}O$ (SO4)
Glucose	1	0.2	20.4	0.0	6.83E+07	0.9	10.4
Glucose	2	3.8	20.2	0.1		1.3	10.5
Glucose	3	9.3	18.1			1.1	10.3
Glucose	4	15.1	19.2			1.3	10.9

Glucose	5	20.4	20.0	0.2	5.32E+08	1.6	10.9
Glucose	6	25.3	19.9	0.4	1.28E+09	2.0	11.8
Glucose	7	30.0	19.9	0.6	1.90E+09	2.6	12.1
Glucose	8	37.3	19.3	1.2	3.83E+09	4.1	13.5
Glucose	9	40.9	18.7	1.6	5.17E+09	6.0	14.4
Glucose	10	45.3	18.1	2.1	6.83E+09	8.1	15.2

$\delta^{18}O_{(H2O)}$= 31.0‰

Experiment	Sample	Time (days)	SO_4 (mM)	H_2S (mM)	Cells (#/ml)	$\delta^{34}S$ (SO4)	$\delta^{18}O$ (SO4)
Glucose	0	16.9	19.9	1.0	9.11E+07	0.7	17.7
Glucose	1	9.8	20.2	0.6	8.50E+07	0.3	10.8
Glucose	2	1.0	20.4	0.4	1.44E+07	-0.5	8.4
Glucose	3	26.2	19.5	0.9	1.72E+08	2.6	27.1
Glucose	4	30.7	18.7	1.7	2.74E+08	4.2	32.9
Glucose	5	43.8	15.1	5.0	8.90E+08	15.9	48.3
Glucose	7	36.1	18.2	2.6	3.56E+08	6.1	38.8

Experiment	Sample	Time (days)	$\delta^{33}S$ (SO4)	$\delta^{34}S$ (SO4)	$\delta^{33}S$ (H2S)	$\delta^{34}S$ (H2S)
Glucose	3	26.2	1.2	2.2	-31.6	-60.5
Glucose	5	43.8	8.4	16.4	-31.6	-60.5
Glucose	7	36.1	2.7	5.3	-24.1	-46.4

$\delta^{18}O_{(H2O)}$= 77.8‰

Experiment	Sample	Time (days)	SO_4 (mM)	H_2S (mM)	Cells (#/ml)	$\delta^{34}S$ (SO4)	$\delta^{18}O$ (SO4)
Glucose	0	5.9	20.2	0.3	4.06E+06	-0.3	8.7
Glucose	1	14.8	20.0	0.5	2.78E+07	0.2	14.5
Glucose	2	22.0	19.5	0.5	8.17E+07	1.1	25.8
Glucose	3	31.2	19.1	0.9	1.71E+08	3.3	48.4
Glucose	4	35.7	18.3	1.8	3.51E+08	5.5	63.5
Glucose	5	48.8	14.6	5.6	9.71E+08	16.2	81.3
Glucose	7	41.1	17.7	2.5	4.06E+08	7.2	72.6

A.4.2 Data tables for Chapter 4

Table A.4.2.1: Pore fluids analyses at the Yarqon.

Depth (cm)	SO4 (mM)	$\delta_{34}S$ (SO4) (VCTD)	$\delta^{18}O$ (SO4) (VSMOW)	DIC (mM)	$\delta^{13}C_{(DIC)}$ (PDB)	CH_4 µM	$\delta^{13}C_{(CH4)}$ (PDB)

0.0	31.6	20.8	10.0				
0.6	32.2	22.6	10.8	7.2	-17.0	62	
1.9	28.4	25.1	11.7	11.4	-19.8		-67.3
3.1	24.4	n.d	13.0	14.8	-20.9	89	
4.3	21.4	28.9	13.3	17.4	-21.1		-68.1
5.6	19.1	31.9	13.6	21.5	-22.3	238	
6.8	14.4	35.4	15.2	25.4	-21.8		-73.8
8.1	13.1	38.5	16.8	30.2	-22.1	372	
9.3	10.0	43.5	18.5	33.7	-22.6		-78.6
10.6	6.9		18.9	35.4	-22.1	616	
11.8	5.0	51.3	18.6	41.6	-22.2		-76.6
13.0	3.6		18.8	40.1	-21.6	488	
14.3	2.8		17.0				-73.6
15.5				45.9	-22.0	461	
16.8	1.3			44.8	-21.8		-80.5
18.0	1.3			42.7	-21.9	439	
19.3	1.1			43.4	-22.2		-82.7
20.5						445	
21.7	0.8			48.3	-22.5		-80.0
23.0	0.9			47.1	-22.9	395	
24.2				50.3	-23.3		-78.2

Table A.4.2.2: Pore fluids analyses at the Qhison.

Depth (cm)	SO_4 (mM)	$\delta^{34}S_{(SO4)}$ (VCTD)	$\delta^{18}O(SO4)$ (VSMOW)	DIC (mM)	$\delta^{13}C$ (DIC) (PDB)	CH_4 (µM)	$\delta^{13}C_{(CH4)}$ (PDB)
0		20.9	11.8				
0.6	30.2	21.2	14.1	-9.9	1.8	0.3	
1.7	30.4	22.0	14.7	-13.0	5.6	0.4	
2.9	27.5	23.9	16.9	-15.5	6.2	0.7	-62.5
4.0	27.7	26.1	18.1	-17.0	10.8	0.5	
5.2		27.7	19.7	-17.5	12.8	0.5	
6.3	23.5			-18.0	16.8	0.5	
7.5	22.2	31.5	21.5	-18.3	18.2	0.4	-60.2
8.6	20.9			-18.2	24.0	0.4	
9.8	18.7					0.2	
10.9	16.8	36.9	22.6	-18.1	27.4	0.4	
12.1	14.7			-17.7	33.6		
13.2	12.3	43.1	24.3			0.2	
14.4	8.2					0.2	14.0
15.5	6.6			-16.5	40.9	0.3	
16.6				-15.6	42.7	0.3	-70.6

17.8	2.6					0.5	
18.9	1.4			-13.2	45.9	0.3	-73.2
20.1	1.3			-12.6	48.6	0.3	
21.2	0.7			-11.0	52.7	0.3	
22.4				-10.1	47.0		
23.5	0.6						
24.7	0.5						
25.8				-8.4	52.1		
28.1	0.5			-7.6	48.8		
30.4	0.3			-7.1	50.6		

Table A.4.2.3: Dissolved methane analyses from piston core at the Qishon

Depth (cm)	CH4 (mM)
13.5	0.9
16.5	0.5
26.5	2.1

A.4.3 Data tables for Chapter 5

Table A.4.3.1: Pore fluids analyses at the Acre

	Depth(cm)	SO_4 (mM)	$\delta^{34}S_{(SO4)}$	$\delta^{18}O_{(SO4)}$
NA-8-1	**1**	26.5	25.3	11.8
NA-8-2	**2**		27.3	11.0
NA-8-3	**3**	15.1	31.0	11.9
NA-8-4	**4**		36.5	14.7
NA-8-5	**5**	8.5	43.5	17.8
NA-8-6	**6**		47.4	20.2
NA-8-7	**7**	5.2	52.1	20.4
NA-8-8	**8**		53.6	19.4
NA-8-9	**9**	5.2	53.2	20.1
NA-8-10	**10**		46.9	18.5
NA-8-11	**11**	7.0	42.2	16.7
NA-8-12	**12**		39.3	16.4

Table A.4.3.2: Methane and $\delta^{13}C_{CH4}$ analyses at the Acre

Depth(m)	CH_4 (mM)	$\delta^{13}C_{(CH4)}$
0.5	0.3	-67.5
1.5	0.8	-76.0
2.5	0.3	-73.8
3.5	1.0	-75.7
4.5	1.4	-77.0
5.5	1.4	-80.6
6.5	1.3	-78.8
7.5	1.3	-78.3
8.5	1.4	-78.2

Table A.4.3.3: Pore fluids analyses at the Palmachim

	Depth (cm)	SO_4(mM)	$\delta^{34}S_{(SO4)}$	$\delta^{18}O_{(SO4)}$	DIC (mM)	$\delta^{13}C_{(DIC)}$
NA-80-1	0	31.9	20.2	8.6		
NA-80-2	0.5	n.d	21.7	9.7	4.1	-19.1
NA-80-3	4.5	32.0	21.7	9.4	6.8	-33.4
NA-80-4	8.5	28.2	24.9	11.0		
NA-80-5	10.5	16.4	32.3	14.1	10.7	-52.2

Table A.4.3.4: Methane and $\delta^{13}C_{CH4}$ analyses at the Palmachim

Depth (cm)	CH_4 (uM)	$\delta^{13}C_{(CH4)}$
0	31.7	-59.3
4	254.9	-43.1
8		-70.6
14	776.2	-70.4
15	209.8	-68.2
16	0.7	-69.3

Table A.4.3.4 Pore fluid analyses at site PC-6

Depth [cm]	**SO_4 [mM]**	**CH_4 [µM]**	**$\delta^{13}C_{DIC}$**	**DIC [mM]**	**$\delta^{18}O_{SO4}$**	**$\delta^{34}S_{SO4}$**
0	31.8		-1.3	2.4	9.4	20.2
1	31.2	0	-10.0	3.7	10.9	21.4
44	29.6	0	-13.7	4.4		
84	26.4	0	-19.4	7.2	12.6	22.5
134	20.8	0			15.2	
184	17.1	0	-26.4	13.5	18.3	25.5
234	12.8	0	-28.6	15.8	20.5	28.2
284	8.0	0	-30.6	18.6	24.0	32.2
324	4.5	0	-32.0	22.0	25.2	34.0
364	0.0	1	-32.8	21.7		
404	0.0	114	-30.9	23.5		
444	0.0	466	-27.8	24.3		

Data table for Chapter 6

Table A.4.4.1 Worldwide pore fluid $\delta^{18}O_{SO4}$ vs. $\delta^{34}S_{SO4}$ slope and the coresponding references.

Site name	**Location**	**Type**	**Slope**	**Error (2σ)**	**n[a]**	**Reference**
NA 8[b]	SE Mediterranean Sea	MiE[f]	0.45	0.06	5	Rubin-Blum et al. (2014)
NA 80[c]	SE Mediterranean Sea	MiE[f]	0.34	0.06	12	Rubin-Blum et al. (2014)
2639-3	Gulf of Mexico	MiE[f]	0.34	0.15	5	Aharon and Fu. (2003)
2639-4	Gulf of Mexico	MiE[f]	0.29	0.04	5	Aharon and Fu. (2003)
2647-3	Gulf of Mexico	MiE[f]	0.34	0.16	5	Aharon and Fu. (2003)

Oil	Gulf of Mexico	MiE[f]	0.34	0.06	13	Aharon and Fu. (2000)
Gas	Gulf of Mexico	MiE[f]	0.28	0.04	12	Aharon and Fu. (2000)
Ref	Gulf of Mexico	MiE[f]	0.66	0.3	6	Aharon and Fu. (2000)
Strander Bucht, Station 6	Baltic Sea	MiE[f]	0.45	0.04	10	Strauss et al., (2012)
Strander Bucht, Station 5	Baltic Sea	MiE[f]	0.29	0.13	7	Strauss et al., (2012)
Y1[d]	Yarqon estuary (Israel)	MiE[f]	0.35	0.01	11	Antler et al. (2013)
Y2	Yarqon estuary (Israel)	MiE[f]	0.47	0.05	6	Antler et al. (2013)
Y3	Yarqon estuary (Israel)	MiE[f]	0.37	0.03	8	Antler et al. (2014)
Q2	Qishon estuary (Israel)	MD[g]	0.73	0.16	6	Antler et al. (2014)
OS00-17	Amzon delta	N.D[h]	0.3	0.2	4	Aller et al. (2010)
OS00-16	Amzon delta	N.D[h]	0.29	0.05	6	Aller et al. (2010)
OST-2-LOW	Amzon delta	MD[g]	1.04	0.42	10	Aller et al. (2010)
OST-2-RISING	Amzon delta	MD[g]	0.58	0.12	9	Aller et al. (2010)
PC6[e]	SE Mediterranean Sea	MDL[i]	1.25	0.2	6	This study
BA1	SE Mediterranean Sea	MD[g]	1.06	0.11	8	Antler et al. (2013)
HU	SE Mediterranean Sea	MD[g]	0.99	0.13	5	Antler et al. (2013)
ODP 1082	SW Pacific	MDL[i]	2.2	3.31	4	Turchyn et al. (2006)
ODP 1086	SW Pacific	MD[g]	10.73	7.01	3	Turchyn et al. (2006)
OPD 1225	Peru Margin	MD[g]	4.53	1.37	9	Böttcher et al. (2006); Black et al. (2006)
ODP 1226	Peru Margin	MD[g]	0.96	0.47	4	Böttcher et al. (2006); Black et al. (2006)
ODP 1123	West Africa	MD[g]	1.4	0.24	5	Turchyn et al. (2006)
ODP 1052	NW Atlantic	MD[g]	1.69	0.18	8	Antler et al. (2013)

[a] The number of analyses that were used for the linear regression.

[b] ‘Black patch’ in figure 1a.
[c] ‘Gas seeps’ in figure 1a.
[d] ‘Estuary’ in figure 1a.
[e] ‘SMTZ’ in figure 1a.
[f] MiE- methane-in-excess
[g] MD- methane-devoid
[h] N.D- methane was not measured
[i] MDL- methane-diffusion-limited